MAGNETO-INFRARED SPECTROSCOPY OF EMERGING TOPOLOGICAL MATERIALS

A Dissertation
Presented to
The Academic Faculty

By

Yuxuan Jiang

In Partial Fulfillment
of the Requirements for the Degree
Doctor of Philosophy in the
School of Physics

Georgia Institute of Technology

August 2017

MAGNETO-INFRARED SPECTROSCOPY OF EMERGING TOPOLOGICAL MATERIALS

Approved by:

Professor Zhigang Jiang, Advisor
School of Physics
Georgia Institute of Technology

Doctor Dmitry Smirnov
Condensed Matter Science
National High Magnetic Field Laboratory

Professor Phillip First
School of Physics
Georgia Institute of Technology

Professor Edward Conrad
School of Physics
Georgia Institute of Technology

Professor Martin Mourigal
School of Physics
Georgia Institute of Technology

Date Approved: May 02, 2017

ACKNOWLEDGEMENTS

When I applied for graduate school six years ago, I was not very confident whether I can make through a physics Ph.D. or not, given that physics is such a profound subject and also some negative impression on Ph.D. life - endless work and pressure. It turns out that my journey has been very enjoyable: I have learnt exciting physics (though still feel ignorant today) and the fun to do experiments while enjoying a great life!

Among all the people who made this possible, it is my very best of luck to have Prof. Zhigang Jiang as my advisor. On the scientific side, he is a "hardcore" physicist. He would interrogate every detail in the data carefully. He tries to do the best rather than just being Ok. At one time, we were having troubles with the noise problem in the measurement. He almost disassembled all the instruments just to find out the noise source. It is in this rigorous training that I learnt how to fight with measurement problems and not just treat the instruments as a black box.

On the other hand, he is very approachable and ready to help at any time. He taught me how to do experiments hand by hand and sometimes he joined the experiment himself, which has surprised my friends because many of their advisors have already forgot the experiment details. Whenever I have questions and no matter how naïve they are, He is always there to answer with his deep knowledge. Sometimes I pretended to understand his answer hoping to figure out myself later but ended up coming back with the same question, he is still very happy to help me out. I am always amazed that he never seems to lose his inner peace uner any circumstances. The only exception may be when his son is being naughty. Through our interactions, I can feel that he not only cares about my present but also thinks in the best interest of my future development. At my third year, he offered me the opportunity to stay at the National High Magnetic Field Laboratory (Maglab) for two years. Recently on my postdoc application, he not only gave me informative guidance on each potential advisor but also actively reached out from his network to help me out. There

are many examples to continue and they may seem trivial. However, it is through these examples that he taught me how to be a grown man in life and science, and I am forever grateful to him.

I also deeply appreciate the strong support from Dr. Dmitry Smirnov, who is my supervisor during my stay at Maglab. The best thing being in a national lab is the numerous resources that one can reach out for experimenting new ideas. Dmitry is always supportive on trying new ideas and never limits his students with existing projects. One of his famous quotes is "every initiative should be punished". My interpretation is that he provides as many resources as he can to make the initiative happen and he will also take the responsibility. Whenever I need something, he will search out the lab or take me to someone who may have the resource and see to it happen. Whenever I run into problems, he troubleshoots with me together, through which I have benefited from his wisdom in instrumentation, optics, and history. Whenever I make stupid mistakes, he covers my back. It is with such strong support that I can focus on the fun of doing experimental physics. I can still vividly recall the most exciting moment when we saw the circular polarization resolved setup we developed indeed revealed an asymmetric lineshape between the two polarizations. The excitement is not just about discovering physics but also about realizing exciting ideas through own instrumentation. I believe many would feel the same way when their long term efforts pay off. The only pity is that I did not have the chance to fully understand and publish this beautiful data.

My experiments in Maglab would not be successful without the support from other maglab staffs: Dmitry Semenov, Renee Luallen, Mykhaylo (Mike) Ozerov, Ryan Baumbach, David Graf, Ju-Hyun Park, Timothy Murphy, and many others. Every experimentalist knows the importance of having a good sample and we are so lucky to have Zhiling Dun and Prof. Haidong Zhou from University of Tennessee at Knoxville to supply us with high quality single crystals and also Dr. Wei Pan from Sandia National Lab for the quantum wells samples. Theoretical support is also indispensible in understanding the physics be-

hind our experiment. Thanks to Prof. Christopher Stanton in University of Florida for his guidance, I can finally workout all the details in the $\mathbf{k} \cdot \mathbf{p}$ model to explain the complicated transitions in the InAs/GaSb quantum wells. I would like to thank all my committee members, Profs. Phillip First, Edward Conrad, Martin Mourigal, for spending their time reading my thesis and providing feedbacks.

In this journey, I also benefited a lot from my peers. I would like to express my sincere thanks to Zhengguang Lu from Dmitry's group. He has helped me enormously in the endless nights during my experiments in maglab. It is very usual that we transferred helium together at 4 in the morning or align optics until late night. He would took over my experiment after I stayed overnight. I have learnt my knowledge about Raman and PL spectroscopies from him. His valuable experience in optics, (which claims to be the result of frequent shoppings in Thorlabs), greatly facilitated the development of the circular polarization resolved setup. Thanks to the diversified research environment in Maglab, I also get a taste of the world outside my research areas from both internal research graduates such as Jean-Marie Poumirol, Yu-Che Chiu, Kuan-Wen Chen, Lai You, Minseong Lee, and external user such as Xu Yang during my stay in maglab. I should also make my apologies here that I have been stealing their snacks in the late night during my experiments. Back in Georgia Tech, I would like to thank Wenlong Yu, Xunchi Chen, Chao Huan, Owen Vail, Jeremy Yang, and Di Chen. Not only have I learnt about the instruments operation and device fabrication from you guys but also enjoyed the interesting discussion inside and outside physics such as "how many physicists does it take to change a light bulb" or "are you willing to sacrifice one part of your body for a reasonable wish".

Outside research, I can't imagine the life without my dearest friends, especially those from Peking University. I would like to thank Eric Yue Ma for hosting me in Stanford every summer and taking me to fishing and crabbing on the Pacific piers. He is also my major peer pressure since I always felt ignorant when we discuss physics. I would like to thank Shi Liu for organizing numerous trips into the wonderlands of national parks. I thank Yun

Wei for teaching me how to drive, which greatly improves my mobility. Back in China, my gratitude goes to Xuanming Situ for accomodating me in Beijing and listened to my ups and downs in the past few years. The thank list goes on (Chen Zhang, Zhongjing Chen, Chen Wang, Zheng Li, Ting Zhang, Hao Luo, Wei Shang, Qingyuan Lin, Yiping Dong, etc.). I am very lucky to have you all and knowing that wherever I go, I can have a good friend to count on.

I would like to thank Prof. Tongjun Yu in Peking University, for her guidance in my undergraduate research and support for the graduate applications, and also Liqiang Sun and Prof. Liangzhu Mu for introducing me to Zhigang, which gave me the ticket to this journey.

Finally, I want to thank my parents for taking a good care of the family so that I don't have to watch my back.

TABLE OF CONTENTS

LIST OF TABLES

LIST OF FIGURES

SUMMARY

Topological insulators (TIs) have recently attracted much attention due to their robust edge/surface states against disorders and external disturbance under the protection of symmetries. Such robust states hold great promise for application in spintronics and quantum computing. Therefore, intense explorations and characterizations of possible TIs have been carried out in the scientific community. In this thesis, we use magneto-infrared spectroscopy to study the electronic band structures of two TI candidates. The first candidate is InAs/GaSb double quantum wells. We showed that when its band structure crosses the boundary from the normal state to the inverted state, multiple absorption modes emerge. This normal-inverted state transition can be described semi-quantitatively with an eight-band $\mathbf{k} \cdot \mathbf{p}$ model. We further demonstrate that the transition is widely adjustable with the effects of strain, magnetic field and quantum well widths, which paves the way for band engineering of optimal InAs/GaSb structures for realizing novel topological states as well as for device applications.

Another candidate studied in this thesis is zirconium pentatelluride ($ZrTe_5$). The transmission spectra measured at zero magnetic field is suggestive of a quasi-2D nature in bulk $ZrTe_5$ similar to that in graphene. The Landau level transitions clearly follow a square-root magnetic field dependence, which is a signature of Dirac bands, only with a small energy gap of ~ 9.4 meV. A four-fold splitting in low lying interband transitions are resolved under high magnetic fields, while circular polarization resolved measurements help identify a significant contribution from electron-hole asymmetry. We employ a model based on the Bernevig-Hughes-Zhang effective Hamiltonian to determine the values of the Fermi velocity, Dirac mass (or gap), electron-hole asymmetry, and electron and hole g-factors in $ZrTe_5$. Our results support the topological Dirac semimetal picture with a small energy gap.

CHAPTER 1
INTRODUCTION AND BACKGROUND

The classification of materials into conductors and insulators is famously known to the public. However, this notion was challenged by the discovery of quantum Hall effects (QHEs) [1] (Fig. 1.1(a)) in which conducting edges coexist with an insulating bulk. How can this system be classified? Another surprising result related to QHEs is the extremely accurate quantized value of the transverse resistance (Fig. 1.1(b)) regardless of the disorder. It was later discovered that these two phenomena can be explained by the so-called topological band theory [2, 6]. In conventional band theory, depending on the Fermi level relative to the bands, the material is either a conductor or an insulator. In contrast, the topological band theory emphasizes the topology of the wavefunction rather than the bands, which enables the exploration of novel materials such as topological insulators,superconductors, and nodal semimetals. In addition, on the application side, novel properties such as protected states in this new class of materials render them promising for next generation information technology. All these factors have stimulated the rapid progress in the emerging field of topological materials.

In this chapter, we will introduce basic topological band theory in the context of topological insulators (TIs) since this is the most relevant subject to this thesis. The discussion will be mostly intuitive, therefore mathematical formulation will be largely avoided. The classification of TI will also be discussed.

1.1 Topological order in band theory

In mathematics, the study of topology focuses on the invariant geometric property under continuous transformation of an object instead of the details of its geometry. For example, in view of conventional geometry, shapes are classified into rectangular, circle and others.

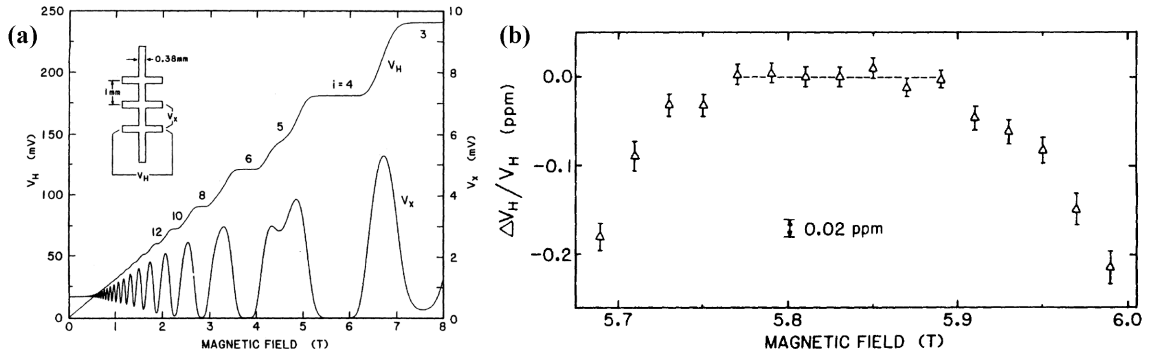

Figure 1.1: Quantum Hall effect. (a) Magnetic field dependence of the transverse voltage V_H and longitudinal voltage V_x. As magnetic field increases, the V_H develops a plateau (quantized region) where the V_x reaches zero. Inset in (a) shows the measurement configuration. (b) Quantization accuracy of the V_H measurement. The deviation from the quantized value is found to be 0.1 parts per million (ppm). Adapted from Ref.[3].

In topology, these are all in the same classification as long as they can transform into others under smooth deformation as shown in Fig. 1.2(a) and (b). In contrast, a donut shape is topologically inequivalent to a circle because it is inevitable to break a hole in a circle to deform into a donut(Fig. 1.2(c)). Such a deformation is not a continuous transformation. Thus, geometric objects can be classified based on their topological property instead of their geometric shape. A formal way to define this is to specify curvature at each points and integrate over the whole space to get a topological number, which describes the topological order of an object. In fact, it has been shown that the resulting topological number is related to the number of holes in an object [4], which allows for straightforward determination without complicated mathematical calculation.

In solid-state physics, the corresponding topology concept is established upon the abstract Hilbert space spanned by the wavefunction from a band. In other words, the wavefunction in Hilbert space is just like the points in real space that form the geometric shape to be studied. Apparently, this is a much more abstract idea, and unlike the case in mathematics, there are rarely obvious features that can be linked to the topological number of a band. However, it is found that the topologically nontrivial bands are likely to be associated with band inversion. Usually, electrons in filled orbits form valence bands (VBs), while un-

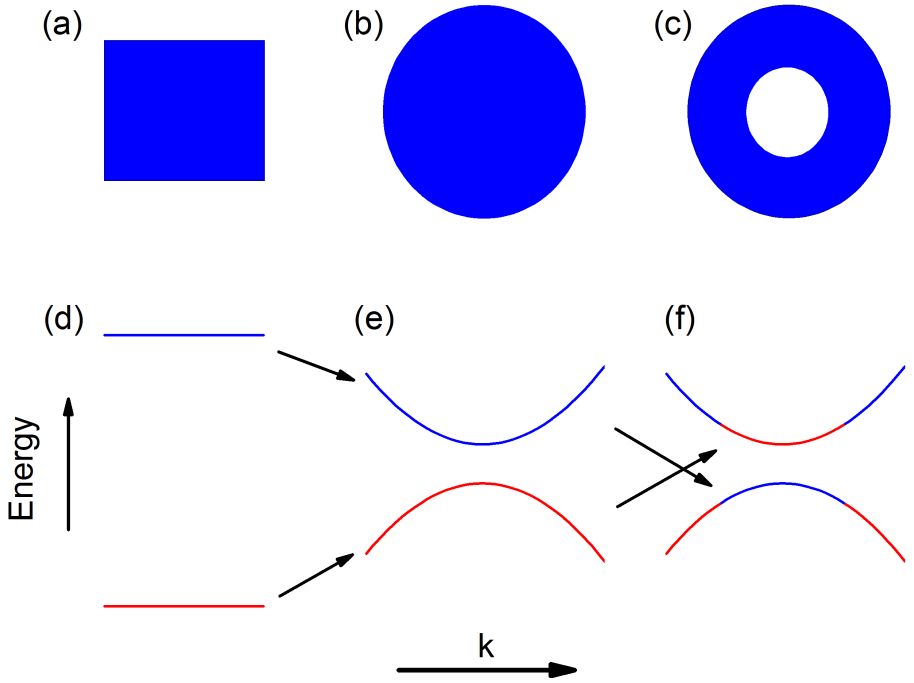

Figure 1.2: Topology in band structures and geometries. In mathematics, a (a) rectangular shape is topological equivalent to a (b) circle, but different from a (c) donut shape. Similarly, a (d) vacuum state is topologically equivalent to a (e) normal state band structure but not an (f) inverted band structure. The arrows in (d-f) indicate the transition from a normal to an inverted state. From (e) to (f), the system will inevitably pass through a gapless state.

filled or partially filled orbits form conduction bands (CBs). If the CBs lay above the VBs, it is in a normal order (Fig. 1.2(d) and (e)). But due to certain effects, such as spin-orbit coupling or quantum confinement effect, it is possible that VBs cross above CBs and form the so-called band inversion (Fig. 1.2(f)). From this picture, systems in a normal state can never reach a band inversion state without closing a gap, and the energy gap opened by band-inversion is topologically distinct from the normal band gap. Two systems are said to be topologically equivalent if one system can transform into another without closing the gap. For example, silicon (Fig. 1.2(e)) can be thought the same as vacuum (Fig. 1.2(d)) in band structure topology since the band gap in silicon can be tuned to the same as vacuum by moving the silicon atoms apart.

It is important to note that even though band inversion is important in many realizations of TI materials, it is only an indicator and neither a necessary nor sufficient condition leading to a topologically nontrivial state. A counter example would be the QHE, which is topological nontrivial but does not involve any band -inversion. A mathematical description is needed to identify the topological nature of the states.

The mathematical description of the topological index of a band can be constructed using the Berry phase [2]. If the Bloch wave function of band m is denoted as $|u_m(\mathbf{k})\rangle$, the topological index can be defined as

$$n_m = \int_C A_m \cdot d\mathbf{k} = \int_{\mathbf{C}} \mathbf{i} \langle \mathbf{u_m} | \nabla_{\mathbf{k}} | \mathbf{u_m} \rangle \cdot \mathbf{dk}, \tag{1.1}$$

where the integral runs over the zone boundary C. This equation is essentially the expression for Berry phase [5]. Alternatively, One can also express the topological index using a surface integral of the Berry flux $\nabla \times A_m$,

$$n_m = \int_S \nabla \times A_m d^2k, \tag{1.2}$$

where Stokes theorem is applied and the integral is over a surface S bounded by the closed

loop C. The topological index of a system is the sum of the contributions from all fully occupied bands. It can only take integer values, as in the case of geometric objects.

In 1982, Thouless, Kohmoto, Nightingale and den Nijs (TKNN) found that the Hall resistance in QHE is determined solely by the topological index of the system, found to be the same as the Chern number [6]. Since the Chern number only reflects the number of filled bands but not the detailed information about the electron wavefunction, this discovery essentially explains the quantization of Hall resistance and the universality of the QHEs.

The concomitance of zero longitudinal resistances (resulting from ballistic edge transport) with quantized Hall resistances in QHE suggests that the edge states are also a consequence of the nontrivial topology. This is because the band-gap has to be closed at the interface in order to connect the two topologically distinct states, vacuum with Chern number 0 and the bulk with Chern number n, adiabatically. Meanwhile, it is worth noting that the number of edge states is equal to the difference of the topological order across the interface. This observation is an example of the bulk-boundary correspondence, which relates the edge/surface states with the bulk topological states across an interface.

QHE provides a simple picture to understand the basics of topology in band structures. The related topological number here is the Chern number. If additional symmetry is allowed, there could be other topological indices defined. Time reversal symmetry (TRS) is a very common symmetry. Many topological materials discovered up to date are classified under this symmetry, which is to be discussed in the next section in the context of TIs.

1.2 Two dimensional topological insulators

The realization of QHE requires breaking the TRS by applying a magnetic field. However, it is possible to construct a topologically non-trivial case,the so-called quantum spin Hall (QSH) state or two-dimensional (2D) TI, without violating TRS. Figure 1.3 shows conceptually how this can be done using two QH systems with opposite Chern numbers. These QH systems have opposite magnetic fields and also edge states traveling in opposite

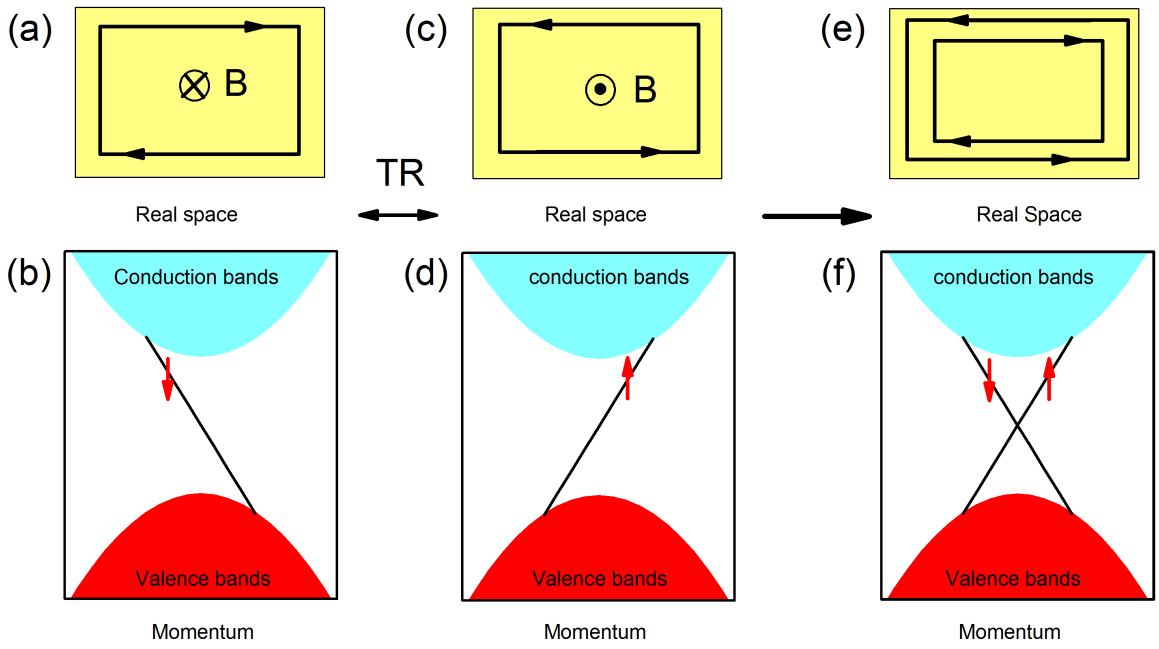

Figure 1.3: Quantum spin Hall effect. A QH system with Chern number (a) (b) $n = 1$ is a TRS copy of that with (c) (d) $n = -1$. The red arrows denote the spin directions. (e) The QSH system can be viewed as a superposition of two copies of QH systems with opposite Chern numbers, producing a time reversal pair of (f) spin polarized surface states. In addition, the spin directions are locked to the traveling directions of electrons.

directions. If the two copies are "merged", the total external magnetic fields is zero, thus retrieving TRS while maintaining the edge states propagating along the boundary. One immediate difference to note from the QHE is that the edge states now must come in pairs. In addition, though the total magnetic field is zero, electrons in each of the QH copies should still experience a non-zero intrinsic magnetic field. This is realized through the spin-orbit interaction (SOI). Generally speaking, electrons in materials will experience the Coulomb effect from the background ions. From relativistic theory, electric field can be transformed into magnetic field through a reference transformation. It follows that electrons in their own reference frames can experience a magnetic field whose direction is determined by the spin direction. The SOI can be greatly enhanced by choosing a heavier element with stronger ionic electric fields. The strong intrinsic magnetic fields also lift the spin degeneracy. However, with TRS the spin degeneracy may be recovered at certain high symmetry $\mathbf{k}$ points. This can be understood through the Kramer theorem, which guarantees that if $|\mathbf{k}, \mathbf{s}\rangle$ is a solution to a system's Hamiltonian, then $|-\mathbf{k}, -\mathbf{s}\rangle$ is also a solution with the same eigen energy under TRS. Therefore, a $\mathbf{k}$ point that can be folded back to itself through the $k = -k$ relation will retrive the spin degeneracy. These points are called time reversal invariant momenta (TRIMs). Γ point is an obvious TRIM. Another set of TRIMs are the boundary points due to the periodic condition of a Brillouin zone. Between these TRIMs, there is no spin degeneracy, and the number of edge states must be even. These states begin from a TRIM and either end at another TRIM or merge into bulk bands, resulting in two distinct possibilities. If a pair of edge states leaves a TRIM and both go into another TRIM, the Fermi level must have even crossing points with edge states(Fig. 1.4(a)). If this pair of bands leaves a TRIM but connects with two different TRIMs, the Fermi level must have odd crossing points with the edge states (Fig. 1.4(b)). By moving the TRIMs up and down but keeping their relative positions, all the odd crossing points can be reduced into one crossing point while all the even crossing points can be eliminated. In other words, an odd crossing points case implies that the surface states are gapless while an even crossing

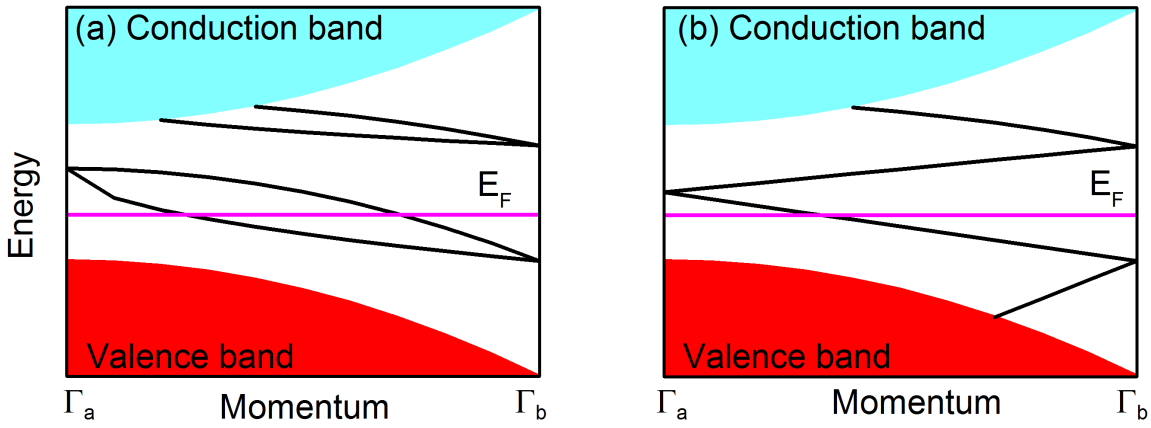

Figure 1.4: Edge states connecting TRIMs. Two possibilities for edge states connecting two TRIMs: (a) the topological trivial case where the Fermi level crosses even times of the edge states, and (b) the topological nontrivial case where the existence of edge state is guaranteed. Adapted from Ref. [2].

points case is a gapped system. Thus, these two topological distinct states is labeled by a Z_2 index which only takes the value of 0 or 1. Here, Z means integers, and 2 means modulo of 2. The odd crossing points case is topologically nontrivial because no matter how the bands are manipulated, the crossings of edge states with Fermi level are guaranteed and thus the existence of surface states.

Another interesting property from TRS is the spin-momentum locking. From the Kramer theorem, the energy degenerated spin up and spin down states are resolved in opposite momenta. Therefore, each spin in a given band is locked to a specific traveling direction. This is termed spin-momentum locking in edge states. In consequence, it would be difficult for an electron to reverse its moving direction (backscattering) since this scattering process also requires flipping the spin.

Graphene was the first material predicted to be a 2D TI [7], but carbon atoms are so light that the SOI does not produce observable effects. Later, Bernevig et.al. [8] proposed that HgTe/CdTe quantum wells (QWs) are a potential candidateand its band alignment can be tuned through quantum confinement effect. In HgTe/CdTe QWs, the constituent material CdTe has a normal band ordering while HgTe is inverted due to the heavy element Hg. In HgTe/CdTe QWs, if the well width of HgTe is reduced to 0, the band structure will be the

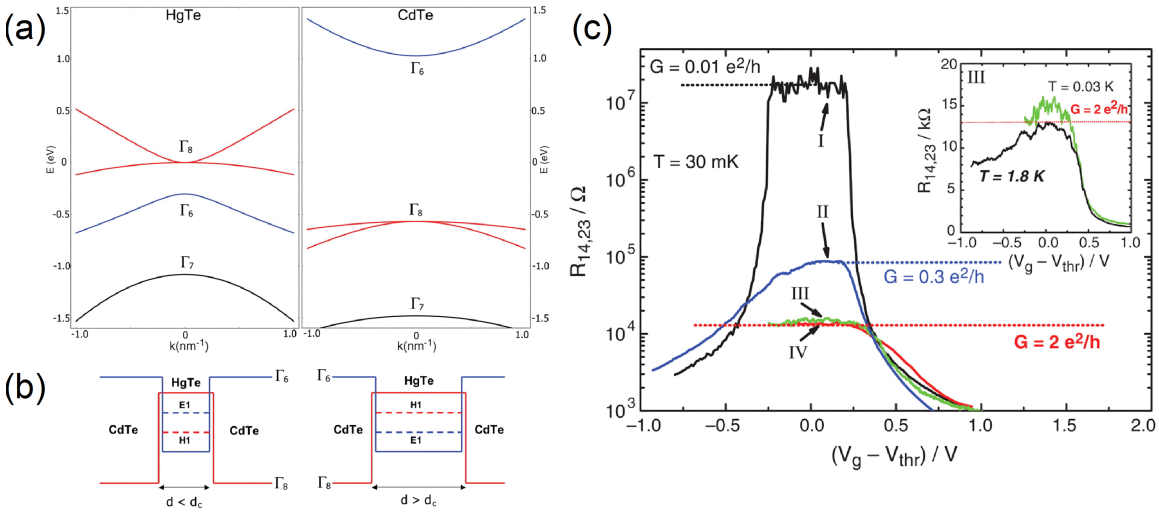

Figure 1.5: 2D TI phase in CdTe/HgTe QWs. (a) The band ordering in the constituent materials HgTe and CdTe. (b) Band alignment of the QW structure with HgTe well width d below and above the critical width d_c. The left panel shows the normal band alignment while the right panel shows the inverted alignment. (c) The measured quantized conductance in the inverted CdTe/HgTe QWs as a strong evidence to the TI phase. Adapted from Refs. [8, 9].

same as CdTe. On the other hand, a very thick HgTe layer will produce an inverted band structure similar to HgTe. Somewhere between these two extrema, the lowest CB will meet the highest VBs. Electronic transport measurements [9] on HgTe/CdTe QWs at different thickness confirmed the transition from the normal to the inverted band structure. The longitudinal resistances and non-local measurements [10] agree well with the Landauer-B üttiker theory in the context of QSH, giving strong evidence of the 2D TI phase in this system (Fig. 1.5).

More recently, InAs/GaSb double quantum wells (DQWs) [11] have also been predicted to be a 2D TI. It is based on the so-called broken-gap band alignment between InAs and GaSb. The advantages of the InAs/GaSb DQWs over the HgTe/CdTe QWs are two fold. First, the electronic band structures in InAs/GaSb DQWs can be tuned via top and bottom gates in addition to the quantum confinement effect. Second, InAs/GaSb DQWs are easier to handle and much more available compared to the delicate HgTe/CdTe system. Since the InAs/GaSb DQWs system is one of the central topics in this thesis, we will discuss in

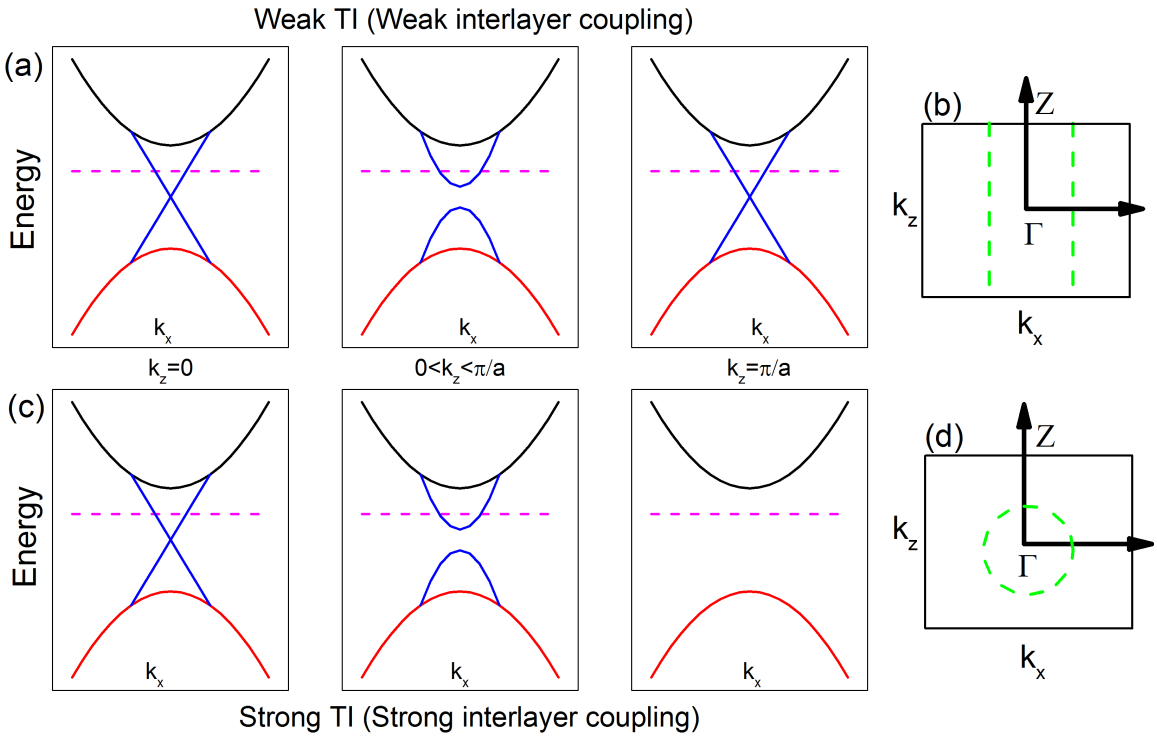

Figure 1.6: Weak and strong TIs. Electronic band structures of (a) weak and (c) strong TIs at different cuts in the k_z direction. The pink lines represent the Fermi level crossing the surface states (blue). Surface states projections (green) onto the $k_x - k_z$ planes in (b) weak and (d) strong TIs .

further details in Chapter 4.

1.3 Three dimensional topological insulators

Next, we want to study the TI phase in three dimensional (3D) case. A simple way is by stacking many 2D TI layers to form a bulk material. It turns out that the resultant 3D bulk material can be either a strong or weak TI(Fig. 1.6) depending on the interlayer coupling [12]. In the weak coupling case(Fig. 1.6(a)), the gapless edge states are preserved at the TRIM point at different k_z cuts. An extreme case would be no coupling at all, where the surface states persist throughout the k_z direction. If all these surface states at different cuts are projected onto the $k_x - k_z$ plane, it turns out that not every k direction has protected surface states. For example, in Fig. 1.6(b), the system is in a trivial state along the k_z direction whereas it is in a non-trivial state along the k_x direction. On the other hand, in

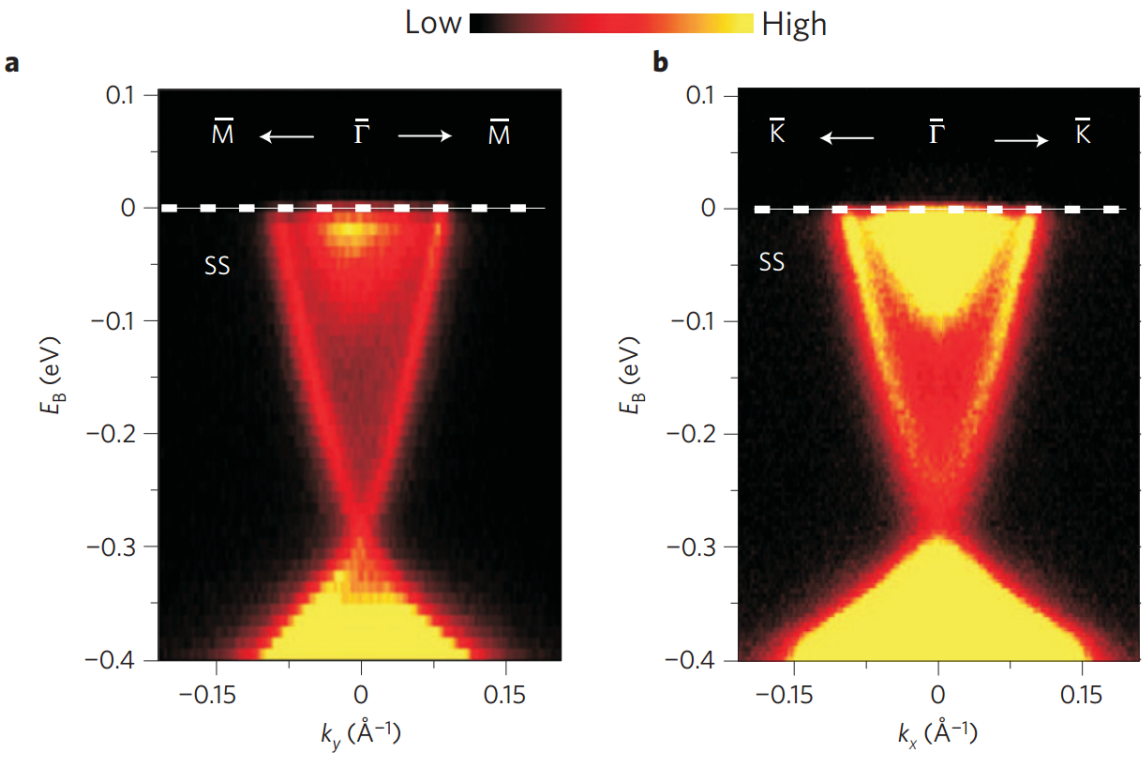

Figure 1.7: Observation of surface states in a 3D TI. ARPES results of the bulk and surface band structures in Bi_2Se_3 along (a) $\bar{\Gamma} - \bar{M}$ and (b) $\bar{\Gamma} - \bar{K}$ directions. Between the bulk bands, two bright lines represent the surface states, which is a signature of 3D TI. Adapted from Ref.[14].

Fig. 1.6(c) and (d), though the strong coupling destroys the surface states at the boundary in the k_z direction, the surface states projected onto the $k_x - k_z$ plane are preserved in all directions. Apparently, the latter case is more robust and thus called strong TI compared to the former case (i.e. weak TI) where only certain directions carry surface states. It is somewhat surprising to see that a system with surface states in all directions turns out to be a weak TI. This is similar to a trivial 2D insulator with Fermi level crossing the edge states even times and multiple edge states interfering destructively [13].

There are many 3D TIs discovered up to date [15]. The first experimentally confirmed 3D TI is $Bi_{1-x}Sb_x$ [16]. However, the most studied 3D TIs are the binary compounds in tetradymite family such as Bi_2Se_3 [14] because they have a much simpler surface band structure and a much wider bulk band gap. Figure 1.7 shows the experimental verifications

of the surface states within the bulk gap in Bi_2Se_3 using angle resolved photoemission spectroscopy (ARPES). A drawback of these binary compounds is the high doping level due to the residual carriers in the bulk which easily mask the surface states. Semi-insulating samples have recently been achieved by either expanding the composition into four elemets such as $Bi_{2-x}Sb_xTe_{3-y}Se_y$ [17] or by introducing suitable substitutions for the Bi element [18, 19].

The experimental progress on 3D TIs reveals several advantages over 2D TIs. First, they are easier to prepare as evidenced by numerous discoveries of 3D TIs. Compared to 2D TIs that require the state-of-the-art molecular beam epitaxial (MBE) growth technique for extremely thin and high quality layers, 3D TIs growth techniques are much more cost effective and approachable. Second, 3D TIs in general show a much larger band gap than 2D TIs, which makes them more realistic for device applications. On the down side, the doping levels in 3D TIs are relatively high and it is much more difficult to tune the bulk carrier density in 3D than 2D due to the additional dimension. Consequently, electrical transport measurements targeting on surface carriers are difficult to perform. Surface sensitive spectroscopic techniques such as ARPES or scanning tunneling microscopy (STM) become important in 3D TI verification.

1.4 Outline of the thesis

This thesis is organized as follows: Chapter 2 is devoted to the theoretical descriptions of band structures with and without magnetic fields. We start with the free electron model and then discuss how the electron energy dispersions are modified in the presence of a magnetic field. We consider a more realistic picture by including the interaction between different energy bands in a semiconductor using the $\mathbf{k}\cdot\mathbf{p}$ model and the Bernevig-Hughes-Zhang model. These models are used in Chapters 4 and 5 to understand the experimental data. Chapter 3 introduces two experimental techniques: Fourier transform based and quantum cascade laser based magneto-infrared spectroscopy. The operating principles and detailed instru-

mentations are discussed. Chapter 4 presents the magneto-infrared spectroscopy study on the quantum phase transition in InAs/GaSb DQWs, which has recently been predicted as a 2D TI. Chapter 5 focuses on the band structure of zirconium pentatulleride ($ZrTe_5$) again using magneto-infrared spectroscopy. Monolayer ZrTe5 has also been theoretically predicted as a 2D TI, while its bulk property is thought to be at the boundary of a strong TI and a weak TI phase. Finally, Chapter 6 concludes the thesis and discusses possible future directions.

CHAPTER 2

THEORY OF LANDAU LEVEL SPECTROSCOPY

Landau level (LL) spectroscopy is a powerful tool to probe the electronic structure of a material with the help of magnetic fields. In this chapter, we will first discuss the modification induced by magnetic fields on a free electron and the consequent change in its energy dispersion. Next, we will introduce $\mathbf{k} \cdot \mathbf{p}$ and Bernevig-Hughes-Zhang (BHZ) models to handle a more complicated case both with and without magnetic fields. These two models are the main keys to understanding the experimental results in this thesis.

2.1 Landau level and its dispersion

The energy dispersion of a free electron is achieved by solving the following Schrödinger equation

$$\frac{\mathbf{p}^2}{2m}\Psi(\mathbf{r}) = E\Psi(\mathbf{r}), \tag{2.1}$$

where m is the bare electron mass, $\mathbf{p} = -i\hbar\nabla$ is the momentum operator and E is the eigenenergy. The energy follows the well-known parabolic dispersion

$$E(\mathbf{k}) = \frac{\hbar^2\mathbf{k}^2}{2m}, \tag{2.2}$$

where $\mathbf{k}$ is the wave-vector and $\hbar$ is the reduced Planck constant. The corresponding eigenfunction is just a plane wave $\Psi(\mathbf{r}) = e^{i\mathbf{k}\cdot\mathbf{r}}$.

Assuming a magnetic field $\mathbf{B} = (0, 0, B)$ in the z direction, the Schrödinger equation is

modified with the canonical momentum

$$\mathbf{p} \rightarrow \mathbf{p} + e\mathbf{A}, \tag{2.3}$$

and results in

$$\frac{(\mathbf{p} + e\mathbf{A})^2}{2m}\Psi(\mathbf{r}) = E\Psi(\mathbf{r}), \tag{2.4}$$

where e is the elemetary charge and $\mathbf{A}$ is the vector potential satisfying $\mathbf{B} = \nabla \times \mathbf{A}$. Here, we use the Landau gauge: $\mathbf{A} = (-By, 0, 0)$.

If we define the ladder operators

$$a^\dagger = \frac{l_c}{\sqrt{2}\hbar}(p'_x + ip'_y), \qquad a = \frac{l_c}{\sqrt{2}\hbar}(p'_x - ip'_y), \tag{2.5}$$

where $l_c = \sqrt{\frac{\hbar}{eB}}$ is the magnetic length and the primes are to denote the operators after substitution. The ladder operators satisfy the commutation relation $[a, a^\dagger] = 1$, with which Eq. (2.4) can be rewritten into

$$\big[\hbar\omega(a^\dagger a + \frac{1}{2}) + \frac{p_z^2}{2m}\big]\Psi = E\Psi, \tag{2.6}$$

where $\omega = eB/m$. The energy dispersion of an electron in magnetic fields is

$$E(n, k_z) = \hbar\omega(n + \frac{1}{2}) + \frac{(\hbar k_z)^2}{2m}. \tag{2.7}$$

The corresponding eigenfunction for $E(n, k_z)$ is the nth order Hermite function. In the 2D case, $k_z = 0$ and Eq. (2.7) reduces to

$$E(n, k_z) = \hbar\omega(n + \frac{1}{2}). \tag{2.8}$$

Comparing Eqs. (2.2) and (2.8), magnetic fields can split a continuous band into infinite subbands (also named LLs), denoted by the LL index n, and can reduce the degree of freedom by 1. In addition, the electron wavefunction changes from a free propagating plane wave into a localized function due to the parabolic confinement potential from magnetic fields. This is consistent with the classical picture that charged particles exercise cyclotron motions in the plane perpendicular to magnetic fields. Since each electron is confined within the scale of the magnetic length l_c introduced above, N electrons cover an area of $S = N\pi l_c^2$ and the degeneracy of each LL per spin can be calculated through

$$n_e = \frac{N}{2S} = \frac{e}{2\pi\hbar}B, \tag{2.9}$$

where n_e is the charge density.

Another important point to note is that the magnetic field dispersion of the LLs reflects the zero field energy dispersion relation of the materials. As another example, if an electron now follows a linear dispersion, the Hamiltonian can then be written as

$$\hbar v \begin{pmatrix} 0 & k_x + ik_y \\ k_x - ik_y & 0 \end{pmatrix} \Psi = E\Psi, \tag{2.10}$$

where v is the velocity of the electron. The eigenenergy is $E = \pm\hbar v|\mathbf{k}|$ with a plane wave as its eigenfunction. In magnetic fields, the Hamiltonian can be again rewritten in terms of the ladder operators (2.5) after replacing the momentum with the canonical momentum:

$$\sqrt{2}\frac{\hbar v}{l_c} \begin{pmatrix} 0 & a^\dagger \\ a & 0 \end{pmatrix} \Psi = E\Psi. \tag{2.11}$$

Using the ansatz $\Psi = (\phi_n, \phi_{n-1})$ where ϕ_n is the nth order Hermite function, the Hamilto-

nian is transformed into

$$\sqrt{2}\frac{\hbar v}{l_c}\begin{pmatrix} 0 & \sqrt{n} \\ \sqrt{n} & 0 \end{pmatrix}\Psi = E\Psi. \tag{2.12}$$

Solving this algebra eigenproblem, the energy dispersion in magnetic fields reads

$$E = \pm v\sqrt{2|n|\hbar Be}. \tag{2.13}$$

Two immediate differences from Eq. (2.8), the square root energy dispersion in magnetic fields and in LL index, can be noticed. In addition, the zero LL is pinned at zero energy and does not change with magnetic fields. As a result, the energy gaps between adjacent LLs are no longer the same as the parabolic case.

Figure 2.1 summarizes the magnetic field effects on the above two cases. Because the magnetic field reduces one degree of freedom and simplifies the dispersions in the studied system, it is easier to reconstruct the zero field dispersion by probing the energy dispersions in magnetic fields. One of the common techniques is to shine lights onto a material and measure the changes in transmission/reflection as a function of magnetic field. If the incident photon energy matches the transition energy between two LLs, the particles in the system can be excited by absorbing photons and produce a change in the transmission/reflection. This technique probes the transition energies between LLs, giving rise to its name LL spectroscopy, which is the main experiment technique used in this thesis.

Figure 2.2 compares the LL spectroscopic measurements in GaN and multilayer graphene. The linear fit of the absorption energy in magnetic field indicates that GaN has a parabolic band while graphene requires a square root fit, indicating its linear band dispersion.

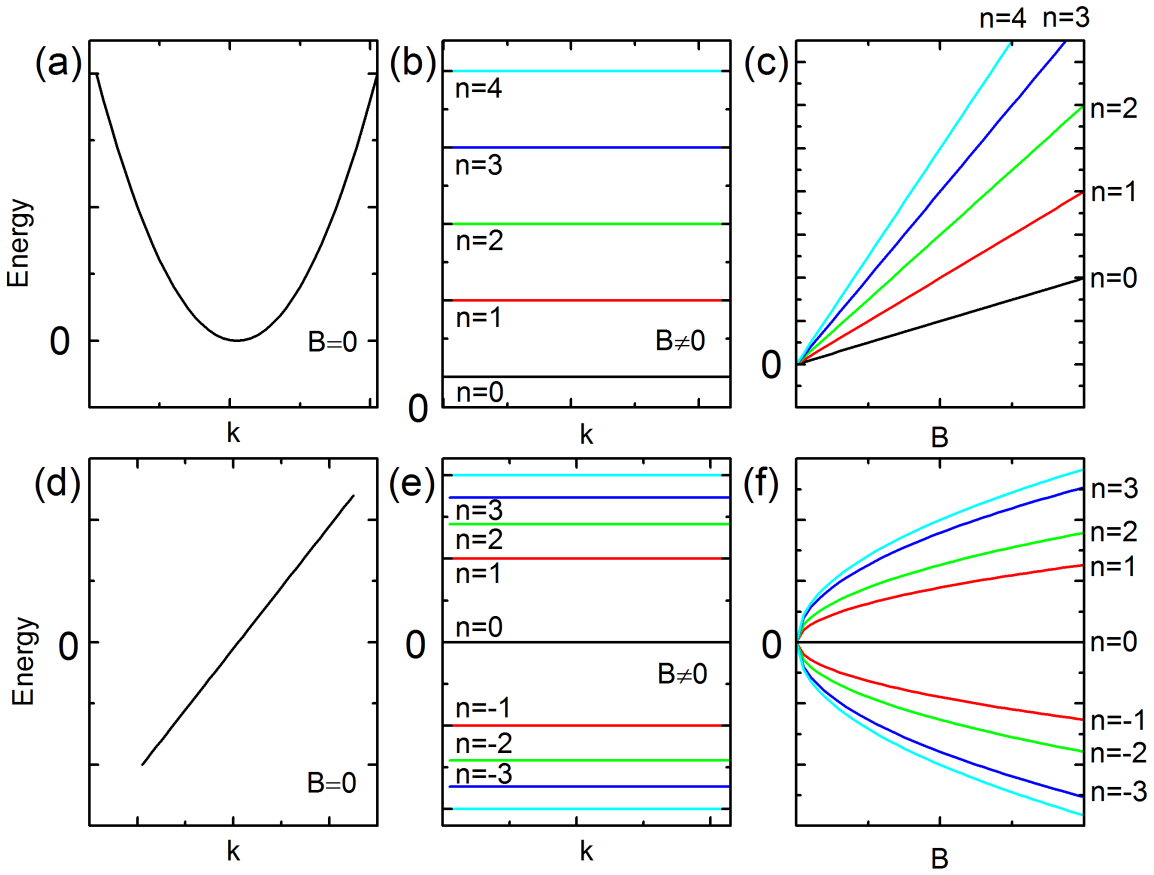

Figure 2.1: LL dispersions from two zero field energy dispersions. In both (a) parabolic and (d) linear cases, a continuous band in zero magnetic field is split into many flat subbands (b)(e) in magnetic fields. However, the dispersions on magnetic fields and the energy gaps between adjacent LLs are different, determined by their zero field dispersions. Specifically, the parabolic band in (a) gives equally spaced LLs (b) and linear dispersions (c) whereas the linear band in (b) gives unevenly spaced LLs (e) and square root dispersion (f). Moreover, in the linear case, the zero LL is pinned at zero energy and there are LLs with negative energy.

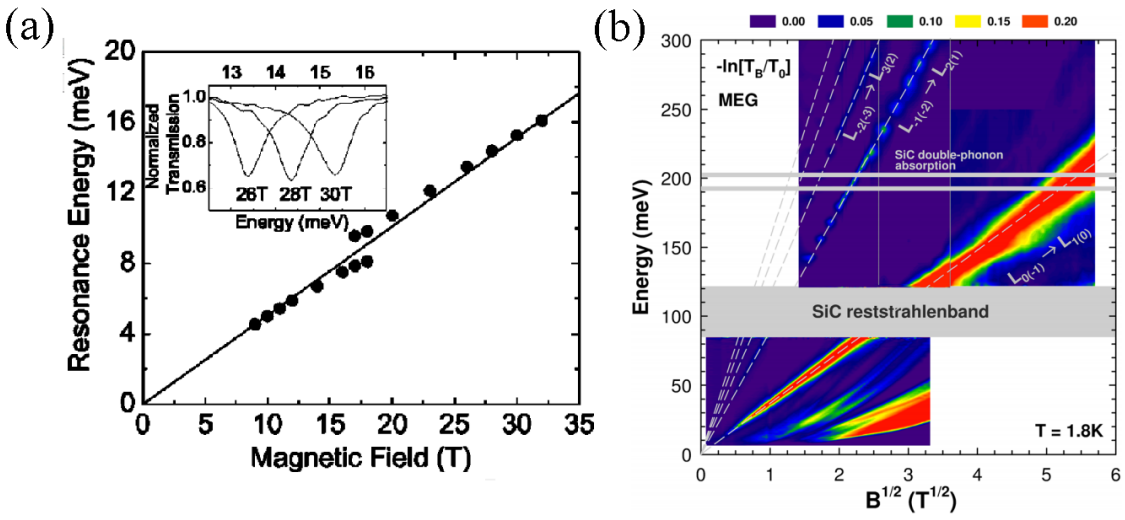

Figure 2.2: LL spectroscopy in GaN and multilayer graphene. (a) Absorption energy as a function of magnetic field in GaN. The solid line is a linear fit assuming a parabolic band. The inset shows transmission data normalized to 0 T at selected fields. (b) False color plot of the relative change of multilayer graphene absorption with the applied magnetic fields. The dash lines are the best fit of the transition energies between different LLs assuming a linear band. Adapted from Refs. [20, 21].

2.2 $\mathbf{k}\cdot\mathbf{p}$ theory

In the above section, the energy bands are ideal and isolated. However, band structures can be much more complicated in reality due to the interactions with adjacent bands. Multiple-band $\mathbf{k}\cdot\mathbf{p}$ theory is a semi-empirical but very successful method for a comprehensive description of complicated energy bands. In this section, we will give a brief introduction on this theory and its application in magnetic fields.

2.2.1 $\mathbf{k}\cdot\mathbf{p}$ model in zero field

The one electron Hamiltonian including the SOI is given by

$$H = \mathbf{p}^2/2m + V + \frac{\hbar}{4m^2c^2}[\nabla V \times \mathbf{p}]\cdot\sigma, \tag{2.14}$$

where V is the potential, c is the speed of light, and σ is the Pauli matrix. In a periodic potential, the Bloch theorem dictates that the eigenstates ψ have the form of

$$\psi = e^{i\mathbf{k}\cdot\mathbf{r}}u(\mathbf{r}), \tag{2.15}$$

where $u(\mathbf{r})$ is the cellular function being periodic within the Brillouin zone. Plugging Eq. (2.15) into Eq. (2.14), the Hamiltonian becomes

$$\begin{aligned} H = \mathbf{p}^2/2m + \hbar^2\mathbf{k}^2/2m + V + (\hbar/m)\mathbf{k}\cdot\mathbf{p} \\ + (\hbar^2/4m^2c^2)[\nabla V \times \mathbf{p}]\cdot\sigma + (\hbar^2/4m^2c^2)[\nabla V \times \mathbf{k}]\cdot\sigma. \end{aligned} \tag{2.16}$$

The term with second order in $\mathbf{k}$ describes the parabolic energy dispersion in a free electron. The last term containing $\nabla V \times \mathbf{k}$ is usually ignored because it gives much smaller contribution than the third terms, due to the fact that the velocity of the electron in its atomic orbit is much greater than that in a wave packet [22]. Note that Eq. (2.16) now only governs the cellular function $u(\mathbf{r})$.

Assuming the solution to the first two terms in Eq. (2.16) is known, then the rest of the Hamiltonian can be treated as a perturbation. This is equivalent to diagonalizing the entire Hamiltonian using the basis functions from the solution to the first two terms. The completeness of the basis functions determines the applicable range and the accuracy of the solutions. Though only limited bands, i.e., basis functions, can be considered in practice, for some materials with as few as 15 bands, the $\mathbf{k}\cdot\mathbf{p}$ model can describe the whole Brillouin zone surprisingly well [23].

Next, we briefly show the formulation of an eight-band $\mathbf{k}\cdot\mathbf{p}$ model for the zincblende structure as an example. We start with four-band model by leaving out the spins, and the perturbation term is the $\mathbf{k}\cdot\mathbf{p}$ term in Eq. (2.16). There are four bands of concerns(Fig. 2.3(a)), the lowest lying CB and three highest lying VB. The three VBs are composed of a heavy hole (HH) and two degenerated light hole (LH) bands. We will show shortly that the

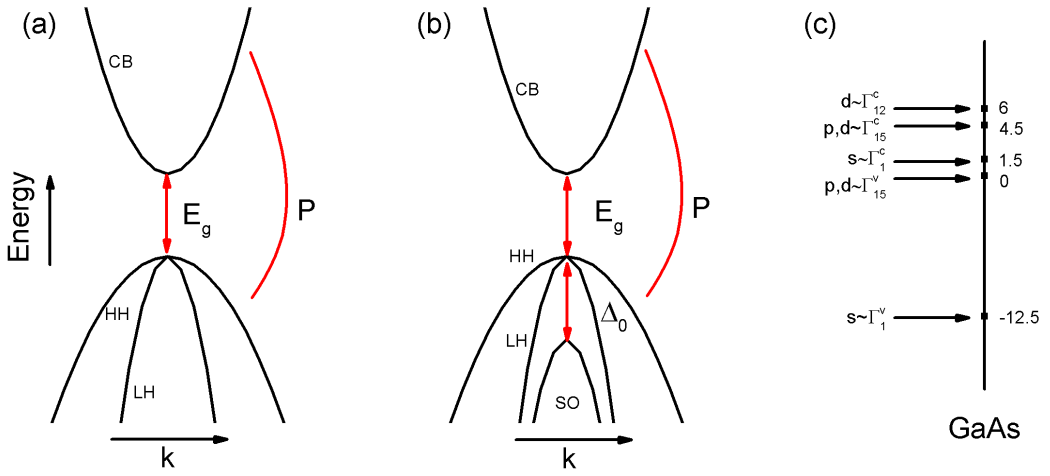

Figure 2.3: $\mathbf{k} \cdot \mathbf{p}$ model in the zincblende structure. In the (a) four-band model, the LH bands are doubly degenerated. The SOI in the (b) eight-band model lifts the degeneracy in LH bands. The band shifted down by Δ_0 is called the SO band. In both models, the CB and VBs are separated by the band gap E_g. P denotes the interaction between CB and VBs. (c) Zone center energy ordering for zincblende structure semiconductor GaAs. The energies on the right side of the line are in eV and the symbols on the left side label the symmetry and the representing basis function of the corresponding energies. Adapted from Ref. [24].

two fold degeneracy in LH will be lifted if SOI is included (Fig. 2.3(b)). Noticing that the wavefunctions in VBs resemble the p orbitals while that in CB is similar to the s orbital in atomic physics, one can choose the following four states $|S\rangle, |X\rangle, |Y\rangle, |Z\rangle$ as basis states.

Though the model only considers four bands, its accuracy can still be improved by taking into account the interaction effects between the four bands of interests and the other (remote) bands (Fig. 2.3(c)). Since there can be partial degeneracies between the bands of interests, a generalized quasi-degenerate perturbation theory [24–26] that can handle degenerate and non-degenerate states together is developed.

The quasi-degenerate perturbation theory (Appendix A) gives a renormalized Hamiltonian

$$H'^{A}_{mn} = H_{mn} + \sum_{\alpha \in B} \frac{H_{m\alpha} H_{\alpha n}}{E - E_\alpha}, \tag{2.17}$$

where $m, n \in A$, $\alpha \in B$, and A and B denote the sets that include the bands of interests

and the remote bands, respectively. Also, $H_{mn} = \langle m| H |n\rangle$, and $|n\rangle$ denotes the eigenstate at band m. Here, the remote bands only contribute in the second order terms as expected from the standard perturbation theory.

The first term in Eq. (2.17) gives the following matrix

$$H^{(1)}_{k\cdot p} = \begin{pmatrix} \epsilon(\mathbf{k}) + E_g & ik_xP & ik_yP & ik_zP \\ & \epsilon(\mathbf{k}) & 0 & 0 \\ & & \epsilon(\mathbf{k}) & 0 \\ & \dagger & & \epsilon(\mathbf{k}) \end{pmatrix},$$

where $\epsilon(\mathbf{k}) = \frac{(\hbar k)^2}{2m}$, E_g is the energy gap between the valence and conduction bands, and $P = -i\frac{\hbar}{m}\langle S|\, p_x\, |X\rangle = -i\frac{\hbar}{m}\langle S|\, p_y\, |Y\rangle = -i\frac{\hbar}{m}\langle S|\, p_z\, |Z\rangle$. The matrix elements can be determined by the symmetry properties of the wavefunctions. In $H_{mn} \propto \mathbf{k}\cdot\langle m|\,\mathbf{p}\,|n\rangle$, the integration is non-vanishing only if the integrand is an even function in all directions. Since the states in valence bands and the momentum operators are odd in one of the axial directions labeled by their subscripts, the only nonzero matrix elements are $\langle S|\, p_x\, |X\rangle$, $\langle S|\, p_y\, |Y\rangle$, and $\langle S|\, p_z\, |Z\rangle$. Moreover, these three nonzero elements are equal because of the degeneracies in $|X\rangle, |Y\rangle$, and $|Z\rangle$.

The second term in Eq. (2.17) accounts for the contribution from the remote bands, which results in

$$H^{(2)}_{k\cdot p} = \begin{pmatrix} A(k_x^2+k_y^2+k_z^2) & Bk_yk_z & Bk_xk_z & Bk_xk_y \\ & Lk_x^2 + M(k_y^2+k_z^2) & Nk_xk_y & Nk_xk_z \\ & & Lk_y^2 + M(k_x^2+k_z^2) & Nk_yk_z \\ & \dagger & & Lk_z^2 + M(k_x^2+k_y^2) \end{pmatrix}.$$

Here, the details of the parameters will not be listed but can be found in Ref. [24]. As an

example, we briefly show the derivation of the parameters in matrix element H_{22}. In H_{22},

$$\sum \frac{H_{x\alpha}H_{\alpha x}}{E_v - E_\alpha} = \frac{\hbar^2}{m_0^2}\sum \frac{|k_x \langle x| p_x |\alpha\rangle + k_y \langle x| p_y |\alpha\rangle + k_z \langle x| p_z |\alpha\rangle|^2}{E_v - E_\alpha}$$
$$= \frac{\hbar^2}{m_0^2}\sum \frac{(|k_x \langle x| p_x |\alpha\rangle|^2 + |k_y \langle x| p_y |\alpha\rangle|^2 + |k_z \langle x| p_z |\alpha\rangle|^2)}{E_v - E_\alpha}.$$

The cross terms vanish in the second equality because the allowed symmetries for the matrix elements of different momenta do not overlap. For example, $\langle x| p_x |\alpha\rangle$ is nonzero for state $|\alpha\rangle$ with Γ_1 and Γ_{12} symmetries while $\langle x| p_y |\alpha\rangle$ is nonzero for state $|\alpha\rangle$ with Γ_{15} and Γ_{25} symmetries. Apparently, there is no symmetry for both terms in $\langle x| p_x |\alpha\rangle \langle \alpha| p_y |x\rangle$ to be simultaneously nonzero. In addition, the summation in the second line runs over bands with different allowed symmetries (Fig.2.3(c)): the allowed symmetry in $\langle x| p_x |\alpha\rangle$ is different from $\langle x| p_y |\alpha\rangle$ and $\langle x| p_z |\alpha\rangle$. Therefore, H_{22} amounts to $Lk_x^2 + M(k_y^2 + k_z^2)$, where

$$L = \frac{\hbar^2}{m_0^2}\sum_{\alpha}^{\Gamma_1,\Gamma_{12}} \frac{|k_x \langle x| p_x |\alpha\rangle|^2}{E_v - E_\alpha}, \quad M = \frac{\hbar^2}{m_0^2}\sum_{\alpha}^{\Gamma_{15},\Gamma_{25}} \frac{|k_y \langle x| p_y |\alpha\rangle|^2}{E_v - E_\alpha}.$$

The rest of the matrix elements can be derived similarly.

Next, we consider the SOI. First, the basis states need to be expanded to include the spin degree of freedom

$$|S,\uparrow\rangle, |X,\uparrow\rangle, |Y,\uparrow\rangle, |Z,\uparrow\rangle, |S,\downarrow\rangle, |X,\downarrow\rangle, |Y,\downarrow\rangle, |Z,\downarrow\rangle.$$

Here, $|\uparrow\rangle$ and $|\downarrow\rangle$ denote the spinnors for spin up and spin down. The Hamiltonian regarding the $\mathbf{k}\cdot\mathbf{p}$ perturbation terms expands into an 8 by 8 matrix:

$$\begin{pmatrix} H_A & 0 \\ 0 & H_A \end{pmatrix}.$$

The spin-orbit term can be calculated from the orbital and spin parts separately

$$H_{so} = \frac{\hbar \mathbf{k}}{4m^2c^2} \cdot \langle i| \left[\nabla V \times \mathbf{p}\right]_k |j\rangle \cdot \langle s_i| \sigma |s_j\rangle ,$$
$$\text{where} \quad |i\rangle , |j\rangle = |S\rangle , |X\rangle , |Y\rangle , |Z\rangle , \quad |s\rangle = |\uparrow\rangle , |\downarrow\rangle .$$

The spin part is very straightforward and the orbital part can be simplified using symmetry arguments. As a result of the rotational symmetries in the zincblende structure, the indices i, j, k in $\langle i| (\nabla V \times \mathbf{p})_k |j\rangle$ must be different in order to have a nonzero matrix element and these non-zero elements are again equal. In addition, the SOI only couples within the VBs but not the CB, which means that all the matrix elements involving $|S\rangle$ are zero. With this, the H_{so} Hamiltonian reads

$$H_{so} = \frac{\Delta}{3} \begin{pmatrix} 0 & 0 & 0 & 0 & 0 & 0 & 0 & 0 \\ 0 & 0 & -i & 0 & 0 & 0 & 0 & 1 \\ 0 & i & 0 & 0 & 0 & 0 & 0 & -i \\ 0 & 0 & 0 & 0 & 0 & -1 & i & 0 \\ 0 & 0 & 0 & 0 & 0 & 0 & 0 & 0 \\ 0 & 0 & 0 & -1 & 0 & 0 & i & 0 \\ 0 & 0 & 0 & -i & 0 & -i & 0 & 0 \\ 0 & 1 & i & 0 & 0 & 0 & 0 & 0 \end{pmatrix} ,$$

where $\Delta = \frac{3i\hbar}{4m_0^2c^2}$.

The H_{SO} Hamiltonian can be diagonalized

$$H'_{so} = \frac{\Delta}{3}\begin{pmatrix} 0 & 0 & 0 & 0 & 0 & 0 & 0 & 0 \\ 0 & 0 & 0 & 0 & 0 & 0 & 0 & 0 \\ 0 & 0 & 1 & 0 & 0 & 0 & 0 & 0 \\ 0 & 0 & 0 & 1 & 0 & 0 & 0 & 0 \\ 0 & 0 & 0 & 0 & 1 & 0 & 0 & 0 \\ 0 & 0 & 0 & 0 & 0 & 1 & 0 & 0 \\ 0 & 0 & 0 & 0 & 0 & 0 & -2 & 0 \\ 0 & 0 & 0 & 0 & 0 & 0 & 0 & -2 \end{pmatrix},$$

using the following basis states

$$\begin{aligned}
&\phi_1 = |\frac{1}{2}, \frac{1}{2}\rangle = |S\uparrow\rangle, \phi_2 = |\frac{1}{2}, -\frac{1}{2}\rangle = |S\downarrow\rangle, \\
&\phi_3 = |\frac{3}{2}, \frac{3}{2}\rangle = \frac{1}{\sqrt{2}}|(X+iY)\uparrow\rangle, \phi_4 = |\frac{3}{2}, \frac{1}{2}\rangle = \frac{i}{\sqrt{6}}|(X+iY)\downarrow -2Z\uparrow\rangle, \\
&\phi_5 = |\frac{3}{2}, -\frac{1}{2}\rangle = \frac{1}{\sqrt{6}}|(X-iY)\uparrow +2Z\downarrow\rangle, \phi_6 = |\frac{3}{2}, -\frac{3}{2}\rangle = \frac{i}{\sqrt{2}}|(X-iY)\downarrow\rangle, \\
&\phi_7 = |\frac{1}{2}, \frac{1}{2}\rangle = \frac{1}{\sqrt{3}}|(X+iY)\downarrow +Z\uparrow\rangle, \phi_8 = |\frac{1}{2}, -\frac{1}{2}\rangle = -\frac{i}{\sqrt{3}}|(X-iY)\uparrow -Z\downarrow\rangle.
\end{aligned}$$

One can easily see that the spin-orbit term only lifts the degeneracy in the two degenerated LH bands. Now the lower band is called the split-off (SO) band. The new basis states are linear combinations of the old basis states. It is easy to calculate a transformation matrix S that connects the two basis so that one can transform into the new basis states using $H_{new} = S^{-1}H_{old}S$.

Finally, we have reached the Kane Hamiltonian for zincblende crystals near the Γ point

[27]:

$$H = \begin{pmatrix} A & 0 & i\sqrt{3}V^\dagger & \sqrt{2}U & iV & 0 & iU & \sqrt{2}V \\ 0 & A & 0 & -V^\dagger & i\sqrt{2}U & -\sqrt{3}V & i\sqrt{2}V^\dagger & -U \\ -i\sqrt{3}V & 0 & -P-Q & L & M & 0 & \frac{i}{\sqrt{2}}L & -i\sqrt{2}M \\ \sqrt{2}U & -V & L^\dagger & -P+Q & 0 & M & i\sqrt{2}Q & i\sqrt{\frac{3}{2}}L \\ -iV^\dagger & -i\sqrt{2}U & M^\dagger & 0 & -P+Q & -L & -i\sqrt{\frac{3}{2}}L^\dagger & i\sqrt{2}Q \\ 0 & -\sqrt{3}V^\dagger & 0 & M^\dagger & -L^\dagger & -P-Q & -i\sqrt{2}M^\dagger & -\frac{i}{\sqrt{2}}L^\dagger \\ -iU & -i\sqrt{2}V & -\frac{i}{\sqrt{2}}L^\dagger & -i\sqrt{2}Q & i\sqrt{\frac{3}{2}}L & i\sqrt{2}M & -P-\Delta & 0 \\ \sqrt{2}V^\dagger & -U & i\sqrt{2}M^\dagger & -i\sqrt{\frac{3}{2}}L^\dagger & -i\sqrt{2}Q & \frac{i}{\sqrt{2}}L & 0 & -P-\Delta \end{pmatrix} \tag{2.18}$$

$$\begin{aligned} \text{where} \quad A &= E_v + E_g + \mathbf{k}A_c\mathbf{k}, \quad P = -E_v + \frac{\hbar^2}{2m}\mathbf{k}\gamma_1\mathbf{k}, \\ Q &= \frac{\hbar^2}{2m}(k_x\gamma_2 k_x + k_y\gamma_2 k_y - 2k_z\gamma_2 k_z), \\ M &= -\frac{\sqrt{3}\hbar^2}{2m}[k_x\gamma_2 k_x - k_y\gamma_2 k_y - 2i\{k_x\gamma_3 k_y\}], \\ L &= i\frac{\sqrt{3}\hbar^2}{m}\{k_-\gamma_3 k_z\}, \quad U = \frac{Pk_z}{\sqrt{3}}, \quad V = \frac{Pk_-}{\sqrt{6}}. \end{aligned}$$

In the above formula, $\{k_\beta\gamma k_\alpha\} = \frac{k_\beta\gamma k_\alpha + k_\alpha\gamma k_\beta}{2}, \alpha, \beta = x, y, z$, and $k_\pm = k_x \pm ik_y$. Δ is the SO splitting of the LH bands. The interaction strength between the CBs and VBs P is related to the Kane parameter E_p by $E_p = \frac{2m}{\hbar^2}P^2$. $\gamma_1, \gamma_2, \gamma_3$ are the Luttinger parameters. γ_2 and γ_3 are often set to be their average to simplify the calculation. This is called axial approximation since the anisotropy in the plane is neglected.

Figure 2.4 shows the band structure of GaSb calculated with the above eight-band $\mathbf{k}\cdot\mathbf{p}$ model and compared with a first-principles calculation [28]. There are two things to note here. First, as expected from the perturbation theory and the use of incomplete basis states, the $\mathbf{k}\cdot\mathbf{p}$ model is only valid in a narrow range around Γ point. Second, comparing Figs. 2.4(a) and (b), the bands are symmetrized under the axial approximation.

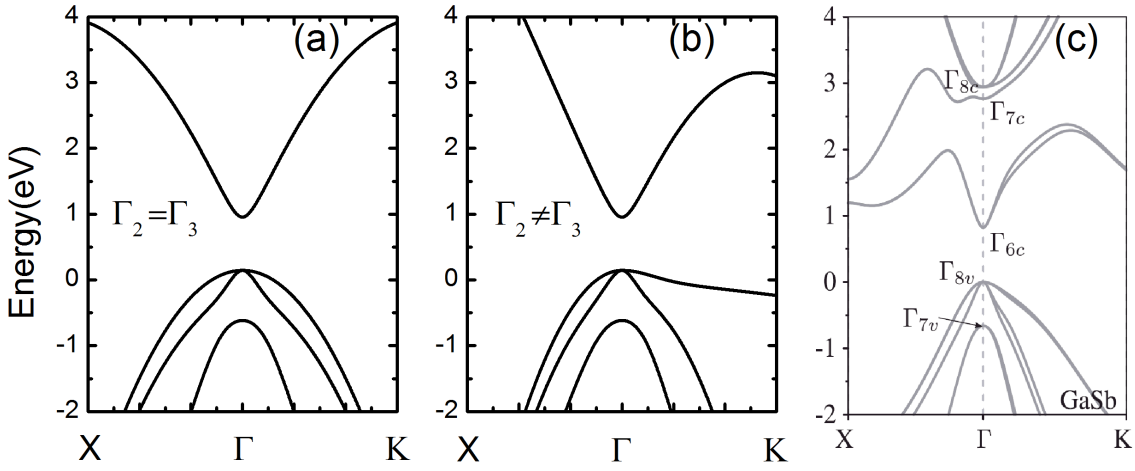

Figure 2.4: Band structure of GaSb calculated using $\mathbf{k}\cdot\mathbf{p}$ model. Band structure from Γ to X[010] and K[110] (a) with and (b) without axial approximation. (c) The energy band of GaSb obtained from first-principles calculation. The spin splitting in (c) is due to the inversion asymmetry in zincblende structure which is not included in the $\mathbf{k}\cdot\mathbf{p}$ calculation. (c) Adapted from Ref. [28].

2.2.2 $\mathbf{k}\cdot\mathbf{p}$ model in magnetic field

In a magnetic field $\mathbf{B} = (0, 0, B)$ and with the same Landau gauge as before, we again replace the momentum with the canonical momentum. One can easily prove the following relations

$$k_+Ak_- + k_-Ak_+ = 2(k_xAk_x + k_yAk_y), k_-Ak_+ - k_+Ak_- = 2i(k_xAk_y - k_yAk_x),$$
$$k_-Ak_- - k_+Ak_+ = -2i(k_xAk_y + k_yAk_x), k_+Ak_+ + k_-Ak_- = 2(k_xAk_x - k_yAk_y),$$

and use them to rewrite the Hamiltonian matrix elements in terms of the ladder operators

$$A = E_v + E_g + \frac{1}{l_c^2}(a^\dagger A_c a + a A_c a^\dagger) + k_z A_c k_z,$$
$$P = -E_v + \frac{\hbar^2}{2m_0}[\frac{1}{l_c^2}(a^\dagger \gamma_1 a + a\gamma_1 a^\dagger) + k_z \gamma_1 k_z],$$
$$Q = \frac{\hbar^2}{2m_0}[\frac{1}{l_c^2}(a^\dagger \gamma_2 a + a\gamma_2 a^\dagger) - 2k_z \gamma_2 k_z],$$
$$M = \frac{\sqrt{3}\hbar^2}{2m_0}\frac{1}{l_c^2}[(\gamma_3 - \gamma_2)(a^\dagger)^2 - (\gamma_3 + \gamma_2)(a)^2],$$
$$L = i\frac{\sqrt{3}\hbar^2}{m_0}\frac{\sqrt{2}}{l_c}\{a\gamma_3 k_z\}, \quad U = \frac{P_0 k_z}{\sqrt{3}}, \quad V = \frac{\sqrt{2}a}{l_c}\frac{P_0}{\sqrt{6}}.$$

In the axial approximation, the trial solution to the above Hamiltonian has a nice form

$$\Psi_{p,\mu}(x,y,z) \propto e^{ik_x x} \begin{bmatrix} a_{p,1,\mu}(z) & \phi_{n-1}(y) \\ a_{p,2,\mu}(z) & \phi_n(y) \\ a_{p,3,\mu}(z) & \phi_{n-2}(y) \\ a_{p,4,\mu}(z) & \phi_{n-1}(y) \\ a_{p,5,\mu}(z) & \phi_n(y) \\ a_{p,6,\mu}(z) & \phi_{n+1}(y) \\ a_{p,7,\mu}(z) & \phi_{n-1}(y) \\ a_{p,8,\mu}(z) & \phi_n(y) \end{bmatrix}, \tag{2.19}$$

where p is the Pigeon-Brown (PB) index, μ denotes the band order within the same PB index, ϕ_p is the pth order Harmonic oscillator eigenfunction, and $a(z)$ is the wavefunction along the z direction. For a given eigenfunction $\Psi_{p,\mu}$, different components of the electron wavefunction are in different but related excited states denoted by different LL indices in the subscript of ϕ in each spinor component. Therefore, it is important for p to consistently refer to the same spinor component to unambiguously define the eigenstate. In this thesis, p is taken to be the same as the LL index in the second spinor component and from now on n will be replaced by p. This connection also determines the range of p. Since the LL

index can only take all the non-negative integers, any ϕ with a negative LL index is set to 0. The lowest possible value for p is thus -2, below which the solution will be trivial.

After operation onto Eq. (2.19), the Hamiltonian in magnetic fields H_L is now casted into an algebric matrix as a function of p and magnetic field B

$$H_L = \begin{pmatrix} A_{p-1} & 0 & i\sqrt{3}V_{p-1}^* & \sqrt{2}U & iV_p & 0 & iU & \sqrt{2}V_p \\ & A_p & 0 & -V_p^* & i\sqrt{2}U & -\sqrt{3}V_{p+1} & i\sqrt{2}V_p^* & -U \\ & & -S_{p-2} & L_{p-1} & M_p & 0 & \frac{i}{\sqrt{2}}L_{p-1} & -i\sqrt{2}M_p \\ & & & -T_{p-1} & 0 & M_{p+1} & i\sqrt{2}Qp-1 & i\sqrt{\frac{3}{2}}L_p \\ & & & & -T_p & -L_{p+1} & -i\sqrt{\frac{3}{2}}L_p^* & i\sqrt{2}Q_p \\ & & \dagger & & & -S_{p+1} & -i\sqrt{2}M_{p+1}^* & -\frac{i}{\sqrt{2}}L_{p+1}^* \\ & & & & & & -P_{p-1}-\Delta & 0 \\ & & & & & & & -P_p-\Delta \end{pmatrix},$$

where $A_p = E_v + E_g + A_c(k_z^2 + \frac{2p+1}{l_c^2}), \quad P_p = -E_v + \frac{\hbar^2}{2m}\gamma_1(k_z^2 + \frac{2p+1}{l_c^2}A_c),$

$$Q_p = \frac{\hbar^2}{2m}\gamma_2(\frac{2p+1}{l_c^2}A_c - 2k_z^2), \quad M_p = -\frac{\sqrt{3}\hbar^2}{2m}\frac{\sqrt{p(p-1)}}{l_c^2}(\gamma_2+\gamma_3),$$

$$S_p = P_p + Q_p, \quad T_p = P_p - Q_p, \quad L = i\frac{\sqrt{3}\hbar^2}{m}\frac{\sqrt{2p}\gamma_3}{l_c}k_z, \quad U = \frac{Pk_z}{\sqrt{3}}, \quad V_p = \sqrt{\frac{2p}{6}}\frac{P}{l_c},$$

and $*$ denotes conjugate operations.

When calculating the lowest few PB manifolds, i.e., $p = -1, 0, 1$, due to the zero spinor components, the corresponding columns and rows in the Hamiltonian matrix will be struck out, reducing the dimensions of the Hamiltonian. For example, if $p = -2$, the Hamiltonian is reduced to a 1 by 1 matrix since only the H_{66} element will survive. Consequently, the number of eigenenergies in different p can also be different.

Finally, we wish to include the Zeeman effect with the following Hamiltonian [29]

$$H_Z = \frac{\hbar^2}{m_0 l_c^2} \begin{pmatrix} \frac{1}{2} & 0 & 0 & 0 & 0 & 0 & 0 & 0 \\ 0 & -\frac{1}{2} & 0 & 0 & 0 & 0 & 0 & 0 \\ 0 & 0 & -\frac{3}{2}\kappa & 0 & 0 & 0 & 0 & 0 \\ 0 & 0 & 0 & -\frac{1}{2}\kappa & 0 & 0 & i\sqrt{\frac{1}{2}}(\kappa+1) & 0 \\ 0 & 0 & 0 & 0 & \frac{1}{2}\kappa & 0 & 0 & -i\sqrt{\frac{1}{2}}(\kappa+1) \\ 0 & 0 & 0 & 0 & 0 & \frac{3}{2}\kappa & 0 & 0 \\ 0 & 0 & 0 & -i\frac{\kappa+1}{\sqrt{2}} & 0 & 0 & -(\kappa+\frac{1}{2}) & 0 \\ 0 & 0 & 0 & 0 & i\frac{\kappa+1}{\sqrt{2}} & 0 & 0 & \kappa+\frac{1}{2} \end{pmatrix},$$

where $\kappa = \gamma_3^L + \frac{2}{3}\gamma_2^L - \frac{1}{3}\gamma_1^L - \frac{2}{3} - \frac{E_p}{6E_g}$, and the Luttinger parameters $\gamma_1^L, \gamma_2^L, \gamma_3^L$ can be connected to the modified Luttinger parameters $\gamma_1, \gamma_2, \gamma_3$ in Eq. (2.2.1) through the following relations

$$\gamma_1 = \gamma_1^L - \frac{E_p}{3E_g}, \quad \gamma_2 = \gamma_2^L - \frac{E_p}{6E_g}, \quad \gamma_3 = \gamma_3^L - \frac{E_p}{6E_g}.$$

The above Hamiltonian apparently has contributions other than just the Zeeman term

$$H_Z = -g_e \mu_B B \sigma, \tag{2.20}$$

where g_e is the electron g-factor and μ_B is the Bohr magneton. The additional contribution comes from the asymmetry of the second order momentum matrices in the parameters [30]. In general, these momentum matrices can be written as

$$D_{mn} = \sum_{i,j} D_{mn}^{ij} k_i k_j = \sum_{\alpha,i,j} \langle m| p_i |\alpha\rangle \langle \alpha| p_j |n\rangle k_i k_j,$$

and they need not be symmetric, i.e., $D^{ij}_{mn} \neq D^{ji}_{mn}$. We can further rewrite them as

$$D_{mn} = \frac{1}{4}\sum_{i,j}\Big[\{D^{ij}_{mn}, D^{ji}_{mn}\}\{k_i, k_j\} + [D^{ij}_{mn}, D^{ji}_{mn}][k_i, k_j]\Big],$$

where $\{A, B\} = AB - BA$ and $[A, B] = AB + BA$. Without magnetic fields, k_i and k_j commute and $\{D^{ij}_{mn}, D^{ji}_{mn}\}$ vanishes. In magnetic fields, commuting k_i and k_j will produce a term proportional to magnetic field B and the contribution from $\{D^{mn}_{ij}, D^{mn}_{ji}\}$ can not be dropped.

2.2.3 Selection rules and absorption spectra

As discussed in Section 2.1, electrons/holes can be excited to higher energy states by absorbing photons with suitable energies. This process can be described using the famous Fermi's golden rule [5]:

$$\Gamma_{i,f} = \frac{2\pi}{\hbar}|\langle f|\, H'\, |i\rangle\,|^2\delta(E_f - E_i - \hbar\omega)[f_i(E_F) - f_f(E_F)], \tag{2.21}$$

where Γ is the transition probability per unit of time from initial state $|i\rangle$ at energy E_i to final state $|f\rangle$ at energy E_f, $f_s(E_F)$ is the Fermi distribution for state s with Fermi energy E_F, ω is the incident light frequency, and H' is the perturbing Hamiltonian from the electromagnetic field of the incident light.

Equation. (2.21) has several immediate consequences. First, transitions only happen when the incident photon energy matches the transition energy between the initial and final states as constrained by the delta function. Second, the intial and final states can not be fully empty nor filled. Otherwise, the transition is blocked by the Pauli exclusive principle described by the difference of the Fermi distribution. Lastly, if the perturbing Hamiltonian H' has certain symmetries, the initial and final states must also be connected with certain symmetries to ensure a nonzero matrix element. The resulting connection is called the selection rule. With all these knowledges, we can calculate the magneto-absorption spectra.

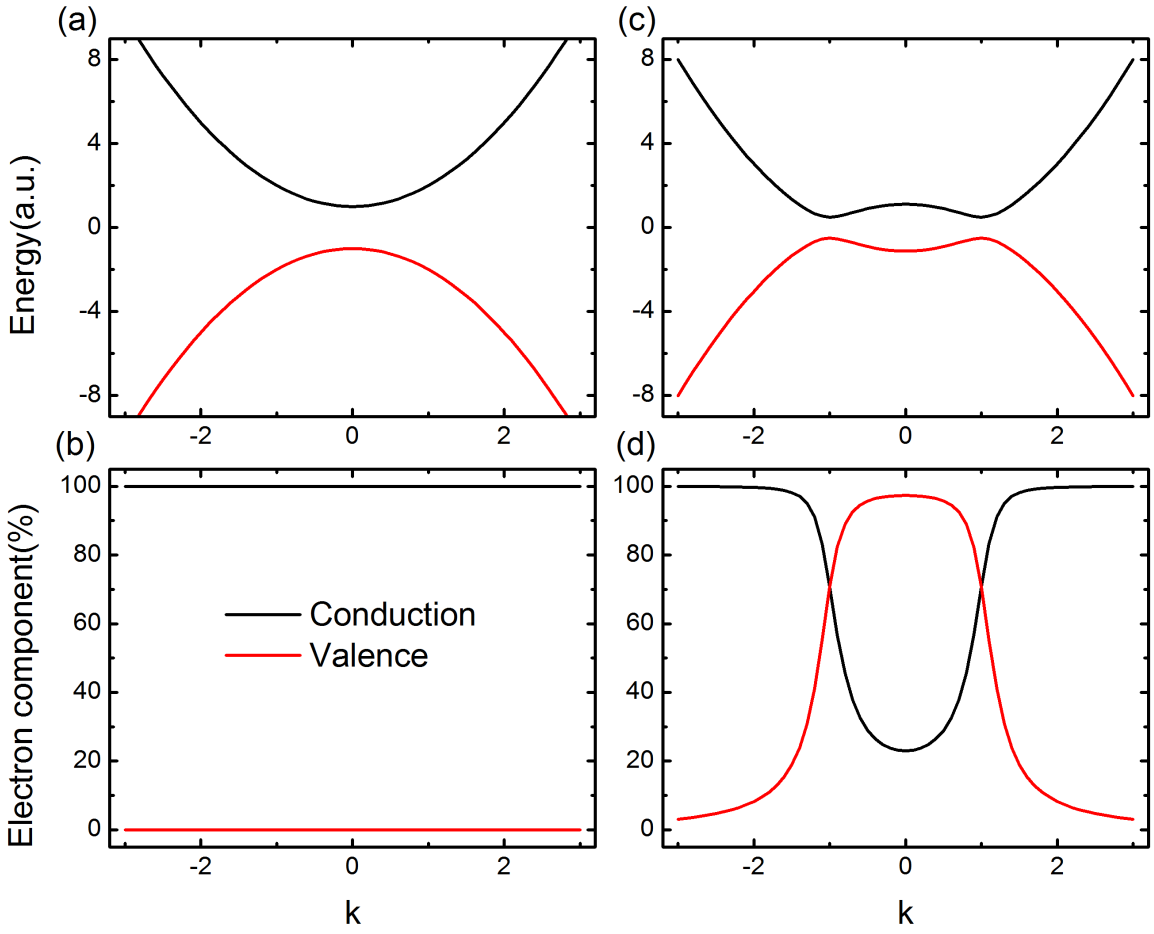

Figure 2.5: Wavefunction components in a two-band model. Energy band structures of a (a) normal band, where there is no overlap between the CB (black) and VB (red), and an (c) inverted band, where level repulsion occurs at the crossing of two bands and opens a small gap at finite k. Comparing the electron components in the wavefunctions for CB and VB for (b) normal and (d) inverted bands, one may find that they are no longer dominated by a single component once they interact. The hole component can be calculated by (1− the electron component).

Let us start with the Fermi level. In eight-band $\mathbf{k}\cdot\mathbf{p}$ calculations, the bands involved are two CBs and six VBs. In magnetic fields, each band splits into subbands which are labeled by the PB index p and another index μ for their energy position within the same PB index. For an intrinsic sample, the Fermi level should be lying within the lowest CB (subband) and the highest VB (subband) in zero (nonzero) magnetic field. For a doped sample, the Fermi level can be determined by removing or filling electrons starting from the intrinsic Fermi level till the desired doping level. Here, we want to emphasize that the electron (hole) component in the spinor wavefunction does not necessarily determine the band states, i.e., CB or VB. This is illustrated using a simple two-band model (Fig. 2.5). In a normal band, the wavefunctions of the CB (VB) are dominated by electron (hole) components. In an inverted band, however, the CB (VB) can have hole (electron) as dominant components. Therefore, wavefunctions only describe the distribution of electrons/holes but have nothing to do with the definition of the band states. In fact, the band states can be defined by their relative positions to the intrinsic Fermi level. If a band is above (below) the intrinsic Fermi level, then it is a CB (VB).

The Fermi energy can be calculated by solving the equations relating the doping levels with the carrier contributions from all the CBs and VBs through the hole/electron Fermi statistics described below. In the case of zero field,

$$f_n = \frac{1}{1+exp[(E_n(k_x,k_y)-E_F)/kT]}, \qquad N_c = \frac{1}{(2\pi)^2}\int dk_x dk_y [f_n - \delta_n^v], \tag{2.22}$$

whereas in magnetic field,

$$f_{p,\mu} = \frac{1}{1+exp[(E_{p,\mu}-E_F)/kT]}, \qquad N_c = g\sum_{p,\mu}[f_{p,\mu} - \delta_{p,\mu}^v], \tag{2.23}$$

where T is the temperature, k is the Boltzmann constant, E_F is the Fermi level, and N_c is the doping level. $\delta_{n,\mu}^v$ is the delta function accounting for the band states, which is 1 for VB and 0 for CB. g is the LL degeneracy.

In Eq. (2.21), the perturbing Hamiltonian H' is the leading term in the expansion of the perturbing field $\sim \mathbf{P} \cdot \mathbf{A}$, which gives the electric dipole transition [5]. When the leading term vanishes, the second term in the expansion will be considered, which is the magnetic dipole transition and gives a different selection rule. Here, we will focus on the electric dipole transition.

For electric dipole transition, the matrix element is proportional to

$$\hat{\mathbf{e}} \cdot \vec{\mathbf{P}}_{p,\mu}^{p',\mu'} = \sum_{m,m'} a^*_{p,m,\mu} a_{p',m',\mu'} \left\langle \phi_{N(p,m)} | \phi_{N(p',m')} \right\rangle \left\langle m \right| \left(\hat{\mathbf{e}} \cdot \vec{\mathbf{P}} \right) \left| m' \right\rangle ,$$

where $\hat{\mathbf{e}}$ is the polarization of the incident light, m denotes the spinor component, and $\langle m| \left(\hat{\mathbf{e}} \cdot \tilde{\mathbf{P}} \right) |m'\rangle$ are the momentum matrix elements between the mth and m'th Bloch basis states [29]. $\langle \phi_{N(p,m)} | \phi_{N(p',m')} \rangle$ will either be 1 or zero owing to their orthogonal relation.

It is not difficult to write down the momentum matrix

$$P_x = \begin{pmatrix}
0 & 0 & i\frac{P}{\sqrt{2}} & 0 & i\frac{P}{\sqrt{6}} & 0 & 0 & \frac{P}{\sqrt{3}} \\
0 & 0 & 0 & -\frac{P}{\sqrt{6}} & 0 & -\frac{P}{\sqrt{2}} & i\frac{P}{\sqrt{3}} & 0 \\
 & & 0 & 0 & 0 & 0 & 0 & 0 \\
 & & & 0 & 0 & 0 & 0 & 0 \\
 & & & & 0 & 0 & 0 & 0 \\
 & & \dagger & & & 0 & 0 & 0 \\
 & & & & & & 0 & 0 \\
 & & & & & & & 0
\end{pmatrix},$$

$$P_y = \begin{pmatrix} 0 & 0 & -\frac{P}{\sqrt{2}} & 0 & \frac{P}{\sqrt{6}} & 0 & 0 & -i\frac{P}{\sqrt{3}} \\ & 0 & 0 & -i\frac{P}{\sqrt{6}} & 0 & i\frac{P}{\sqrt{2}} & -\frac{P}{\sqrt{3}} & 0 \\ & & 0 & 0 & 0 & 0 & 0 & 0 \\ & & & 0 & 0 & 0 & 0 & 0 \\ & & & & 0 & 0 & 0 & 0 \\ & & \dagger & & & 0 & 0 & 0 \\ & & & & & & 0 & 0 \\ & & & & & & & 0 \end{pmatrix}.$$

By inspecting the optical matrices P_x and P_y, i.e., linear light polarized in x or y direction, only transitions satisfying $\Delta p = \pm 1$ are allowed. This can be also understood with angular momentum conservation. If the incident light is circular polarized, then the matrix elements can be written as:

$$P_{\sigma^+} = (P_{\sigma^-})^\dagger = P_x + iP_y = \begin{pmatrix} 0 & 0 & 0 & 0 & i\frac{2P}{\sqrt{6}} & 0 & 0 & \frac{2P}{\sqrt{3}} \\ 0 & 0 & 0 & 0 & 0 & -\frac{2P}{\sqrt{2}} & 0 & 0 \\ -i\frac{2P}{\sqrt{6}} & 0 & 0 & 0 & 0 & 0 & 0 & 0 \\ 0 & -\frac{2P}{\sqrt{6}} & 0 & 0 & 0 & 0 & 0 & 0 \\ 0 & 0 & 0 & 0 & 0 & 0 & 0 & 0 \\ 0 & -i\frac{2P}{\sqrt{3}} & 0 & 0 & 0 & 0 & 0 & 0 \\ 0 & 0 & 0 & 0 & 0 & 0 & 0 & 0 \\ 0 & 0 & 0 & 0 & 0 & 0 & 0 & 0 \end{pmatrix}.$$

Apparently, the $p \to p+1$ ($p \to p-1$) transition is only allowed for σ^+ (σ^-) polarized light, which is also termed as electron (hole) like transition.

Finally, we are ready to calculate the energy dependence of the absorption coefficient

combining the above results [29],

$$\alpha(\hbar\omega) \propto \frac{e^3}{(\hbar c)^2 n_r}\frac{B}{\hbar\omega}\sum_{p,\mu,p',\mu'}|\hat{\mathbf{e}}\cdot\vec{\mathbf{P}}_{p,\mu}^{p',\mu'}|^2 \times (f_{p,\mu}-f_{p',\mu'})\delta(\Delta E_{p,\mu}^{p',\mu'}-\hbar\omega).$$

Here, n_r is the refraction index, (p,μ) and (p',μ') denote the final and initial states and $\hat{\mathbf{e}}\cdot\vec{\mathbf{P}}_{p,\mu}^{p',\mu'}$ are the optical matrix elements introduced above. The summation goes over all the possible pairs of bands. Fortunately, this calculation is greatly simplified by the selection rule.

2.3 BHZ model

The BHZ model was first introduced by Bernevig, Hughes and Zhang [8] to describe the electronic structure of HgTe/CdTe QW. Later, the BHZ model was generalized to 3D by the method of invariants [31]. In essence, the BHZ model is still a $\mathbf{k}\cdot\mathbf{p}$ model but it provides an effective analytical form of Hamiltonian that can quantitatively describe the low-energy dispersion of the bands.

2.3.1 BHZ model in zero field

Both HgTe and CdTe are also zincblende structure [32]. The $\mathbf{k}\cdot\mathbf{p}$ Hamiltonian in Eq. (2.2.1) is still valid except to replace the k_z with a momentum operator due to the quantum confinement effect [8]. The low-energy electronic structure of HgTe/CdTe QW involves the two lowest CBs $(|E1,\uparrow\rangle, |E2,\downarrow\rangle)$ and the two highest VBs $(|H1,\uparrow\rangle, |H2,\downarrow\rangle)$ of interests and also contributions from many other bands. For simplicity, we can simplify the Hamiltonian by projecting it into the subspace spanned by the desired bands while keeping the contributions from the other bands. The projection is done by

$$H'_{ij} = \langle\phi_i| H_{k.p} |\phi_i\rangle, \quad i,j = 1,2,3,4, \tag{2.24}$$

where 1-4 denote the four bands of interests. The Hamiltonian can be further simplified by projecting out the extra dimension

$$H_{ij} = \int_{-\infty}^{+\infty} \langle \phi_i | \, H_{k.p} \, | \phi_i \rangle \, dz, \quad i, j = 1, 2, 3, 4. \tag{2.25}$$

In HgTe/CdTe QW, the simplified Hamiltonian [8] is

$$H(\mathbf{k}) = \epsilon_0(\mathbf{k}) + \begin{pmatrix} L(\mathbf{k}) & Ak_+ & 0 & 0 \\ Ak_- & -L(\mathbf{k}) & 0 & 0 \\ 0 & 0 & L(\mathbf{k}) & -Ak_- \\ 0 & 0 & -Ak_+ & -L(\mathbf{k}) \end{pmatrix}, \tag{2.26}$$

where $\epsilon_0(\mathbf{k}) = C - D(k_x^2 + k_y^2)$ and $L(\mathbf{k}) = M - \mathscr{B}(k_x^2 + k_y^2)$. Here, the parameters A, $\mathscr{B}$, C, D and E depend not only on the material but also on the specific QW structure because of the integration in Eq. (2.25).

The resulting energy dispersion is

$$E_\pm = \epsilon(\mathbf{k}) \pm \sqrt{A^2\mathbf{k}^2 + (M - \mathscr{B}\mathbf{k}^2)^2}, \tag{2.27}$$

where $\pm$ represent the CBs and VBs. Around the Γ point, if the square root term dominates and $\mathscr{B}$ is 0, Eq. (2.27) resembles the energy-momentum relation in the massive Dirac equation [15]

$$E = \pm\sqrt{(pc)^2 + (m_0c^2)^2}. \tag{2.28}$$

Because of this similarity, electrons following the square root relation are also called Dirac fermions. Parameter A is acting like the "speed of the light" in the material, which is connected to the Fermi velocity, $A = \hbar v_f$. The band gap at Γ point is solely determined by the parameter M corresponding to the mass term in the massive Dirac equation. When a

system is gapless, $M = 0$ and the electrons are called massless Dirac fermions, otherwise massive Dirac fermions. Interesting, parameter M can be also negative which implies that the lowest CB lies below the highest VB as an inverted band structure, while a positive M implies a normal case. The $\mathscr{B}$ term is similar to the non-relativistic mass term [13] in that the energy exhibits quadratic dependence on momentum. Parameter D in $\epsilon(k)$ term breaks the symmetry in energy between CB and VB, since C only shifts the overall energy and is normally set to 0.

It turns out that the Hamiltonian for 3D TIs derived from the method of invariants [31] is nearly the same as the BHZ model in 2D,

$$H(\mathbf{k}) = \epsilon_0(\mathbf{k}) + \begin{pmatrix} L(\mathbf{k}) & A(k)k_+ & 0 & -\mathscr{B}(k_z)k_z \\ A(k)k_- & -L(\mathbf{k}) & \mathscr{B}(k_z)k_z & 0 \\ 0 & \mathscr{B}(k_z)k_z & L(\mathbf{k}) & -A(k)k_- \\ -\mathscr{B}(k_z)k_z & 0 & -A(k)k_+ & -L(\mathbf{k}) \end{pmatrix},$$

where the generalized parameters are $\epsilon_0(\mathbf{k}) = C_0 + C_1k_z^2 + C_2(k_x^2 + k_y^2), A(k) = A_0 + A_2(k_x^2 + k_y^2), L(\mathbf{k}) = M_0 + M_1k_z^2 + M_2(k_x^2 + k_y^2)$, and $\mathscr{B}(k_z) = \mathscr{B}_0 + \mathscr{B}_2k_z^2$. Apparently, once the k_z is set to 0, it reduces to the 2D BHZ model. This makes the BHZ model extremely useful when describing the electronic structure of 2D and 3D TIs.

Finally, it is interesting to show the edge states within the BHZ model [33]. Specifically, the edge state can be solved with an open boundary condition, where the region for $y > 0$ is the QW structure and $y < 0$ is vacuum. In the x direction, the system extends infinitely far. Since the Hamiltonian is in a block diagonal form of two 2 by 2 matrices, the solution can be obtained for each block individually. Here, we will focus on the upper block, that is

$$H = \begin{pmatrix} M - B_+(k_x^2 - \partial_y^2) & A(k_x - \partial_y) \\ A(k_x + \partial_y) & -M + B_-(k_x^2 - \partial_y^2) \end{pmatrix},$$

where $B_\pm = \mathscr{B} \pm D$ and k_y is now replaced by the operator ∂_y since in this direction the

translational invariance is violated. The trial solution is

$$\phi = \begin{pmatrix} c \\ d \end{pmatrix} e^{\lambda y},$$

where λ can be obtained by solving the eigenenergy equation $H\phi = E\phi$. After substituting the trial solution into the Hamiltonian, we get

$$\lambda_{1,2}^2 = k_x^2 + F \pm \sqrt{F^2 - \frac{M^2 - E^2}{\mathscr{B}^2 - D^2}},$$

where $F = \frac{A^2 - 2(M\mathscr{B} + ED)}{2(\mathscr{B}^2 - D^2)}$. The E term can be eliminated using the boundary condition requiring the wavefunction to decay at $y = 0$ and $+\infty$, that is

$$\begin{pmatrix} c \\ d \end{pmatrix} (e^{-\lambda_1 y} - e^{-\lambda_2 y}).$$

Again, applying the Hamiltonian onto this general solution, the nontrivial solution of c and d can be obtained , which leads to

$$E = M - (\mathscr{B} + D)\lambda_1\lambda_2 - (\mathscr{B} + D)(\lambda_1 + \lambda_2)k_x - (\mathscr{B} + D)k_x^2.$$

At $k_x = 0$,

$$E = M - (\mathscr{B} + D)\lambda_1\lambda_2,$$
$$\lambda_1 = \sqrt{F - \sqrt{F^2 - \frac{M^2 - E^2}{\mathscr{B}^2 - D^2}}},$$
$$\lambda_2 = \sqrt{F + \sqrt{F^2 - \frac{M^2 - E^2}{\mathscr{B}^2 - D^2}}}.$$

Plugging F into the above formula, we have

$$\lambda_1\lambda_2 = \frac{M}{\mathscr{B}}, \qquad \lambda_1 + \lambda_2 = \sqrt{\frac{A^2}{\mathscr{B}^2 - D^2}}.$$

Since the existence of edge states requires $\lambda_1 > 0$ and $\lambda_2 > 0$, it is equivalent to

$$\mathscr{B}^2 > D^2, \qquad M/\mathscr{B} > 0. \tag{2.29}$$

2.3.2 BHZ model in magnetic field

The procedure to solve the BHZ model in magnetic field is similar to that in the $\mathbf{k}\cdot\mathbf{p}$ model. Hre, we briefly show the derivation in 2D and the 3D case follows similarly.

In magnetic fields, the Hamiltonian (2.26) can be rewritten with ladder operators, giving

$$H = \begin{pmatrix} H_{up} & 0 \\ 0 & H_{down} \end{pmatrix}, \tag{2.30}$$

$$\text{where} \quad H_{up} = \begin{pmatrix} (C+M) - (D+\mathscr{B})\frac{2}{l_c^2}(a^\dagger a + \frac{1}{2}) & A\frac{\sqrt{2}}{l_c}a^\dagger \\ A\frac{\sqrt{2}}{l_c}a & (C-M) - (D-\mathscr{B})\frac{2}{l_c^2}(a^\dagger a + \frac{1}{2}) \end{pmatrix},$$
$$H_{down} = \begin{pmatrix} (C+M) - (D+\mathscr{B})\frac{2}{l_c^2}(a^\dagger a + \frac{1}{2}) & -A\frac{\sqrt{2}}{l_c}a \\ -A\frac{\sqrt{2}}{l_c}a^\dagger & (C-M) - (D-\mathscr{B})\frac{2}{l_c^2}(a^\dagger a + \frac{1}{2}) \end{pmatrix}. \tag{2.31}$$

As indicated by the basis states, the upper (lower) block describes the spin up (down) state. Therefore one can add the following simple Hamiltonian for the Zeeman effect

$$H_{Zeeman} = \frac{\mu_B B}{2}\begin{pmatrix} g_e & 0 & 0 & 0 \\ 0 & g_h & 0 & 0 \\ 0 & 0 & -g_e & 0 \\ 0 & 0 & 0 & -g_h \end{pmatrix}, \tag{2.32}$$

where g_e (g_h) is the effective g factors for CBs (VBs).

In the upper block, the trial solution has the form

$$\psi = \begin{pmatrix} |n\rangle \\ |n-1\rangle \end{pmatrix},$$

where $|n\rangle$ again denotes the nth harmonic oscillator eigenfunction. Next, we will discuss the $n = 0$ and $n \neq 0$ cases. When $n = 0$, the $|n-1\rangle$ is ill-defined and therefore it is set to 0. The eigenenergy is exactly the first diagonal element

$$E_0^{\downarrow} = (C+M) - \frac{(D+\mathscr{B})B}{l_c^2} + \frac{\mu_B g_e}{2} B. \tag{2.33}$$

When $n \neq 0$, we have

$$\begin{pmatrix} (C+M) - (D+\mathscr{B})\frac{2}{l_c^2}(n+\frac{1}{2}) + \frac{\mu_B g_e}{2}B & A\frac{\sqrt{2n}}{l_c} \\ A\frac{\sqrt{2n}}{l_c} & (C-M) - (D-\mathscr{B})\frac{2}{l_c^2}(n+\frac{1}{2}) + \frac{\mu_B g_h}{2}B \end{pmatrix}. \tag{2.34}$$

The resulting eigenenergy is

$$E_n^{\uparrow} = C - (2Dn+\mathscr{B})\frac{eB}{\hbar} + \frac{\bar{Z}}{2}B \pm \sqrt{2A^2 n\frac{eB}{\hbar} + [M - (2\mathscr{B}n + D)\frac{eB}{\hbar} + \frac{\delta z}{2}B]^2}, \tag{2.35}$$

where $\delta z = \mu_B \frac{g_e - g_h}{2}$, $\bar{Z} = \mu_B \frac{g_e + g_h}{2}$. The lower block can be solved in a similar fashion.

Combining the solutions from upper and lower blocks, the complete solution can be

summarized as

$$
\begin{aligned}
&E_0^{\uparrow} = C + M - (D + \mathscr{B})\frac{eB}{\hbar} + \frac{\mu_B g_e}{2}B, \quad E_0^{\downarrow} = C - M - (D - \mathscr{B})\frac{eB}{\hbar} - \frac{\mu_B g_h}{2}B, \\
&E_n^s = C - (2Dn + s\mathscr{B})B + s\frac{\bar{Z}}{2}B \\
&\qquad + \alpha\sqrt{2A^2nB + (M - (2\mathscr{B}n + sD)B + s\frac{\delta z}{2}B)^2}, \quad n \neq 0
\end{aligned}
\tag{2.36}
$$

where $s = \pm 1$ for spin up and down and $\alpha = \pm 1$ for CBs and VBs.

Figure 2.6 plots the LL dispersions for normal ($M > 0$) and inverted ($M < 0$) band structures. It is easy to notice that the band dispersions in these two situations are almost identical except that the zero energy modes switch their positions. In the inverted state, the zero energy modes cross at a high enough magnetic field, which can be calculated by substracting the zero energy modes in Eq. (2.36)

$$
E_0^{\uparrow} - E_0^{\downarrow} = 2M - 2\mathscr{B}\frac{eB}{\hbar} + \frac{\mu_B(g_e - g_h)}{2}B. \tag{2.37}
$$

If the g-factor difference is ignored, the two zero energy modes will meet at $B = \frac{\hbar}{e}\frac{M}{\mathscr{B}}$ when $\frac{M}{\mathscr{B}} > 0$. This is consistent with the condition for the existence of the edge states. Therefore, this crossing can be viewed as an indication of the TI phase.

Under the condition $\frac{M}{\mathscr{B}} > 0$, if M and $\mathscr{B}$ change sign simultaneously, the H_{up} block switches its position with H_{down} block. In other words, the solutions for different spins exchange. In Fig. 2.6(b), the LL dispersions will remain the same but the colors are expected to switch.

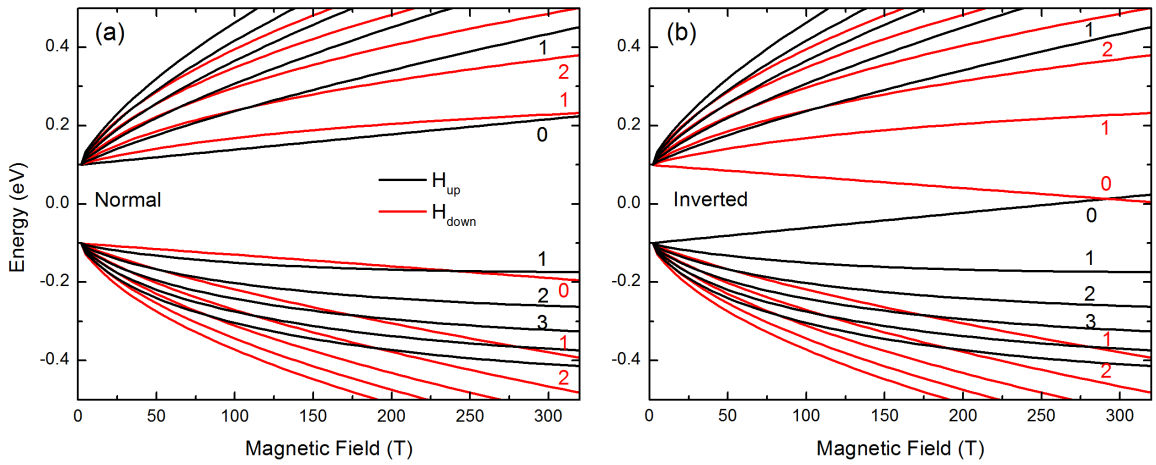

Figure 2.6: LL dispersions in the BHZ model. LL dispersions in the (a) normal and (b) inverted band states. The parameters are taken to be $M = 0.1$ eV, $\mathscr{B} = -22.5$ eVÅ^2, $D = -3$ eVÅ^2, $A = \sqrt{|4M\mathscr{B}|}$, and $g_e = g_h = 0$ for the normal state. In the inverted state, only the sign of M changes and the zero energy modes cross at a sufficiently high magnetic field. The black and red colors represent the solutions from the upper and lower blocks.

CHAPTER 3

EXPERIMENT TECHNIQUES

In LL spectroscopy experiment, the probing lights need have comparable energy with the LL spacing, which can be estimated by the cyclotron resonance(CR) and the Zeeman energy of charge carrier. With bare electron mass, both energy scales are comparable ($\frac{e\hbar}{m}B \sim \mu_B B \sim 5$ cm^{-1}/T). Note that in infrared (IR) spectroscopy, wavenumber cm^{-1} is a very common unit for energy and the translation to eV is 1 meV = 8.065 cm^{-1}. Within the accessible magnetic field $B < 35$ T, this energy range is covered by the far-IR light ($E < 800$ cm^{-1}). The mid-IR ($800 < E < 8000$ cm^{-1}) and near-IR ($8000 < E < 16000$ cm^{-1}) regions also cover a rich variety of phenomena in correlated electron systems (Fig. 3.1), which makes IR spectroscopy a powerful tool to probe electronic structures and many-body interactions. In addition, unlike electrical transport measurements, optical spectroscopy techniques (1) require almost no fabrication process and induce very little contamination, and (2) can be either bulk or surface sensitive depending on the specific spectroscopy techniques. The latter is critically important in separating and studying the edge/surface states in TIs.

The goal of a spectroscopic measurement is to capture the response of a system such as transmission, absorption or reflection to the probing lights. There are two different spectrum acquisition techniques. The most common one is to probe a system with monochromatic light and then repeat the process at a different frequency until the whole energy region is covered. A less intuitive way is to measure a convoluted response to boradband light (i.e., lights composed of a wide range of frequency) in real space and then translated back to frequency space through Fourier transformations. Such method using IR light is called Fourier transform infrared spectroscopy (FTIR). In this chapter, we will introduce both techniques and discuss how to couple them with a magnetic field.

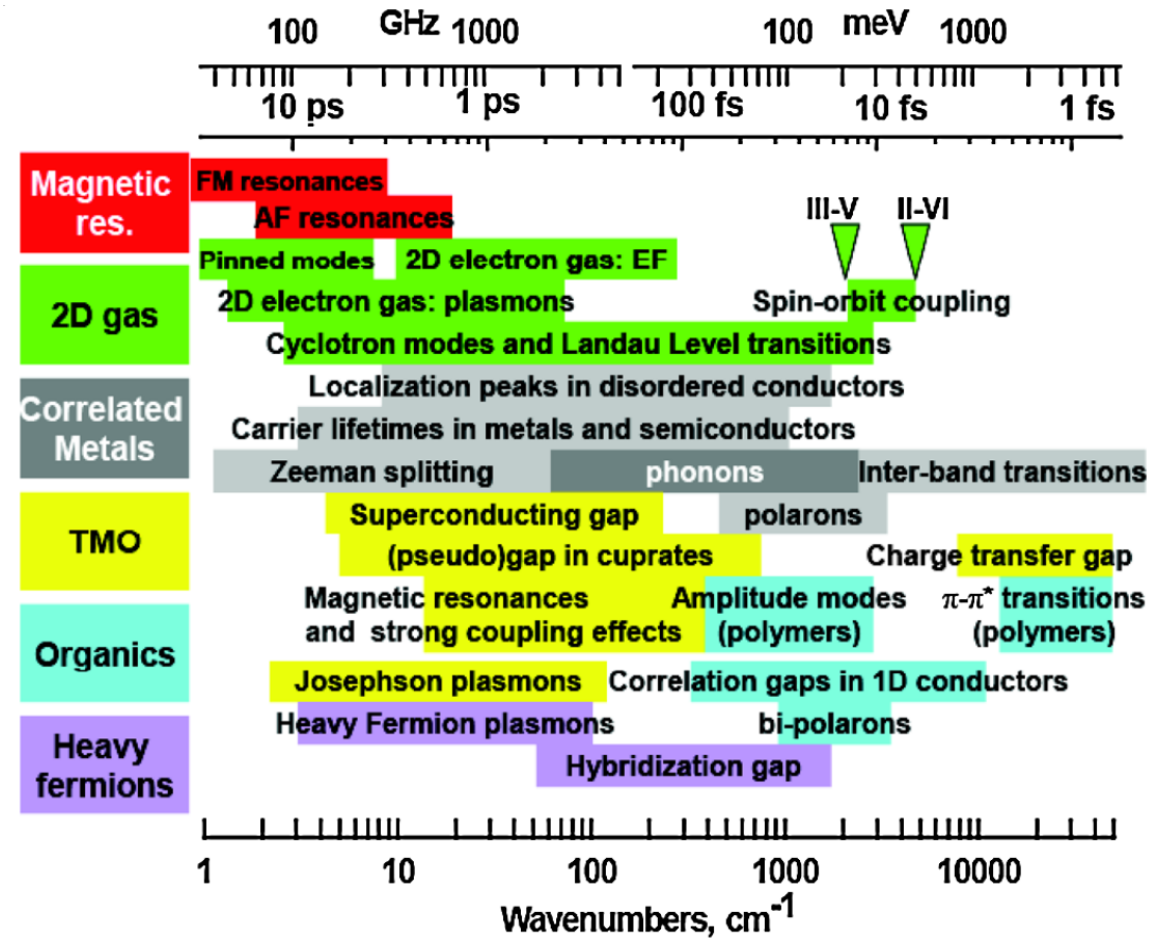

Figure 3.1: Energy scale in correlated electron systems. Schematic representation of characteristic energy scales of physics phenonmena in correlated electron system. The IR range covers almost the whole region starting from 10 cm^{-1}. Adapted from Ref. [34].

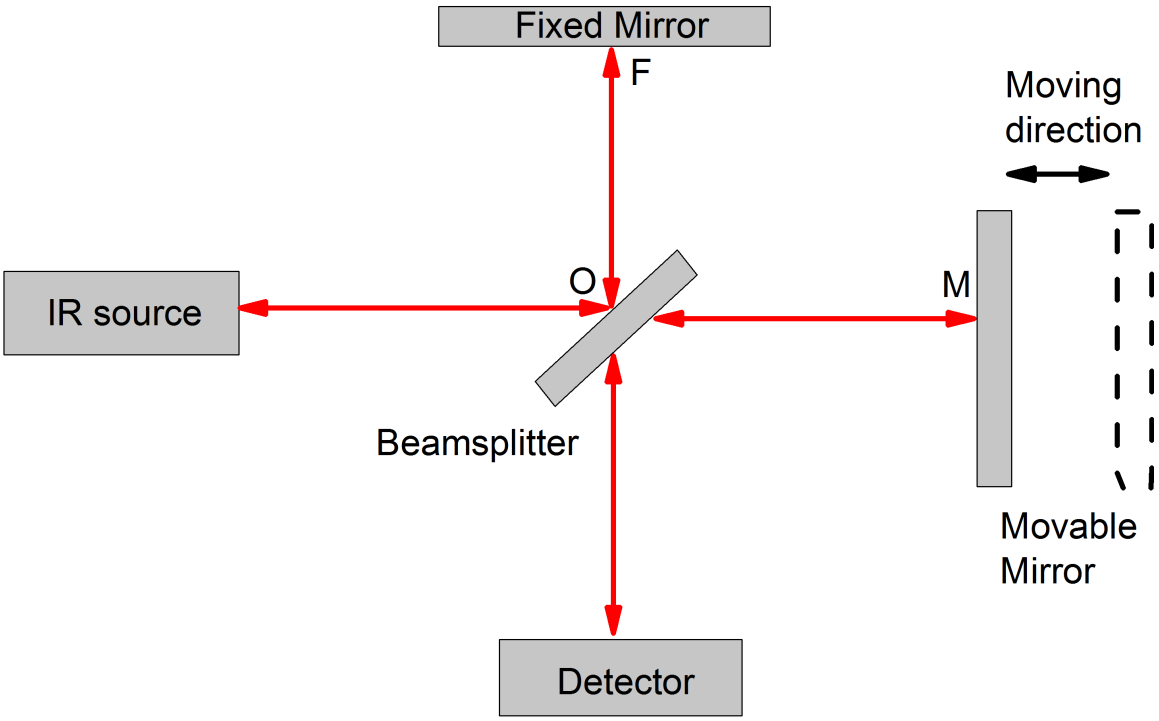

Figure 3.2: Schematic drawing of an interferometer. A beamsplitter splits the incoming light from an IR source. The reflected and transmitted light recombines after bouncing back from a fixed and a movable mirror which produces an optical path difference.

3.1 Fourier trasnform infrared spectrometry

The key component of a FTIR spectrometer is a Michelson interferometer (Fig. 3.2). In such an interferometer, the light from the IR source is split into two beams by a beamsplitter and then recombined after reflecting from two mirrors. One mirror is fixed while the other one is movable along the light traveling direction, which produces an optical path difference between the two paths. The intensity of the recombined light was recorded against the position of the movable mirror, which is called an interferogram.

If the incident light is monochromatic, the recombining lights can interfere constructively or destructively as the optical path difference varies. It is easy to imagine that the intensity has an oscillatory waveform in period with the incident light frequency in the interferogram. If the incident light is polychromatic, the interferogram profile may not be that intuitive but in principle is just the superposition of the contributions from each

monochromatic light.

In mathematics, a monochromatic light can be described by a plane wave:

$$E(k,x) = E_0(k)e^{i(\omega t - 2\pi kx)}, \tag{3.1}$$

where E, ω, k are the electric field, frequency and wave vector of the incident light, respectively, and x denotes the traveling distance along the light path. When the lights recombine at the beamsplitter, the optical path difference δ is $2(OM - OF)$ (Fig. 3.2). Assuming the traveling distance of the reflected light after reflecting from the fixed mirror is x_0 at the beamsplitter, the recombined light is described as

$$E(k,\delta) = \frac{E_0(k)}{2}e^{i(\omega t - 2\pi kx_0)}(1 + e^{-2\pi ik\delta}), \tag{3.2}$$

and the intensity is

$$I(\delta) = E(k,\delta)E^*(k,\delta) = \frac{E_0^2(k)}{2}(1 + \cos(2\pi k\delta)). \tag{3.3}$$

Here, we assume that the mirrors have perfect reflection and the beamsplitter reflects and transmits light in 50/50 percents. If the light is polychromatic, we need to integrate over the whole frequency range

$$I(\delta) = \int_0^{+\infty} \frac{B_0(k)}{2}(1 + \cos(2\pi k\delta))dk, \tag{3.4}$$

where $B_0(k)$ denotes the spectral density of the source. Equation (3.4) is just a Fourier transformation. Therefore, $B_0(k)$ can be calculated from $I(\delta)$ using inverse Fourier transformation

$$B_0(k) = \int_0^{+\infty} \frac{I_(\delta)}{2}(1 + \cos(2\pi k\delta))dk. \tag{3.5}$$

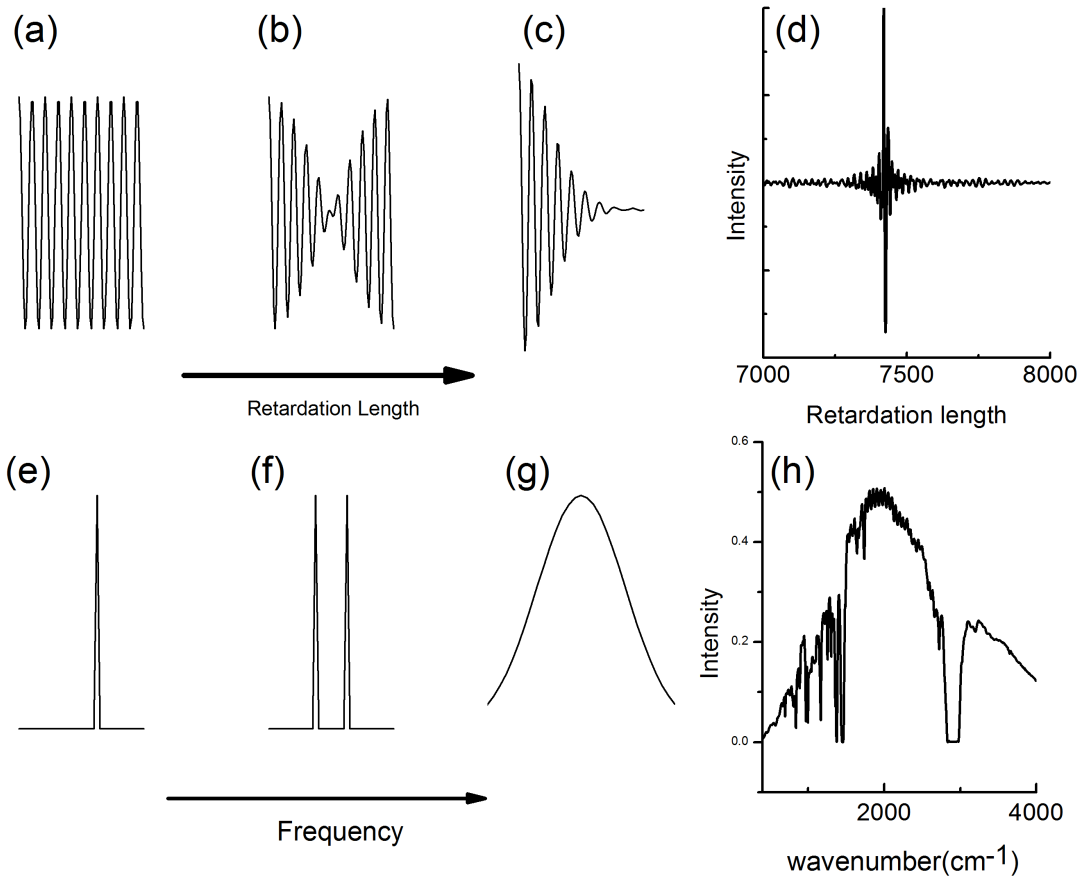

Figure 3.3: Translations between interferogram and spectra. The top and bottom rows show the translation between inteferrogram and spectra for (a) (e) single, (b) (f) double, (c) (g) broadband light with Gaussian broadening in frequency, and in (d) (h) a real example, respectively.

Figure 3.3 shows several examples of the translations between the spectra and the interferograms. For a monochromatic wave, the interferogram is a cosine wave and extends to infinite far. For a broadband light, the interferogram is confined within a small range. Because of this close correlation, noise suppression is very important since any disturbance may introduce noise over the whole spectral range. It is also important to note that the interferogram is a convolution of all the contributions from the objects on the light paths such as air, beamsplitters and samples. Thus, a proper reference is always needed to resolve the desired effects.

There are three essential components in a FTIR spectrometer (Fig. 3.2): broadband sources, beamsplitters, and detectors.

Many broadband IR sources take adavantage of blackbody radiations. Objects at temperature T can emit lights of all frequencies and the spectral energy density I can be calculated through the Planck's law

$$I(\nu, T) = \frac{2h\nu^3}{c^2} \frac{1}{e^{\frac{h\nu}{kT}} - 1}, \tag{3.6}$$

where c is the speed of light, ν is the frequency of the light, and h is the Planck constant. A simple calculation gives the peak intensity at the energy of $2.82kT$ (Wien's displacement law). A typical broadband mid-IR source is a SiC rod heated up to 1300 K with a peak intensity around $\sim$ 2500 cm^{-1}. Due to its bar shape, it is also called globar. In the far-IR region, the power density of the blackbody radiation decays very quickly. From the Planck's law, the power density from a 1400 K blackbody radiation at 100 cm^{-1} is about 1600 times less than that at 1000 cm^{-1}. The intensity can be much improved by using a high-pressure mercury lamp due to the high electron temperature in the ionized gas plamsa (equivalent to $\sim$ 10000 K) [35].

For broadband optics, transparent materials with feature-less transmission spectra in the energy region of interest are highly desirable. Since IR lights cover energy range of many characteristic absorptions such as phonon absorption bands or vibrational and rotational modes in chemical bonds, many visible transparent materials can only extend to the near-IR range but become opaque or have many absorption lines in the mid-IR or far-IR range. A beamsplitter is even more demanding since it needs to balance the reflected and transmitted lights. The maximum light intensity after recombination at the beamsplitter is $2RT$ of the light source intensity, where R and T are the reflectance and transmittance of the beamsplitter, respectively. Assuming $R + T = 1$, $2RT$ reaches a maximum of 0.5 when $R = T = 0.5$. Therefore, a good beamsplitter should approach this value as much as possible over a wide energy range. In general, a thin film with high refractive index is desirable to meet the above requirements [36]. In addition, the thickness of the thin film

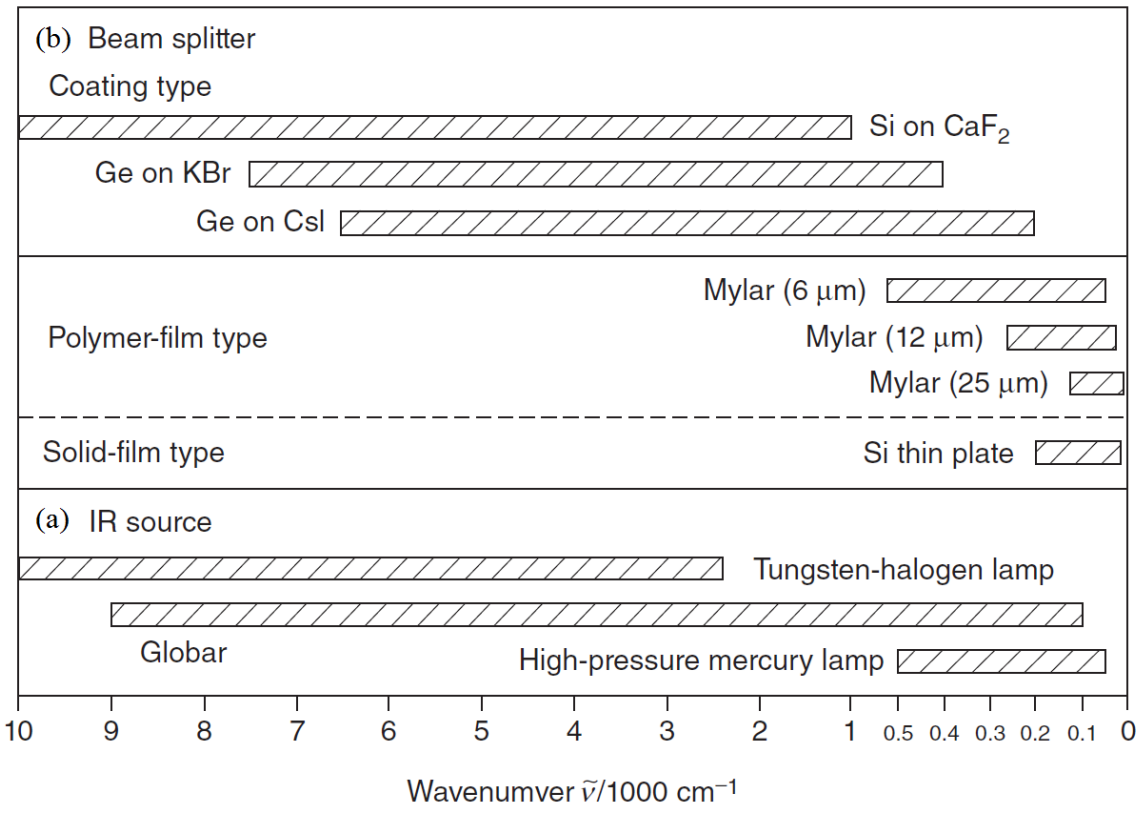

Figure 3.4: IR sources and beamsplitters. Applicable energy range for different (a) IR sources and (b) beamsplitters. Adapted from Ref. [35].

should also be carefully chosen because the interference between the incident and the internally reflected light also affects the intensity of the delivered light from the beamsplitter. In the mid-IR range, a high refractive index film such as germanium or silicon is employed and coated on a transparent supporting substrate made of ionic compounds such as KBr or CaF. In the far-IR range where the wavelength is from tens to hundreds μm, the thickness effect becomes prominent and optimization of the thickness in different spectral regions of interest is important. Mylar (polyethylene terephthalate) films are commonly used in far-IR beamsplitters since many ionic compounds are opaque in this region. Moreover, one can further improve the performance of a Mylar beamsplitter with germanium coating [36]. Figure 3.4 summarizes the applicable energy range for some popular beamsplitters and light sources.

There are two major types of IR detectors: quantum detectors and thermal detectors

[36]. A quantum detector takes advantage of the fact that electrons by absorbing photons can be excited to a higher energy state. In many semiconductors, the excitation is through interband transitions since a photocurrent can be generated by the excited electrons and the holes left behinds. The detecting region is lower bounded by the band gap which can be engineered in multiple ways. For example, in $Hg_{1-x}Cd_xTe$, the band gap can be tuned via the Cd concentration. A thermal detector operates by monitoring temperature sensitive properties of an absorbing material. Pyroelectric bolometers such as DTGS (deuterated triglycine sulfate) and DLaTGS (deuterated lanthanum alanine doped triglycine sulphate) sense the temperature induced change in electrical polarization in ferroelectric materials. The degree of changes in polarization reflects the amount of IR radiations absorbed. In low temperature and far-IR measurement, liquid helium cooled semiconductor bolometers out-perform both the pyroelectric and quantum detectors in sensitivity [37]. The absorbing semiconductors are brought to the metal-insulator transition regime by appropriate doping so that the resistance is highly sensitive to the temperature change [38]. In addition, the low temperature environment suppresses thermal related noise and instability. The temperature can be further lowered to 1.4 K by pumping on the helium bath for higher sensitivity.

Compared to other optical spectroscopy techniques, FTIR is very efficient in measuring a wide energy range due to its unique operating principle. In addition, since each measurement contains information over whole spectral range, it allows for easy means of averaging to reduce noise. Finally, this technique can achieve high resolution in spectrum, benefiting from precise measurement of the mirror position advanced by laser technology and refrain from the use of a slit. Therefore, maximum light intensity can be delivered to samples to improve the signal-to-noise ratio.

3.2 Quantum cascade laser

Semiconductor lasers are based on the recombination of electrons and holes across band gaps (Fig. 3.5(a)). These lasers do not offer tunability in a wide range because the emitting

light frequency is mostly determined by the band gap of the material. In addition, due to the opposite curvature of the CBs and VBs, semiconductor lasers have a relatively broad linewidth (Fig. 3.5(b)).

Quantum cascade laser (QCL) is based on intersubband transitions instead of interband transitions in a multiple QW heterostructure [39], in which the quantum confinement effect can split a continuous band into many subbands described by the following relation

$$E_{n,k} = \frac{\hbar^2}{2m^*}(\frac{\pi^2 n^2}{L^2} + k_{\|}), \tag{3.7}$$

where $k_{\|}$ is the momentum in plane, L is the width of the QW, m^* is the effective mass, and n denotes the subbands. It is easy to see that these subbands have the same curvatures. Therefore, the output from a QCL has a much sharper linewidth (Fig. 3.5(b)). More importantly, because the band gap now can be tailored by different L without changing the material, it is possible to stack several QWs of different L together to make a tunable laser without reducing the lasing quality.

As all lasers, the central engineering problem is to maximize the population inversion. It is desirable to have

$$\tau_{relax} < \tau_{excited},$$

where τ denotes the relaxation time. Figure 3.6(a) shows one simplest realization of a QCL unit, which is composed of two regions: an active region and an injected region under an applied electric field. The active region is a DQWs where the laser transitions take place between the $n = 3$ and $n = 2$ states. To ensure a large population inversion, τ_2 is designed to be much shorter than τ_3 to prevent accumulation in the lower energy states. This is achieved by aligning the energy gap between the $n = 2$ and $n = 1$ states to a longitudinal optical (LO) phonon energy of the QW materials so that the electrons in the $n = 2$ state can be resonantly scattered to the $n = 1$ state by emitting a LO phonon whose relaxation time is on the order of 0.1 ps [40] (Fig. 3.6(b)). On the other hand, the LO phonon scattering

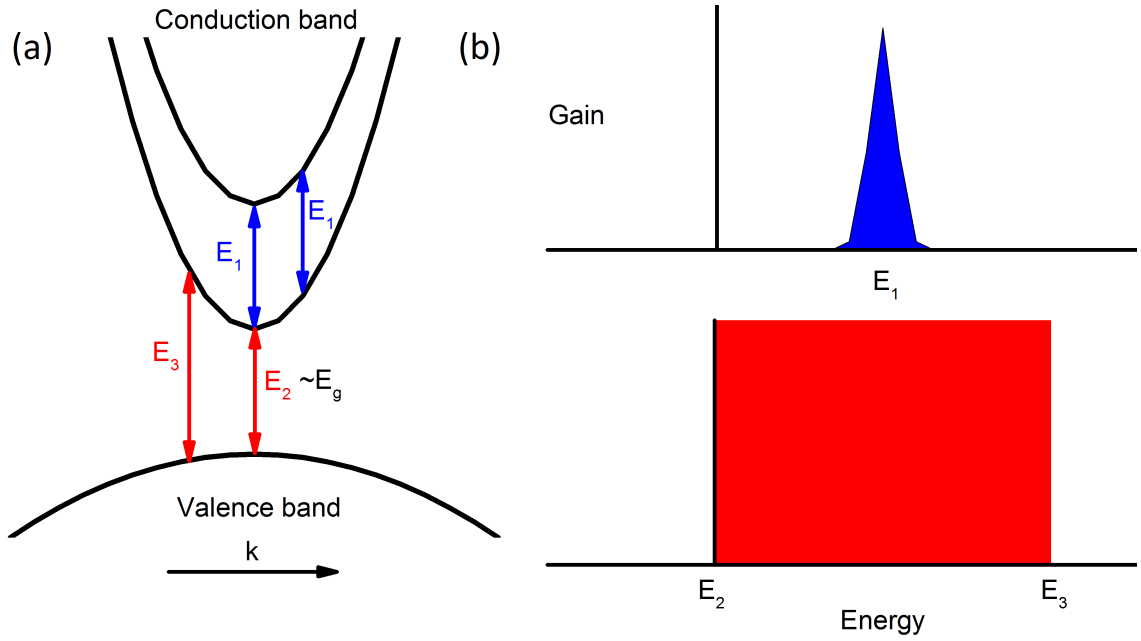

Figure 3.5: Transition processes and laser linewidth in QCL and semiconductor lasers. (a) interband transitions (red) in semiconductor laser and intersubband transitions in QCL. The output laser linewidth is much broader in the semiconductor laser (bottom) than the QCL (top) due to the opposite band curvature between VB and CB. Adapted from Ref. [39].

process is suppressed between the $n = 2$ and $n = 3$ states because of the mismatch between their energy gap and the LO phonon energy. Another possible route for electrons to leak out from the $n = 3$ state is the escaping to the continuum states outside of the DQWs. This leakage can be reduced by imposing a superlattice structure with an energy gap (minigap) facing the $n = 3$ state like a Bragg reflector. The minibands in the superlattice structure can also be aligned to the $n = 2$ and $n = 1$ states to further deplete the electrons. As a result, the relaxation time between the $n = 3$ and $n = 2$ states ($\tau_{32} \sim 2$ ps) is much larger than that between the $n = 2$ and $n = 1$ states ($\tau_{21} \sim 0.2$ ps) [40].

Compared to interband transitions where electrons are relaxed to the VB and stop contributing to lasing, the electrons in the intersubband transitions still remain as conduction electrons and thus still functional. Therefore, QCLs are designed with repeated units to improve the efficiency, giving rise to the term "cascade" in its name. Between the units, the active regions are bridged by the superlattice structure. By further aligning the minibands

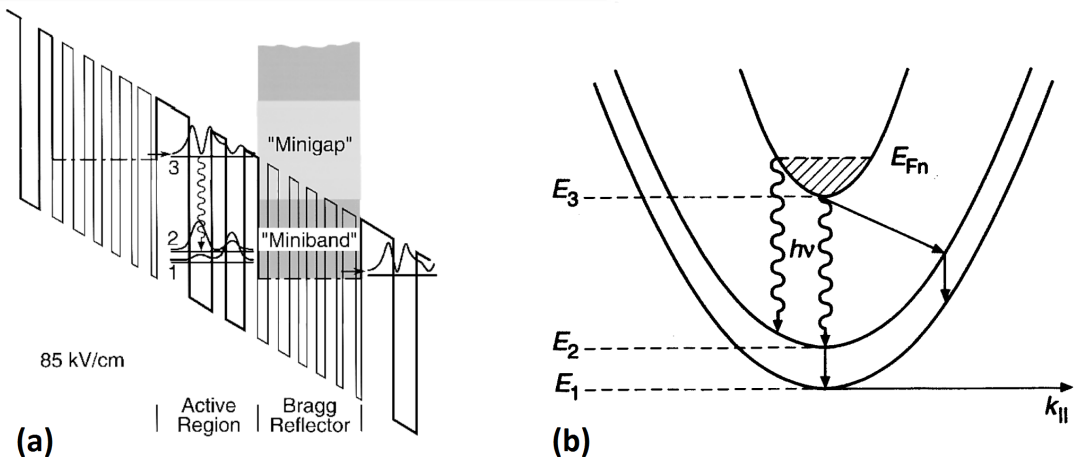

Figure 3.6: QCL design. (a) The band profile of a QCL under an external electric fields. The injected region (i.e. Bragg reflector) transports electrons from previous active region and injects into the $n = 3$ state in the next cycle. (b) Transition processes in the three level system of the active region. The electrons relax from the $n = 3$ state to the $n = 2$ state by emitting a photon followed by a fast LO phonon scattering into the $n = 1$ state. Adapted from Refs. [39, 41].

to the $n = 3$ state in the next stage, the superlattice structure can efficiently transport the electrons from the previous unit to the next region for lasing. Therefore, the superlattice structure is also named the injected region.

Compared to FTIR, QCL has a much higher power output. An aperture of several hundred microns would almost kill all the signals for a broadband light source in FTIR. But for QCL, there is still considerable amount of signal for a 5 μm hole. This is a great advantage in studying microsize samples. Another advantage is the highly collimated and linearly polarized beam as expected from lasers. This is important when coupled to other optical elements for more advanced measurements such as circular polarization resolved measurement.

3.3 Magneto-infrared setup

Next, we will briefly describe our magneto-IR setup using FTIR and QCL. All our magneto-IR measurements were performed in the National High Magnetic Field Laboratory (NHMFL) in Tallahassee, Florida. Figure 3.7 shows the experiment setup using FTIR. Specifically,

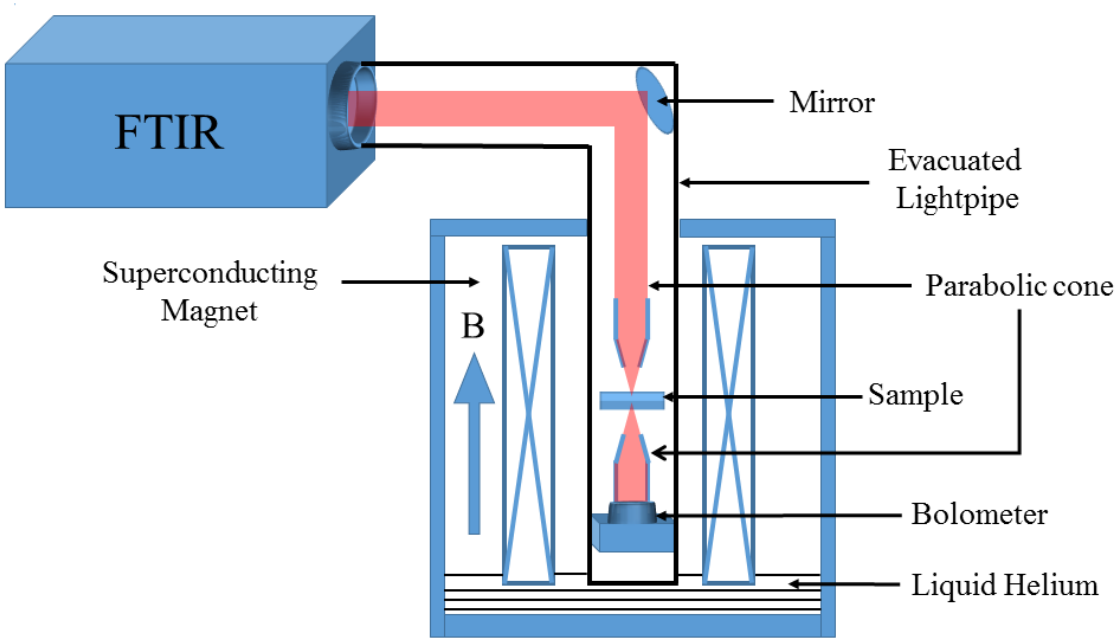

Figure 3.7: FTIR-based magneto-IR setup. Schematic drawing of the magneto-IR experiment setup using FTIR.

the IR light from a spectrometer is delivered to a superconducting magnet through an evacuated light pipe to reduce environmental disturbances such as moisture and temperature variation. It follows by a homemade parabolic cone to focus lights onto a sample to maximize the signal. The transmitted lights are collected by another parabolic cone and received by a silicon composite bolometer. This extra component below the sample is mainly to keep the bolometer away from the field center to reduce the magneto-resistance of the bolometer. The signal from the bolometer is amplified by an analog voltage amplifier and fed back into the FTIR spectrometer for data analysis. The system is operating at liquid helium temperature and the maximum magnetic field is 17.5 T.

The magneto-IR setup using QCL is similar to the one with FTIR except that the laser light is modulated by a chopper and the signals from the bolometer are fed into a lock-in amplifier. In this way, the noise coming from other frequency domains will be greatly suppressed, thus increasing the signal-to-noise ratio of the measurements.

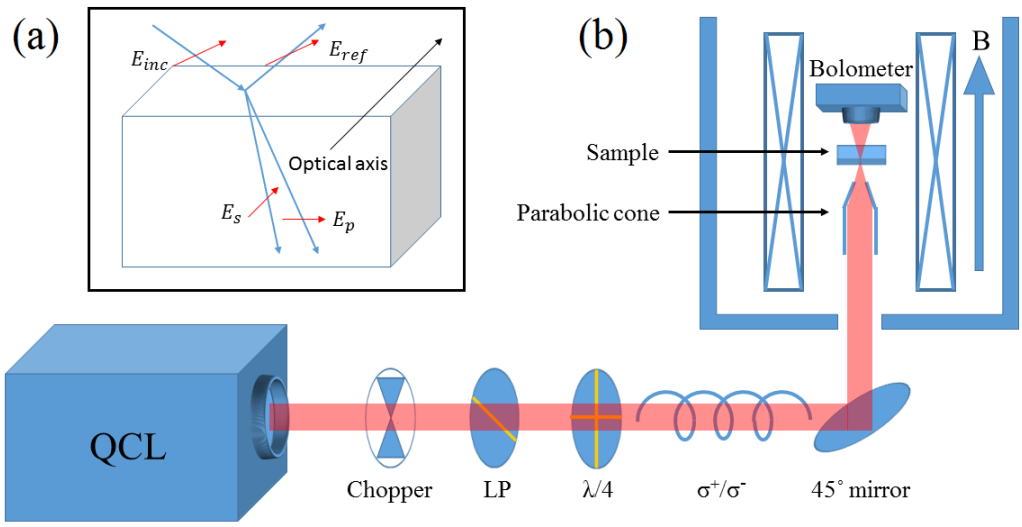

Figure 3.8: Circular polarization resolved measurement setup. (a) Operation principle of a waveplate. The difference in s and p polarized refractions is due to different refraction indicies in the waveplate. (b) Schematic drawing of the magneto-IR experiment setup coupled to QCL. A linearly polarized light can be easily achived by removing the quarter waveplate.

Compared to the FTIR setup, the QCL has a much higher power intensity and a highly collimated beam, which makes it easierto align and control. Therefore, we have also developed a circular polarization resolved measurement setup based on QCL. To produce circular polarized light, a quarter waveplate is needed. It is made of a bifringing material that has different refraction indices for s and p polarized lights. In consequence, the two polarized lights travel at different speed and paths, producing a phase shift when they recombine on the other side of the waveplate (Fig. 3.8(a)). By choosing suitable materials and a proper thickness for the plate, arbitrary phase shift between the s and p polarized lights can be engineered. Particularly, if the phase shift is 90 degree, then the recombined light is circularly polarized. Such waveplate is called quarter waveplate. However, the refraction index of a given material strongly depends on the incident light wavelength. Therefore, waveplates made of single material are applicable to light of a single or a very narrow range of wavelength. It is impractical both experimentally and financially to cover a broad range of wavelength by simply having many single wavelength waveplates. An achromatic waveplate is highly desirable in this case, which can be achieved in two ways. First, one can stack multiple layers of bifringing materials of different thicknesses to compensate the phase shifts of different wavelengths for a relatively broadband waveplate if carefully designed [42]. Another method is based on the fact that the s and p polarizations experience different phase shifts in a total internal reflection [43], which weakly depends on the light wavelength [44]. However, waveplate of this kind is usually bulky and has a large beam offset at the output.

Figure 3.8(b) schematically shows the circular polarization resolved measurement setup. Laser light is first delivered through a linear polarizer (LP) which not only provides an additional degree of freedom for alignment but also can be used as an attenuator to prevent the bolometer from overloading with too much laser power. An achromatic quarter waveplate is placed behind the LP to generate a circular polarized light. The rest is the same as the unpolarized setup (Fig. 3.7). Note that the use of a mirror in the light path will flip the

circular polarization.

In order to resolve the polarization dependent effects, one can rotate the quarter wave-plate or the LP 90 degree to switch to another circular polarization. Equivalently, one can stay at the same configuration but sweep to the opposite magnetic field. Here, we choose the latter to minimize errors in optical alignments.

CHAPTER 4

QUANTUM PHASE TRANSITION IN InAs/GaSb DOUBLE QUANTUM WELLS

4.1 Introduction

When stitching two semiconductors, due to the mismatch between the CBs and VBs, there are three possible [45] band alignments (Fig. 4.1(a)). The broken-gap type is different from the other two types in that an empty CB lies below a filled VB. This allows electrons in the filled VB to transfer to the empty CB, resulting in the coexistence of spatially separated and long lifetime electrons and holes. This charge transfer effect is not expected in either straddle- or stager-type alignments because there is no available state in the lower VBs. InAs/GaSb DQWs have long been studied for its broken-gap band alignment (Fig. 4.1(b)) in which many intriguing physics ranging from excitonic resonances [46–48] to electron-hole hybridization [49–53] have been observed.

It is interesting that the broken-gap alignment in QWs can be manipulated using the quantum confinement effect. For InAs/GaSb DQWs, when the well width of InAs is small enough, the lowest electron level E_0 in InAs can be pushed above the highest hole level H_0 in GaSb, driving the system to the normal state ($E_0 > H_0$). If the opposite alignment $E_0 < H_0$ is achieved, the system is in the inverted state, i.e., broken-gap alignment. The transition from normal to inverted state occurs through a critical state at which $E_0 = H_0$ (Fig. 4.1(c)). It is also reported that such transition can be achieved continuously with the application of electrostatic fields in a dual gate configuration (Fig. 4.2(b)) [11, 54], thus providing versatile tunabilities in the electronic band structure.

Recently, the InAs/GaSb DQWs system has seen renewed interest in the context of TI research due to its inherently inverted band structure. Inspired by the theoretical prediction of a 2D TI phase [11], the QSH effect (Fig. 4.2(b)) [55–57] and helical Luttinger liquids

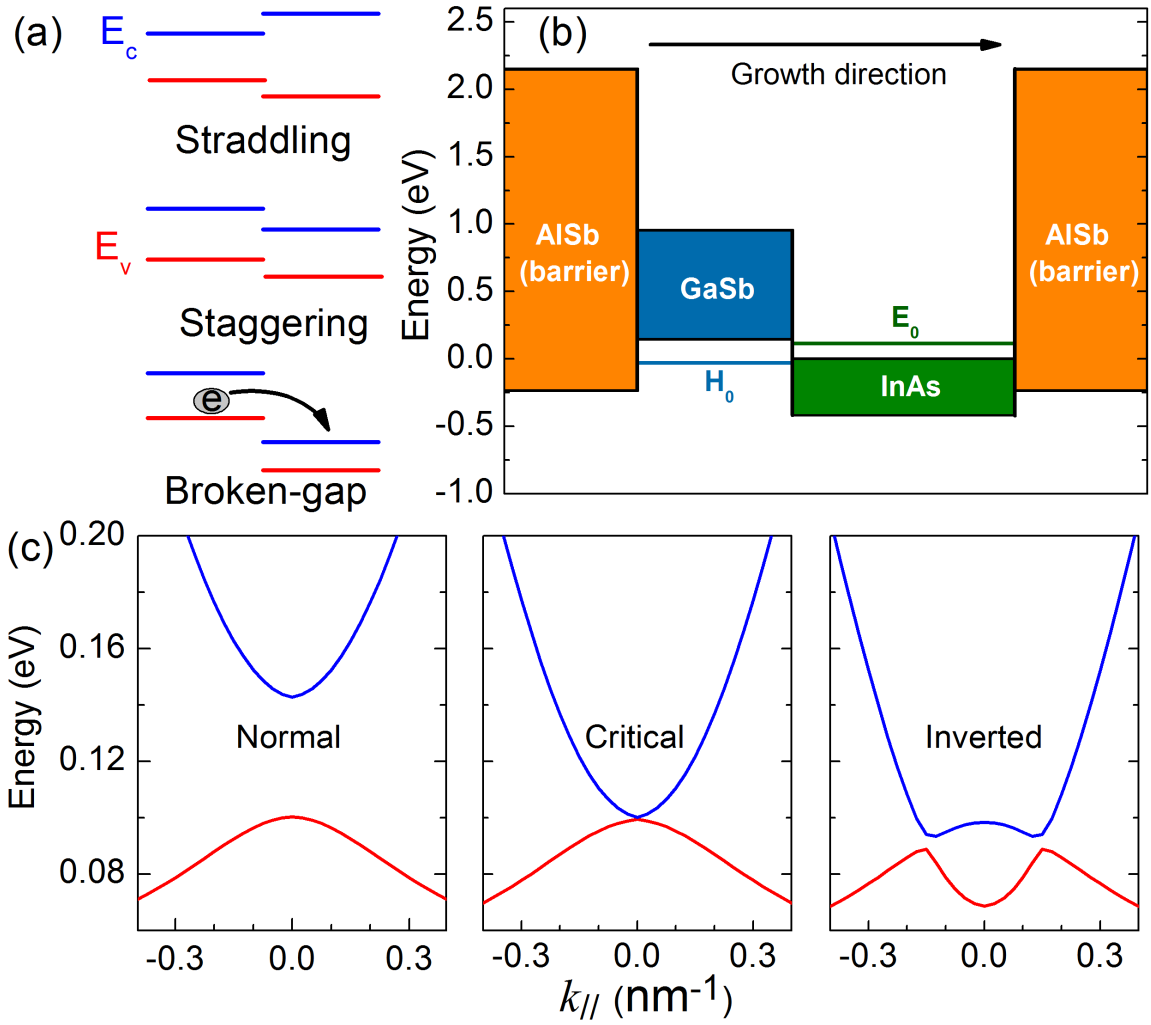

Figure 4.1: Band alignment in InAs/GaSb DQWs. (a) Three types of band alignments between two different semiconductors. (b) Schematic band diagram of AlSb/InAs/GaSb/AlSb QW structure. The energy zero is referenced to the conduction band edge of bulk InAs. The top and bottom of each color coded blocks indicate the energies of the conduction and valence band edges for each material. E_0 and H_0 illustrate the lowest electron subband in InAs and the highest hole subband in GaSb, respectively, due to quantum confinement. (c) Evolution of the band alignment in InAs/GaSb DQWs, as the width d of InAs QW increases (from left to right) while fixing the GaSb QW width. Blue and red curves represent the lowest electron and highest hole subbands, respectively.

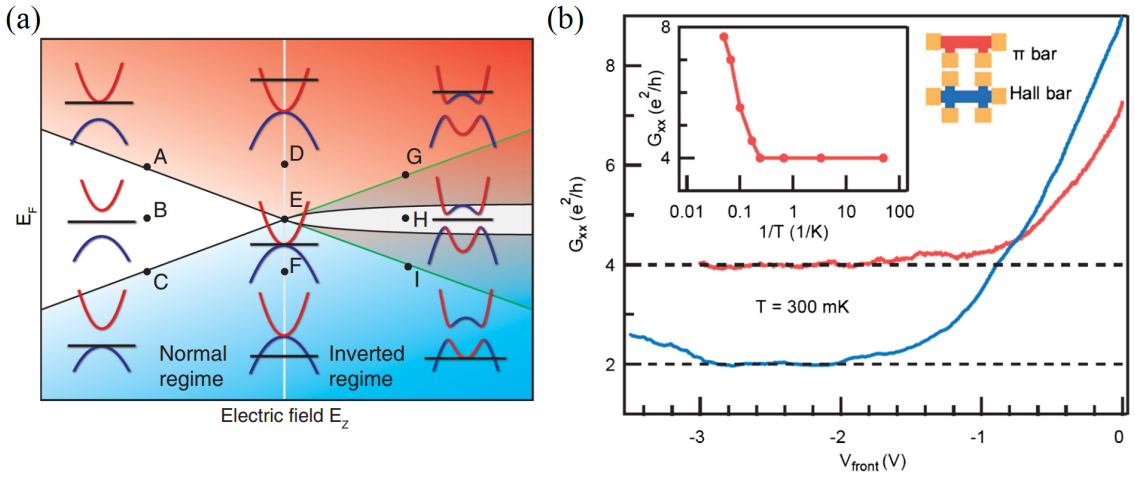

Figure 4.2: Electric field effect and QSH in InAs/GaSb DQWs. (a) Phase diagram as a function of electric field and Fermi level. The electric field manipulation is realized through a dual gating configuration using top and back gates. (b) Robust QSH effect for two device configurations over a wide range of gate voltages and temperatures (inset). Adapted from Refs. [54, 56].

[58] have been experimentally explored in the inverted regime, while an exotic exciton insulator state [59] and a giant supercurrent state [60] have been found in the vicinity of the critical state. Strain effects have also been found useful in tuning the electronic band structure of InAs/GaSb DQWs, leading to a robust QSH insulator state suited for realizing Majorana fermions [61]. Therefore, precise control of band alignment of InAs/GaSb DQWs from the normal to the inverted state is crucial for future fundamental studies.

From technological perspective, InAs/GaSb-based materials are promising candidates for third-generation IR detectors [62], high-power light emitting diodes [63], and tunnel field-effect transistors [64], owing to their band engineering flexibility and the resulting low Auger recombination rates [65]. Practical applications of the material require a complete understanding of the electronic band structure, with respect to external parameters such as strain and doping.

We note that previous combined experimental and theoretical studies [49–51, 53] of InAs/GaSb DQWs largely focused on the heavily inverted regime using reduced models. Quantitative investigations of the quantum transition from the normal to the inverted state

have not yet been performed. In this chapter, we study the evolution of the electronic band structure of InAs/GaSb DQWs across the normal to the inverted state transition with different InAs QW widths using magneto-IR spectroscopy. The observed magneto-optical modes can be explained using an eight-band $\mathbf{k} \cdot \mathbf{p}$ model, and semi-quantitative agreement is achieved [66]. We show that in addition to the commonly used electrostatic gate, the transition can be manipulated in a much larger parameter space via tuning the relative thickness of the QWs, the strain, and the magnetic field.

4.2 $\mathbf{k} \cdot \mathbf{p}$ theory in quantum well systems

The PB model based on the eight-band $\mathbf{k} \cdot \mathbf{p}$ method [27, 72, 73, 75–77] has been successfully used for achieving semi-quantitative understanding of the electronic and magneto-optical properties of narrow-gap semiconductors [29, 32, 69, 78]. However, the model in Chapter 2 is derived for bulk materials. Several modifications will be discussed in this section when applying to QWs.

4.2.1 Envelope theory

First, we briefly introduce the Burt-Foreman envelope theory [24, 67] for accomodating the material difference across the QW. We assume that the wavefunction across the QWs along the growth direction z is

$$\Phi(z) = \sum_n F_n(z) U_n(z), \tag{4.1}$$

where $U_n(z)$ is a complete set of orthogonal periodic functions throughout the whole structure and $F_n(z)$ is the envelope function. Substituting (4.1) into the Schrödinger equation and using the complete and orthogonal property of $U_n(z)$, Burt has derived an exact equation for the envelope function $F_n(z)$ [67]. Compared to the bulk case, the new addition is a non-local term resulting from the potential change at the QW interface.

Two assumptions are made to connect to the $\mathbf{k} \cdot \mathbf{p}$ Hamiltonian derived earlier. First, the $U_n(z)$ is taken to be the eigenfunctions of the constituent material at the Brillouin zone center. Its extension throughout the whole structure is valid if the chemical compositions vary slowly in all other constituent materials, which implies that the envelope functions also vary slowly across the structure. Second, the interface is assumed to be atomically sharp, which is in fact a realistic approximation thanks to the state-of-the-art MBE growth technique. In mathematics, the abrupt changes of material parameters across interfaces can be described by a piecewise function. Under these two assumptions, the non-local term has a small contribution and is confined to a region of a few Å s close to the interface, thus can be discarded [67]. Since $U_n(z)$ is chosen as the basis functions in one of the constituent materials, it is not surprising to find that the Schrödinger equation can be transformed into the $\mathbf{k}\cdot\mathbf{p}$ form. Specifically, only the slowly varying F_n and abrupt interface assumptions are needed to omit the non-local term since the theory is applicable to any U_n that are complete and orthogonal periodic functions. The choice of $U_n(z)$ in the first assumption allows for connection to the $\mathbf{k} \cdot \mathbf{p}$ formalism. Otherwise, the Schrödinger equation would end up in a different representation. Meanwhile, in the growth direction of QWs, the momentum k needs to be replaced by momentum operators due to the quantum confinement effect. Caution should also be applied to the ordering of the operators with respect to material parameters. In our [001] QW, only k_z needs to be replaced by $-i\frac{\partial}{\partial_z}$ while k_x and k_y are still good quantum numbers in the other two directions.

Equation (2.2.1) is now a set of coupled differential equations. One can use the plane-wave expansion method as detailed in Appendix B to transform coupled differential equations into an algebra eigen-value problem. The periodic boundary conditions in the plane-wave expansion imply the repetition of the studied QW structure, which may be a problem in the non-periodic direction such as the growth direction. To get around this problem, thick enough barriers such as AlSb QWs are imposed at both sides of the InAs/GaSb DQWs so that the wavefunctions do not leak out to the adjacent repeating structures. In this way, the

InAs/GaSb QWs can be treated as an isolated system without coupling to other constituents. In addition, unlike the particle-in-a-box model that requires wavefunction matching at the interfaces, the Burt-Foreman envelope theory only asks the envelope function $F_n(z)$ and its first derivative continuous, due to the fact that $U_n(z)$ are the same basis functions through out the entire structure. This requirement is automatically satisfied in the plane-wave expansion since all the basis functions are continuous.

4.2.2 Strain effect

A QW structure is normally composed of several different materials between which the lattice mismatch gives rise to the strain effect. The band profile can be modified up to tens of meVs even if the lattice mismatch is only 1%. Thus, it is important to consider strain effect in band structure calculations.

Bir and Pikus [68] suggest that if one can distort the coordinate system in the same way as the lattice mismatch distortion, then the material can be restored to its "natural lattice" structure under the description of the new coordinate system. In linear approximation, the transformation of the coordinate system is

$$x_i' = x_i + \sum_j \epsilon_{ij} x_j, \quad i, j = x, y, z. \tag{4.2}$$

Here, the prime denotes the new coordinate system in which the material restored its "natural lattice" structure, the unprime ones are in the old coordinate system, and ϵ is the strain tensor. The strained Hamiltonian in the old coordinate system can be related straightforwardly to the unstrained Hamiltonian in the new coordinate system using Eq. (4.2), leading to [69]

$$H_s = \begin{pmatrix} A_\epsilon & 0 & 0 & 0 & 0 & 0 & 0 & 0 \\ 0 & A_\epsilon & 0 & 0 & 0 & 0 & 0 & 0 \\ 0 & 0 & -P_\epsilon - Q_\epsilon & -L_\epsilon & -M_\epsilon & 0 & -i\frac{1}{\sqrt{2}}L_\epsilon & i\sqrt{2}M_\epsilon \\ 0 & 0 & -L_\epsilon^* & -P_\epsilon + Q_\epsilon & 0 & -M_\epsilon & i\sqrt{2}Q_\epsilon & -i\sqrt{\frac{3}{2}}L_\epsilon \\ 0 & 0 & -M_\epsilon^* & 0 & -P_\epsilon + Q_\epsilon & L_\epsilon & i\sqrt{\frac{3}{2}}L_\epsilon^* & i\sqrt{2}Q_\epsilon \\ 0 & 0 & 0 & -M_\epsilon^* & L_\epsilon^* & -P_\epsilon - Q_\epsilon & i\sqrt{2}M_\epsilon & i\frac{1}{\sqrt{2}}L_\epsilon^* \\ 0 & 0 & i\frac{1}{\sqrt{2}}L_\epsilon^* & -i\sqrt{2}Q_\epsilon & -i\sqrt{\frac{3}{2}}L_\epsilon & -i\sqrt{2}M_\epsilon & -P_\epsilon & 0 \\ 0 & 0 & -i\sqrt{2}M_\epsilon^* & i\sqrt{\frac{3}{2}}L_\epsilon^* & -i\sqrt{2}Q_\epsilon & -i\frac{1}{\sqrt{2}}L_\epsilon & 0 & -P_\epsilon \end{pmatrix},$$

where $A_\epsilon = a_c(\epsilon_{xx} + \epsilon_{yy} + \epsilon_{zz})$, $P_\epsilon = -a_v(\epsilon_{xx} + \epsilon_{yy} + \epsilon_{zz})$, $L_\epsilon = id(\epsilon_{xz} - i\epsilon_{yz})$,

$$Q_\epsilon = -\frac{b}{2}(\epsilon_{xx} + \epsilon_{yy} - 2\epsilon_{zz}), \quad M_\epsilon = -\frac{\sqrt{3}}{2}b(\epsilon_{xx} - \epsilon_{yy}) + i\frac{2\sqrt{3}}{3}d\epsilon_{xy},$$

while a_c, a_v, b, and d are deformation potentials. To simplify the problem, we restrict ourselves to the pseudomorphic case where the epitaxial layers of the QWs are all pinned to the same lattice constants. In this case, the strain tensor has the following relations

$$\epsilon_{xx} = \epsilon_{yy} = \frac{a_0 - a}{a}, \quad \epsilon_{zz} = -\frac{2C_{12}}{C_{11}}\epsilon_{xx}, \quad \epsilon_{ij} = 0, \quad \text{for} \quad i \neq j.$$

Here, a_0 and a are the pinned and original lattice constants, respectively, and C_{11} and C_{12} are both the stiffness constants. For strained QWs pseudomorphically grown on a (001) substrate, the pinned constant is set to be the the substrate lattice constant.

At Γ point, the eight-band Hamiltonian including strain can be reduced to four bands

due to the spin degeneracy [70]

$$H(\mathbf{k}=\mathbf{0}) = \begin{pmatrix} E_c + A_\epsilon & 0 & 0 & 0 \\ 0 & -P_\epsilon - Q_\epsilon & 0 & 0 \\ 0 & 0 & -P_\epsilon + Q_\epsilon & -\sqrt{2}Q_\epsilon \\ 0 & 0 & -\sqrt{2}Q_\epsilon & -P_\epsilon - \Delta \end{pmatrix}.$$

In addition, since only the SO and LH bands are coupled, one can obtain

$$\begin{aligned} E_c(0) = E_c + A_\epsilon, \quad E_{HH}(0) = -P_\epsilon - Q_\epsilon, \\ E_{LH}(0) = -P_\epsilon + \frac{1}{2}(Q_\epsilon - \Delta + \sqrt{\Delta^2 + 2\Delta Q_\epsilon + 9Q_\epsilon^2}), \\ E_{SO}(0) = -P_\epsilon + \frac{1}{2}(Q_\epsilon - \Delta - \sqrt{\Delta^2 + 2\Delta Q_\epsilon + 9Q_\epsilon^2}). \end{aligned}$$

If the energy shift induced by strain is small compared to the SO energy ($Q_\epsilon \ll \Delta$), then the LH and SO band energies can be approximated by

$$E_{LH}(0) = -P_\epsilon + Q_\epsilon, \quad E_{SO}(0) = -P_\epsilon - \Delta.$$

In general, the CB is offset by A_ϵ and the VBs (HH, LH and SO) are offset by P_ϵ. The degenracies within the VBs are further lifted by Q_ϵ and Δ.

We assume that the InAs/GaSb system is under pseudomorphic strain and all the QW in-plane lattice constants are pinned to the in-plane lattice constant of the GaSb substrate. The strain gives rise to an energy shift of a few tens of meV and drives the system towards a more inverted band alignment. This effect is significant for all the DQW samples studied.

4.2.3 Charge transfer effect

In a broken-gap band structure, charge transfer results in a significant internal electrostatic potential V across the QWs and greatly modifies the band structure. The charge transfer

effect can be modeled through a self-consistent approach. First, we start with an existing internal potential V_{old} ($V_{old} = 0$ as an initial guess) and solve the $\mathbf{k}\cdot\mathbf{p}$ Hamiltonian according to,

$$\big[H - eV(z)\mathbb{I}\big]\Phi = E\Phi,$$

where $\mathbb{I}$ is an identity matrix of the same dimension as H. From the resulting wavefunction, an updated potential V_{new} can be calculated. If the two potential profiles, V_{old} and V_{new}, converge, the calculation will stop. Otherwise, a new iteration will be performed by modifying the potential to

$$V_{iterate} = V_{new} + \alpha(V_{new} - V_{old}),$$

where $V_{iterate}$ will serve as a V_{old} for next iteration and α is a control parameter taken to be 0.1 to avoid divergence [71].

The potential profile calculation from the wavefunction requires some extra attentions. Due to the charge transfer effect in the inverted DQWs, there will be charge deficits in one well and surpluses in another compared to the same structure but under a normal state as a reference (Fig. 4.3). The reference state can be simply created just by changing the band-gap parameter. In this way, the net transferred charge distribution can be quantitatively calculated by substracting the total charge distributions of the reference structure from the inverted DQWs. The total charge distribution ρ_{total} along the growth direction is just the sum of all the VBs contributions

$$\rho_{total}(z) = -\frac{e}{(2\pi)^2}\sum_{n=\text{all VBs}}\int\sum_{m=1\ldots8}|a_n^m(z)|^2 f_F(E_n(k_x,k_y)-E_F)d\mathbf{k}_{\|},$$

where $a_n^m(z)$ is the wavefunction along z direction in the mth spinnor component of the nth band. The above calculation can be further simplified, as the charge transfer only affects the hybridized CBs and VBs. Therefore, we can just summer over the inverted VBs rather

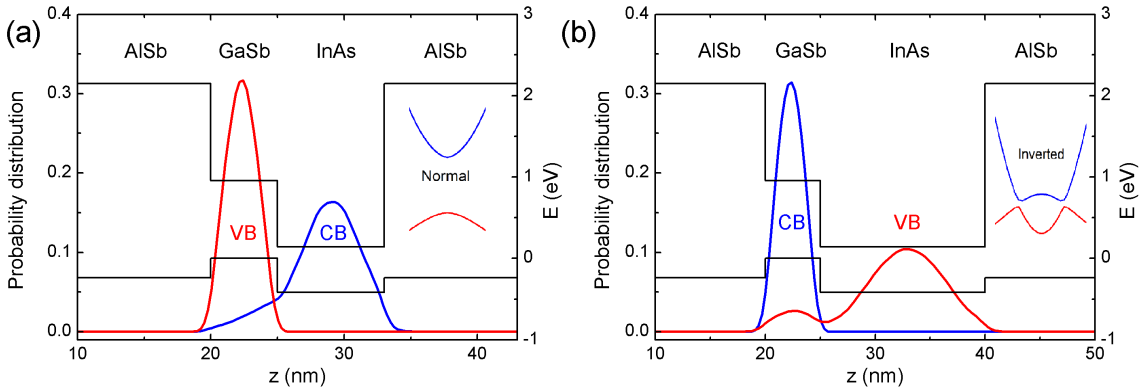

Figure 4.3: Charge distribution of CB and VB in InAs/gaSb DQWs. The band profile (black) and the probability density distribution of the lowest CB (blue) and the highest VB (red) at $k = 0$ in the (a) normal and (b) inverted states. Inset schematically shows the corresponding band dispersion. The thickness of each QW layer is $L_{AlSb} = 20$ nm (left buffer layer), $L_{GaSb} = 5$ nm, $L_{InAs} = 15$ nm for inverted and 8 nm for normal states, and $L_{AlSb} = 1000$ nm (right buffer layer).

than all the VBs If we are in the lightly inverted region where only one CB and one VB are involved, we can even drop the calculation of the reference structure. In this case, the transfered electrons in InAs QW are from the electron component wavefunction in the VB and the holes in GaSb QW can be calculated by the valence component wavefunction in the CB (Fig. 4.3(b)),

$$\rho_e(z) = -\frac{e}{(2\pi)^2} \sum_{n=VB} \int \sum_{m=1,2} |a_n^m(z)|^2 f_F(E(k_x,k_y) - E_F) d\mathbf{k}_{\|},$$
$$\rho_h(z) = \frac{e}{(2\pi)^2} \sum_{n=CB} \int \sum_{m=3...8} |a_n^m(z)|^2 (1 - f_F(E(k_x,k_y) - E_F)) d\mathbf{k}_{\|}.$$

In addition, the total charge of holes from the CB must be normalized to that of the electrons from the VB to maintain the charge neutrality condition. The normalization has to be referenced to the electrons from the VB because there is no real charge occupying the CB (in the intrinsic case). If there is any doping, the above calculation can be simply modified by adding/removing the wavefunction contributions from the states occupied/emptied by the doped electrons. The potential profile $V(z)$ can then be calculated by the Poisson

equation

$$-\frac{\partial^2 V(z)}{\partial^2 z} = -\frac{\rho_e(z) + \rho_h(z)}{\tilde{\epsilon}\tilde{\epsilon_0}},$$

where $\tilde{\epsilon}$ is the dielectric constant and $\tilde{\epsilon_0}$ is the vacuum permittivity. Instead of solving the Poisson equation, we split the QWs into many uniformly charged plates which are infinite in the $x-y$ plane and carry a sheet charge density of $\rho(z_0)dz_0$ at position z_0. The electric field is obtained by

$$E(z) = \int_0^L sgn(z - z_0)\frac{\rho(z_0)}{2\tilde{\epsilon_0}\tilde{\epsilon}(z)}dz_0.$$

The potential can be calculated by integrating again the electric field

$$V(z) = -\int_0^z E(z')dz'.$$

In addition, following Ref. [72], we further assume that the self-consistent potential profile calculated at zero magnetic field is B-field independent. In this way, we can extend the eight-band model to include the magnetic field effect.

Finally, we want to note that the charge transfer effect is appreciable only in the inverted state [79] when the VB of GaSb overlaps with the CB of InAs. This overlap leads to charge redistribution across the InAs/GaSb interface, which consequently modifies the potential profile in DQWs. The charge transfer effect counters, or even overpowers, the strain effect in heavily inverted InAs/GaSb DQW samples.

4.2.4 Modeling transitions

With the previous discussion, the total effective mass Hamiltonian of InAs/GaSb DQWs can be written as

$$H = H_L + H_Z + H_S + H_C, \tag{4.3}$$

where H_L, H_Z, H_S, and H_C are the Landau, Zeeman, strain, and confinement Hamiltonian, respectively. Following the PB formalism described in Section 2.2.2, one can obtained the

Table 4.1: Band parameters used in our eight-band $\mathbf{k}\cdot\mathbf{p}$ calculation. Unless stated explicitly, the parameters are taken from Ref. [80].

	InAs	GaSb	AlSb
m_e^* (m)	0.024	0.039	0.14
E_g (eV)	0.417	0.812	2.386
E_v (eV)	-0.417	0.143	-0.237
E_p (eV)	21.5	27	18.7
Δ (eV)	0.39	0.76	0.676
A_c (eV nm^2)	-0.0601	-0.0853	-0.0045
γ_1	2.81	2.32	2.57
γ_2	-0.093	-0.842	-0.116
γ_3	0.607	0.458	0.664
κ	-1.060	-1.542	-0.936
a (Å)	6.050	6.082	6.128
C_{12} (GPa)	452.6	402.6	434.1
C_{11} (GPa)	832.9	884.2	876.9
a_c (eV)	-5.08	-7.5	-4.5
a_v (eV)	-1	-0.8	-1.4
b (eV)	-1.8	-2.0	-1.35
d (eV)	-3.6	-4.7	-4.3

LL energy $E_{p,\nu}$ in the axial approximation for a given magnetic field, where the integer p is the PB manifold index and $p \geq -1$, and the integer ν labels the eigenvectors/eigenenergies belonging to the same index p. Next, the calculation can be repeated for different magnetic field to obtain the LL dispersions. Table 4.1 summarizes all the parameters used in the calculations.

In order to calculate the magneto absorption spectra (see Section 2.2.3), we first need to determine E_F. Second, we compute the magneto-absorption coefficient using the wave-functions obtained from the PB model and Fermi's golden rule. The deduced selection rule reads $\Delta p = \pm 1$, where $+$ $(-)$ denotes electron (hole) like transitions. In Fig. 4.4, we show calculated magneto-absorption spectra for DQW samples with $d = 8, 11, 13$ nm (detail sample information can be found in Section 4.3.1).

Better understanding of the data can be further attained using the manifold-resolved magneto-absorption spectra, some examples of which are shown in Fig. 4.5. Manifold-

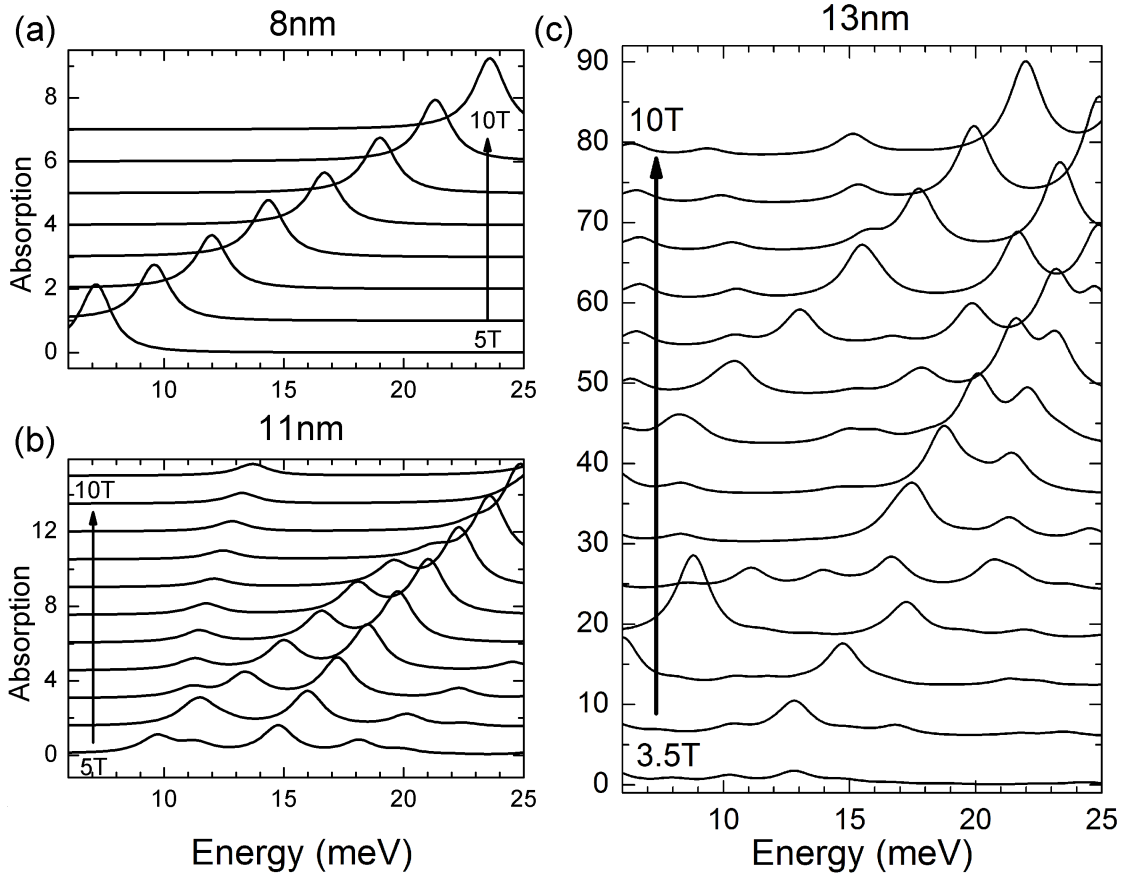

Figure 4.4: Calculated magneto-absorption spectra for the $d = 8$, 11 and 13 nm InAs/GaSb DQW samples.

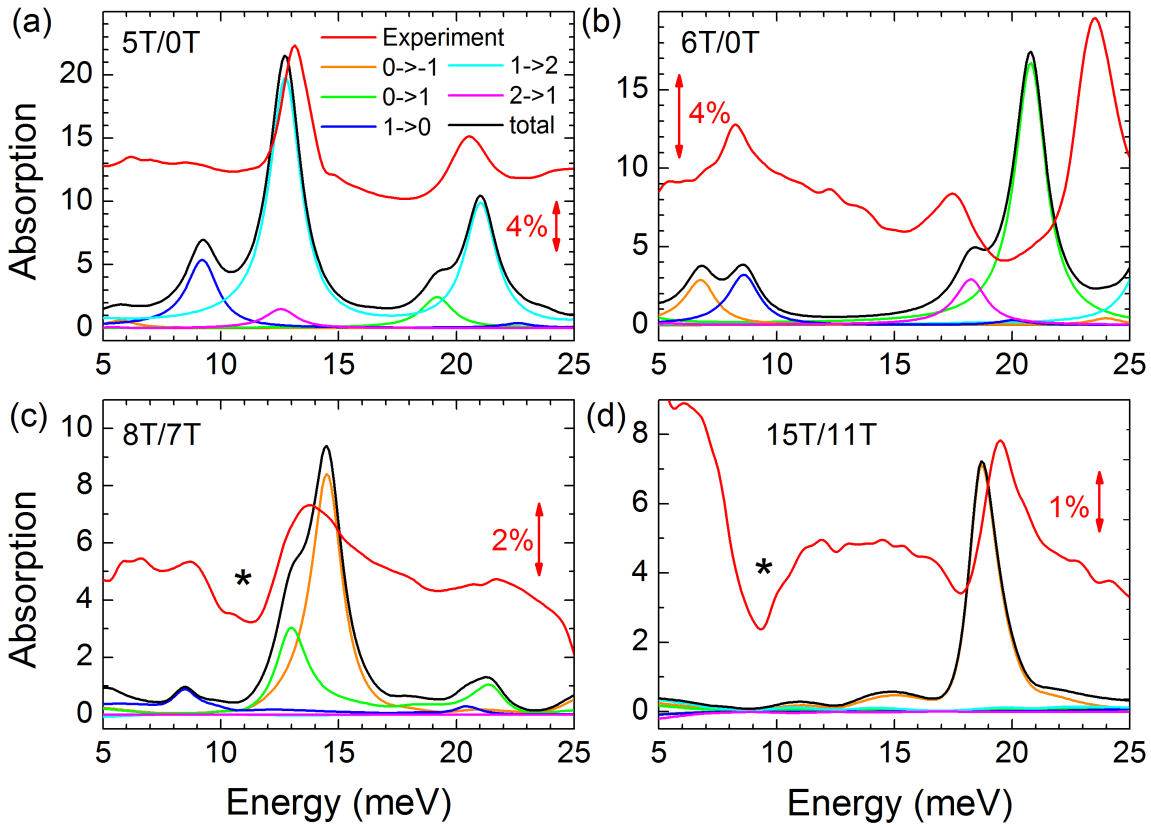

Figure 4.5: Calculated manifold-resolved magneto-absorption spectra for the $d = 15$ nm InAs/Gasb DQW sample. The manifold-resolved absorptions (in colors) and the total absorption (black) at (a) $B = 5$ T, (b) 6 T, (c) 8 T, and (d) 15 T. The calculations are compared with the major absorption peaks observed in the experiment (red), following the normalization method used in Fig. 4.8. The star symbols point to B-independent spectral features (dips) resulting from the normalization process.

resolved calculations help assign a specific transition to each absorption peak observed in our experiment.

4.3 Experiment and discussion

4.3.1 Experiment

The InAs/GaSb DQW samples studied in this work were grown by MBE on GaSb (001) substrates. A schematic of the epi-structure is shown in Fig. 4.6(a), where the InAs/GaSb DQW structure is sandwiched between two AlSb barrier layers. To study the normal to inverted transition, we fabricated a series of five InAs/GaSb DQW samples. We fixed the width of the GaSb QW at 5 nm, while varying the InAs QW width from $d = 8$ to $d = 10$, 11, 13, and 15 nm. Based on our self-consistent eight-band $\mathbf{k} \cdot \mathbf{p}$ calculation, the $d = 8$ nm sample is in the normal state, the $d = 10$ nm sample is close to the critical state, and the $d = 11$, 13, and 15 nm samples are in the inverted state (Fig. 4.6(b)). Magneto-transport measurements determined the carrier densities to be as low as $n \sim 1 \times 10^{11}$ cm^{-2} [60], several times lower than that reported in previous studies [46–49, 51, 53]. Therefore, our samples are close to the intrinsic limit, particularly suited for magneto-optical spectroscopy studies.

Magneto-IR spectroscopy measurements were performed in the Faraday configuration (Fig. 3.7) as described in Chapter 3. Normalized magneto-absorption spectra were then obtained by taking the ratio of $-T(B)/T(B = 0)$, where $T(B)$ is the transmission spectrum measured at a constant magnetic field B. In this scenario, the intra-band (cyclotron resonance, CR) and inter-band LL transitions are expected to manifest themselves as a series of absorption peaks. In the modeling, we assumed an electron density of $n = 0.9 \times 10^{11}$ cm^{-2}. The full width at half maximum (FWHM) is taken to be 0.8 meV in our calculation, estimated from the experimental data.

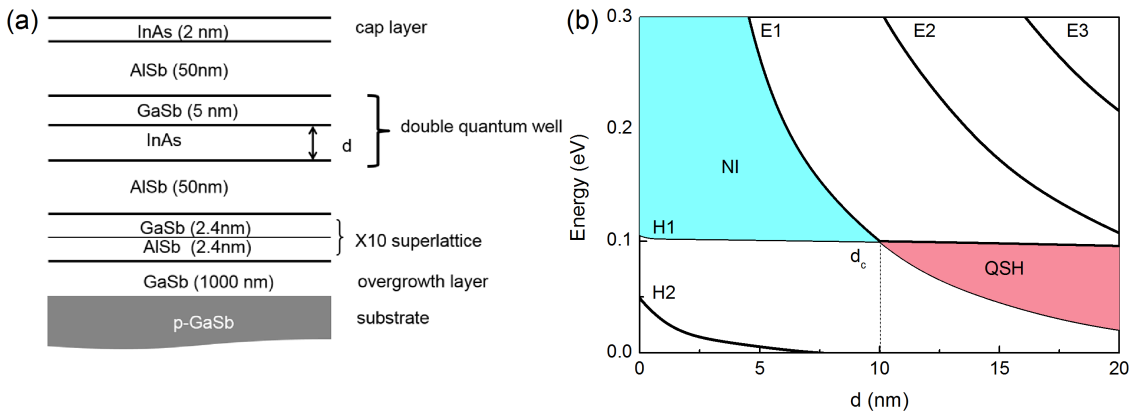

Figure 4.6: (a) Epi-structure of MBE grown InAs/GaSb DQW samples. (b) Evolution of the electron and hole subbands at Γ point as a function of the InAs thickness d, calculated using the 8-band $\mathbf{k}\cdot\mathbf{p}$ method. The critical thickness d_c, separating the normal and inverted band structures, is $\sim$ 10 nm.

4.3.2 Results and discussion

Figure 4.7(a) and 4.8(a) show normalized magneto-absorption spectra for the $d = 8$ and $d = 10$ nm DQW samples at selected magnetic fields, respectively. Here, the spectra exhibit a single symmetric line, indicative of a single absorption peak within the energy range of our measurements. The spectral lineshape becomes asymmetric and substantially broadened in the $d = 11$ nm sample, as shown in Fig. 4.7(b). As the InAs QW width increases further to $d = 13$ nm (Fig. 4.7(c)) and $d = 15$ nm (Fig. 4.8(b)), the InAs/GaSb DQWs enter a heavily inverted regime and multiple absorption peaks appear. Experimentally, one can identify four peaks for the case of $d = 15$ nm in Fig. 4.8(b) in the low-field region, $B \leq 5$ T. The two lower energy peaks are CR-like, $E_{CR} \propto B$, while the higher energy ones can be attributed to inter-band LL transitions. Interestingly, the CR-like peaks deviate from their linear-in-B dependence at higher magnetic field (better seen in Fig. 4.10(d)), suggestive of LL crossing/anti-crossing. This behavior is consistent with that theoretically predicted in Ref. [73]. In the middle and upper panels of Fig. 4.8(b), one can find another two absorption peaks with distinct B-dependence. In particular, the high-field peak exhibits very weak B-dependence, similar to that reported for InAs/GaSb superlattices in Ref. [49]. The

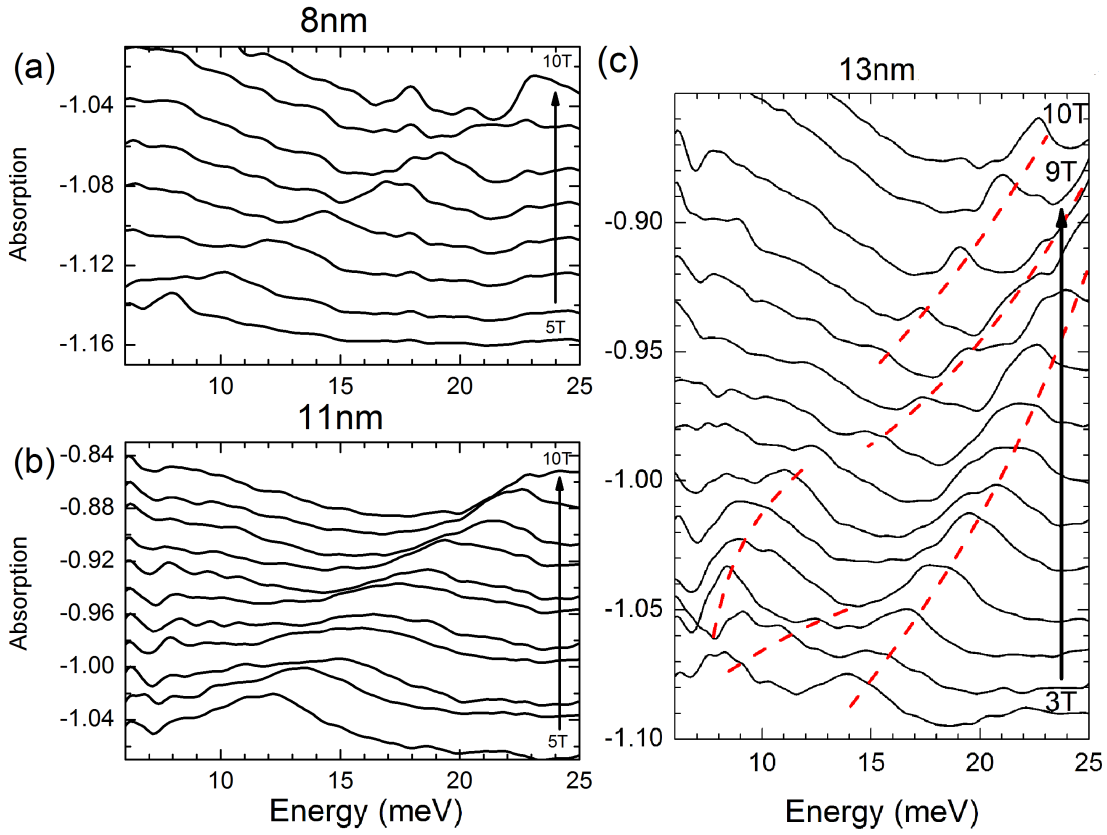

Figure 4.7: Normalized magneto-absorption spectra for $d = 8, 11$ and 13 nm InAs/GaSb DQW samples. The magneto-absorption spectra are plotted at selected magnetic fields for (a) $d = 10$, (b) 11, and (c) 13 nm, respectively. The asymmetric and broadened lineshape in (b) is due to the emergence of a second mode close by. The dashed lines in (c) indicate the major absorption peaks observed in the experiment. In all panels, the spectra are offset vertically for clarity.

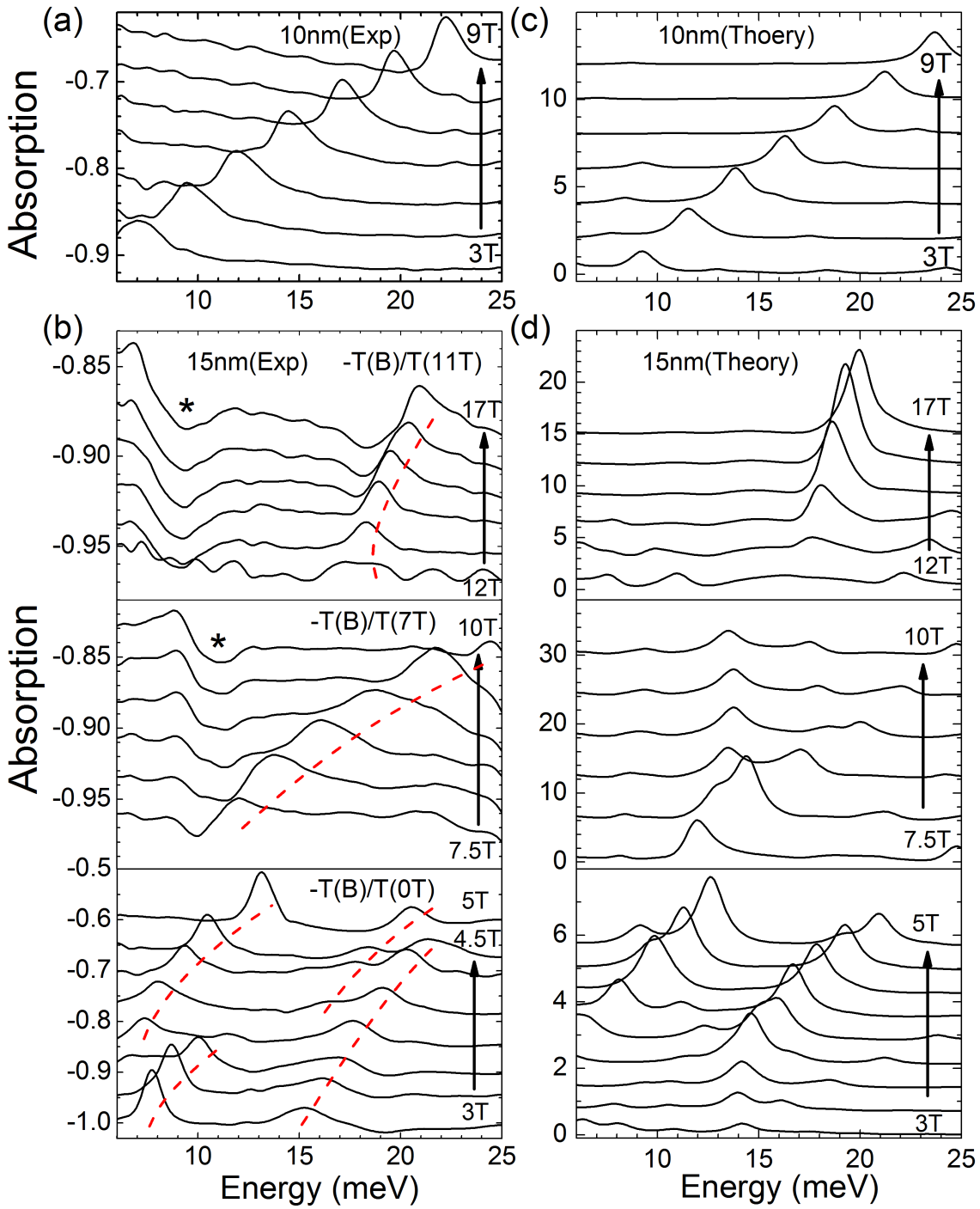

Figure 4.8: Normalized and calculated magneto-absorption spectra for $d = 10$ and 15 nm InAs/GaSb DQW samples. The spectra in the (a) $d = 10$ nm sample are normalized to 0 T while those in (b) $d = 15$ nm in the high-field (top panel), intermediate-field (middle panel), and low-field (bottom panel) regions are normalized to 11 T, 7 T, and 0 T, respectively, for best representation. The star symbols point to B-independent spectral features originating from the normalization process. The dashed lines indicate the major absorption peaks observed in the experiment. (c,d) Calculated magneto-absorption spectra in comparison with the experimental results in (a) and (b). In all panels, the spectra are offset vertically for clarity.

observation of a total of six absorption peaks in the $d = 15$ nm DQW sample (Fig. 4.10(d)) can be attributed to its low carrier density (approaching the intrinsic limit). However, the literature lacks a quantitative model that can interpret all these peaks.

To explain how band inversion changes the LL transitions in InAs/GaSb DQWs, we performed calculations with the eight-band PB model [74]. Figures 4.8(c,d) show the calculated magneto-absorption spectra for the slightly inverted ($d = 10$ nm) and heavily inverted ($d = 15$ nm) DQW samples, in comparison with the experimental data in Figs. 4.8(a,b). One can also compare Figs. 4.4 and 4.7. The same normalization method is applied to both the experimental and theoretical results. Here, as one can see, the calculated spectra capture all the absorption peaks observed in the experiment, although the relative strength between these peaks does not exhibit a perfect match.

The calculated energy levels and Fermi energy E_F are plotted as a function of magnetic field in Fig. 4.9 for the $d = 8$, 10 ,13 and 15 nm samples. (The result of $d = 11$ nm is very similar to that of $d = 10$ nm.) Here, the PB manifold is color coded based on the index p, and for simplicity we only show the lowest levels, i.e., when $p = -1, 0, 1$, and 2. As one can clearly see in Fig. 4.9, the band structure of InAs/GaSb DQWs exhibits a transition from the normal to the inverted state with increasing InAs QW width d. In the normal state (Fig. 4.9(a)), the electron (hole) levels reside in the conduction (valence) band and the energy of each level shows a monotonic B-dependence without any crossing. In contrast, when the band is inverted (Figs. 4.9(b-d)), hole-like levels may exist at the bottom of the CB while electron-like levels appear at the top of the VB. These levels inevitably cross or anti-cross each other at sufficiently high magnetic field, leading to multiple magneto-absorption peaks. The magnitude of the crossing/anti-crossing magnetic field therefore characterizes the degree of band inversion. One can see from Fig. 4.9 that the $d = 10$ nm DQW sample is only slightly inverted, whereas the $d = 13$ nm and 15 nm samples are heavily inverted. In addition, we note that even for a heavily inverted band structure, the electron-like levels in the valence band can be lifted above all the hole-like levels, at

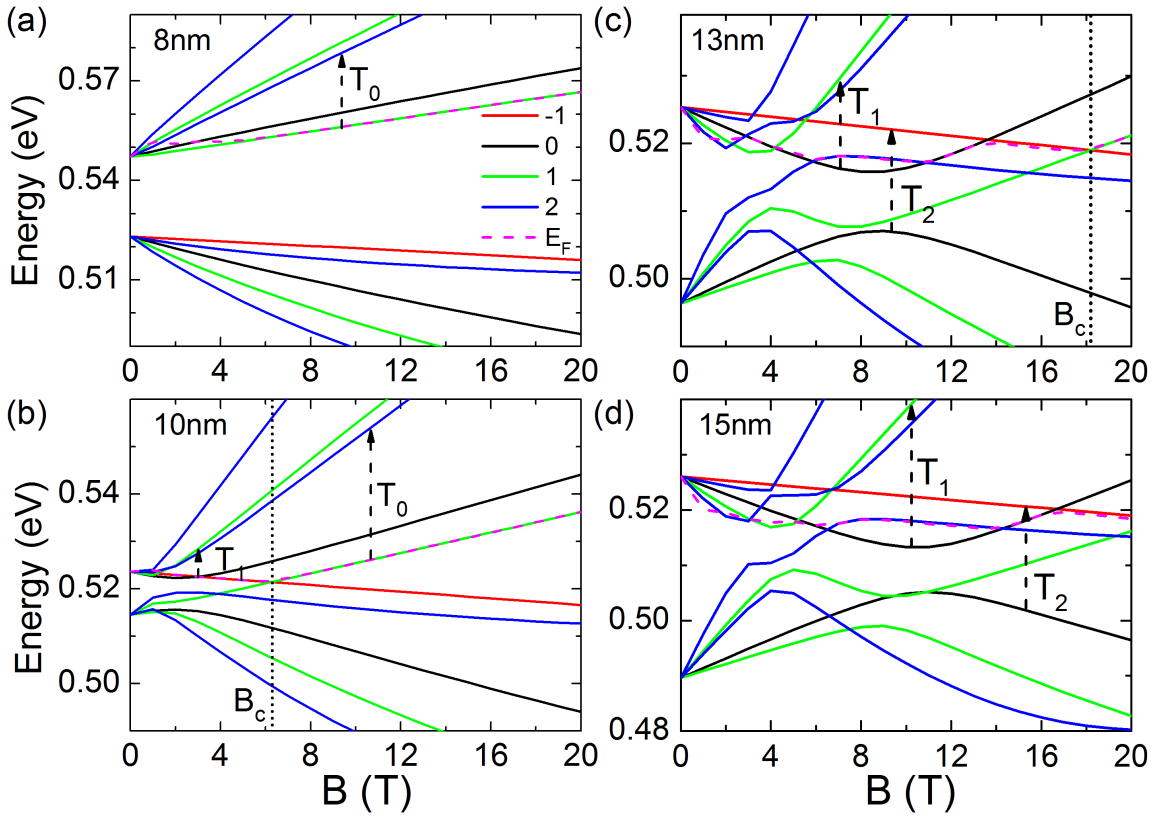

Figure 4.9: Fan diagram of InAs/GaSb DQWs from the normal to the inverted state. Calculated energy levels are plotted as a function of magnetic field for the (a) $d = 8$ nm, (b) 10 nm, (c) 13 nm, and (d) 15 nm InAs/GaSb DQW samples. The PB manifold is color coded based on the index p, and the dashed line shows the evolution of E_F as a function of magnetic field. The dashed arrows indicate the major transitions, T_0, T_1, and T_2, commonly observed in our samples. The dotted lines mark the onset (B_c) of the magnetic field driven transition from the inverted to the normal state.

sufficiently high magnetic fields, driving the system to the normal state [46, 47, 81, 82]. We will return to this magnetic field driven semimetal to semiconductor transition later in the context of Fig. 4.11.

It is important to note that our eight-band PB calculation is based on the band parameters reported in Ref. [80] with only two adjustable variables. One is the carrier density (or Fermi energy), which is set to be $n = 0.9 \times 10^{11}$ cm^{-2} for all the samples. As our DQWs are close to the intrinsic limit, the Fermi energy is expected to be quickly pinned to the lowest electron level with increasing magnetic field. The fact that only one absorption peak (T_0) is observed in the normal state ($d = 8$ nm) and slightly inverted ($d = 10$ nm)

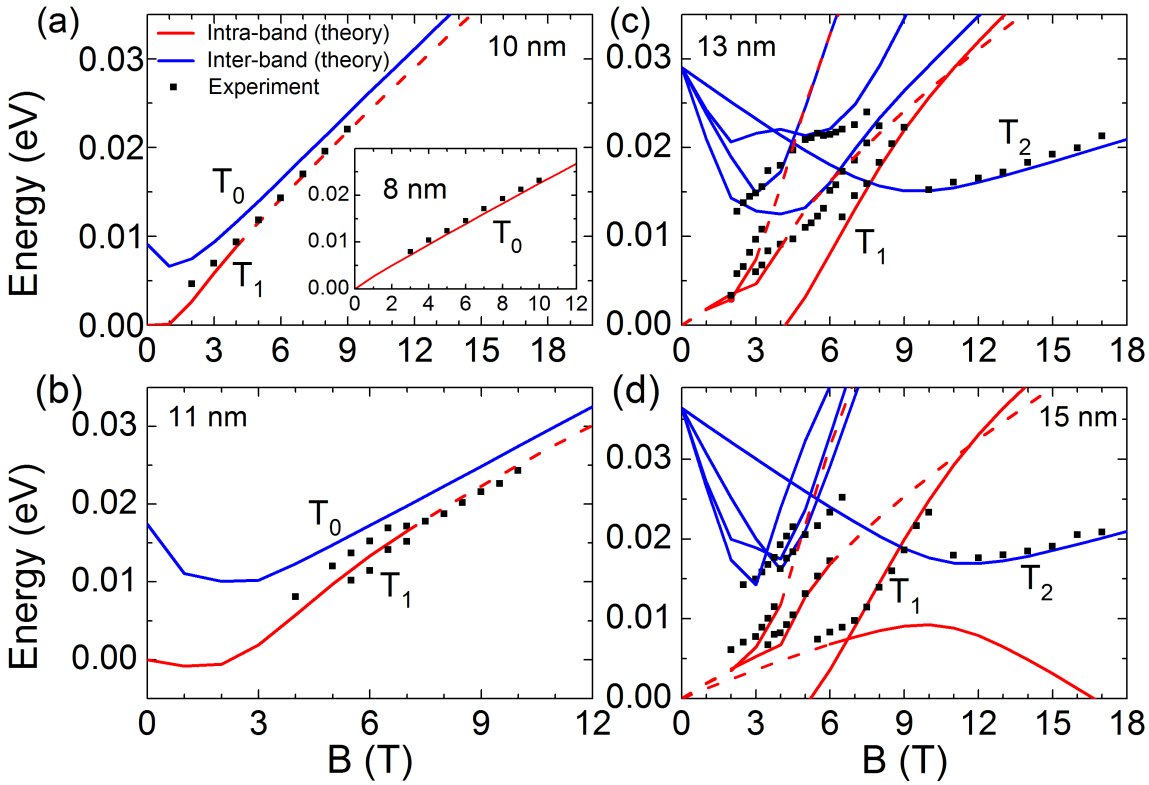

Figure 4.10: Magnetic field dependence of major absorption peaks. The absorption modes are plotted as a function of magnetic field both theoretically and experimentally for the $d = 8$ nm (inset to (a)), 10 nm (a), 11 nm (b), 13 nm (c), and 15 nm (d) InAs/GaSb DQW samples. The blue (red) solid lines represent the manifold-resolved inter-band (intra-band) transitions. For simplicity, we only label the commonly observed transitions, T_0, T_1, and T_2, in our samples. The red dashed lines indicate the diminishing absorption peaks (Pauli) blocked when the corresponding level crosses above the Fermi energy.

samples (Figs. 4.9(a) (b)) suggests an upper bound for the electron density, $n \leq 0.9 \times 10^{11}$ cm^{-2}. The slight broadening of the CR linewidth in the $d = 10$ nm sample at $B \leq 3$ T is indicative of the presence of the T_1 transition (Fig. 4.9(b)), which sets the lower bound for n. Therefore, one can conclude that $n = 0.9 \times 10^{11}$ cm^{-2} is a good approximation. The other variable used in our calculation is the effective mass of electrons in InAs QW, which is determined experimentally as $m_e^* = 0.024m$ by fitting to the CR (T_0) peak in the normal state ($d = 8$ nm) sample. Here, m is the bare electron mass. In the inverted state, the contribution of m_e^* to the band structure is coupled to that of the charge transfer effect discussed earlier. Therefore, m_e^* can only be extracted accurately from the normal state data. With this set of parameters, semi-quantitative agreement between the theory and experiment is reached for all five InAs/GaSb DQW samples across the normal and inverted states. We can also identify all the observed transitions with the help of manifold resolved calculation and summarized them in Fig. 4.10 and Tab. 4.2.

In addition to the T_0 transition, it is intriguing to investigate the T_1 (intra-band, $p : 0 \rightarrow 1$) and T_2 (inter-band, $p : 0 \rightarrow -1$) transitions denoted in Figs. 4.9 and 4.10. We note that in the normal state, T_1 is indiscernible from the T_0 transition. It starts to depart from T_0 when the band is slightly inverted (Figs. 4.10(a,b)), and thus it is responsible for the asymmetric lineshape observed in the $d = 11$ nm sample (Fig. 4.7(b)). As the band is further inverted, T_1 becomes a well-developed peak (Figs. 4.10(c,d)), but only occurs when the magnetic field lifts the $p = 1$ level (green) above the $p = 0$ level (black), as shown in Figs. 4.9(c,d). Therefore, T_1 can be used as an effective band-inversion indicator, and practically one can perform a linear-in-B fit to its energy at relatively high magnetic field, with the fitting intercept $y_0 \approx 0$ for the normal state, $y_0 < 0$ for the inverted state, and more negative value being more inverted. On the other hand, the T_2 transition only occurs in the inverted state and in the high-field region. It exhibits very weak B-dependence, distinct from all the other absorption peaks we have observed. We attribute this peak to a hole-like inter-band transition, $p : 0 \rightarrow -1$, due to the uplift of the heavy hole $p = -1$ level to the

Table 4.2: Detail assignment of all the observed transitions. The subbands are labeled with 3 components L_p^μ, where the letter L (C or H) stands for CB or VB, respectively, defined at $B = 0$. The subscript (superscript) is for PB index p (band label μ) and μ counts from the lowest energy level within the same p. Here, we only include the bands shown in Fig. 4.9, and a short line "$-$" means the transition is not observed in our experiment.

Label	8nm	10nm	11nm	13nm	15nm
T_0	$C_1^1 \to C_2^1$	$H_1^2 \to C_2^1$	$H_1^2 \to C_2^1$	–	–
T_1	–	$C_0^1 \to C_1^1$	$C_0^1 \to C_1^1$	$C_0^1 \to C_1^1$	$C_0^1 \to C_1^1$
T_2	–	–	–	$H_0^1 \to C_{-1}^1$	$H_0^1 \to C_{-1}^1$
T_3	–	–	–	$C_2^1 \to C_3^2$	$C_2^1 \to C_3^2$
T_4	–	–	–	$C_1^1 \to C_2^2$	$C_1^1 \to C_2^2$
T_5	–	–	–	–	$C_0^1 \to C_{-1}^1$
T_6	–	–	–	$H_1^2 \to C_2^1$	$H_2^2 \to C_3^2$
T_7	–	–	–	$H_1^2 \to C_2^2$	$H_2^1 \to C_3^1$
T_8	–	–	–	$H_1^1 \to C_2^1$	$H_1^2 \to C_2^2$

conduction band (i.e., band inversion). This observation is consistent with that reported in Ref. [49].

Lastly, we return to the magnetic field driven semimetal to semiconductor transition from the inverted to the normal state. As mentioned above, the heavy hole level ($p = -1$), inverted to the conduction band, would eventually cross below the lowest electron level ($p = 1$) with increasing magnetic field, driving the system back to the normal state. A critical field B_c can be defined at this crossing point (Figs. 4.9(b,c)), and the corresponding transition diagram is plotted in Fig. 4.11. The importance of the strain effect can also be seen in Fig. 4.11, as it significantly shifts the boundary between the inverted state and the magnetic field driven normal state. Practically, the strain effect can be engineered by choosing the appropriate substrate (typically, GaSb for pseudomorphic growth, GaAs for metamorphic growth) and the epi-structure [61].

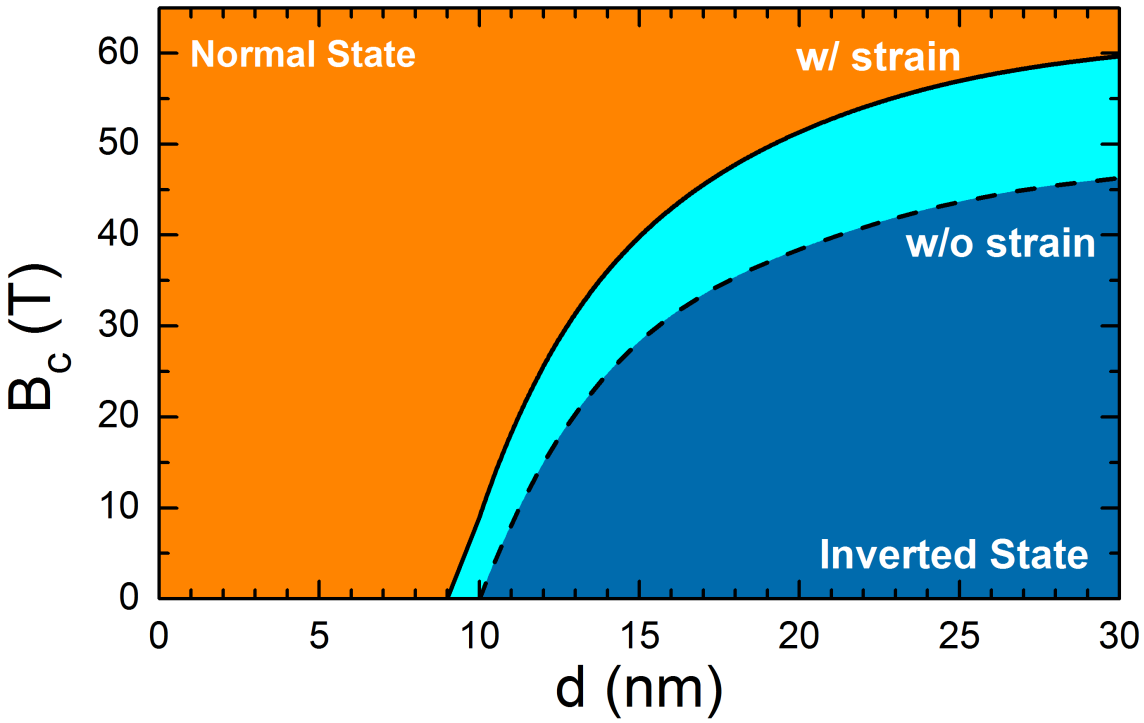

Figure 4.11: Phase diagram describing the magnetic field driven semimetal to semiconductor transition from the inverted to the normal state, with and without strain. The width of GaSb QW is fixed to 5 nm. For demonstration purpose only, we omit the lengthy self-consistency calculation in this diagram.

4.4 Conclusion

In conclusion, we have studied the LL structure of a series of InAs/GaSb DQWs from the normal to the inverted state using magneto-IR spectroscopy. We find that close to the intrinsic limit, the band inversion significantly modifies the magneto-absorption of the system, giving rise to multiple absorption peaks with distinct non-linear B-dependence. All the major absorption peaks observed in our experiment can successfully be explained using an eight-band PB model, with semi-quantitative agreement surpassing the previous two-band [53] and six-band [49] models.

CHAPTER 5

LANDAU LEVEL SPECTROSCOPY OF MASSIVE DIRAC FERMIONS IN $ZrTe_5$

5.1 Introduction to $ZrTe_5$

A major setback of the previously discovered 2D TIs, i.e., HgTe/CdTe QW and InAs/GaSb DQW systems, is their small bulk gaps limiting their applications at room temperature. Recently, zirconium pentatelluride ($ZrTe_5$), long recognized as a layered thermoelectric material [84], has attracted substantial interest in the wave of Dirac and topological material exploration [85]. The interest originates from the theoretical prediction of a large-gap ($\sim$ 100 meV, corresponding to $\sim$ 1100 K) QSH insulator phase (Fig. 5.1(b)) in its monolayer form [83]. Compared to other known 2D TIs requiring the state-of-the-art MBE growth, single/few layers of $ZrTe_5$ can be prepared by simple mechanical exfoliation thanks to its layered crystal structure. The crystal structure of $ZrTe_5$ is illustrated in Fig. 5.1(a), where chains of $ZrTe_3$ along the a-axis of are connected by Te atoms and form a 2D layer in the $a-c$ plane. These layers are stacked along the b-axis to form a bulk material which also has equally intriguing electronic properties (Fig. 5.1(c)). Theory predicts that the electronic structure of bulk $ZrTe_5$ resides near the phase boundary between weak and strong TIs and is very sensitive to the interlayer distance [83, 86], which makes it an ideal platform for studying topological phase transitions.

However, experiments from different groups have led to conflicting interpretations. The controversy is two-fold. First, $ZrTe_5$ thin flakes of several hundred nm in transport experiments exhibit a quasi-2D behavior [87–89] whereas ARPES measurements [90–95] show a 3D band structure. Second, different STM and ARPES experiments (Fig. 5.2) have disagreed on the topological nature of this material. In experiments supporting the weak TI interpretation, a bulk gap of $\sim$ 100 meV [91–93, 96] was reported but only the surface states

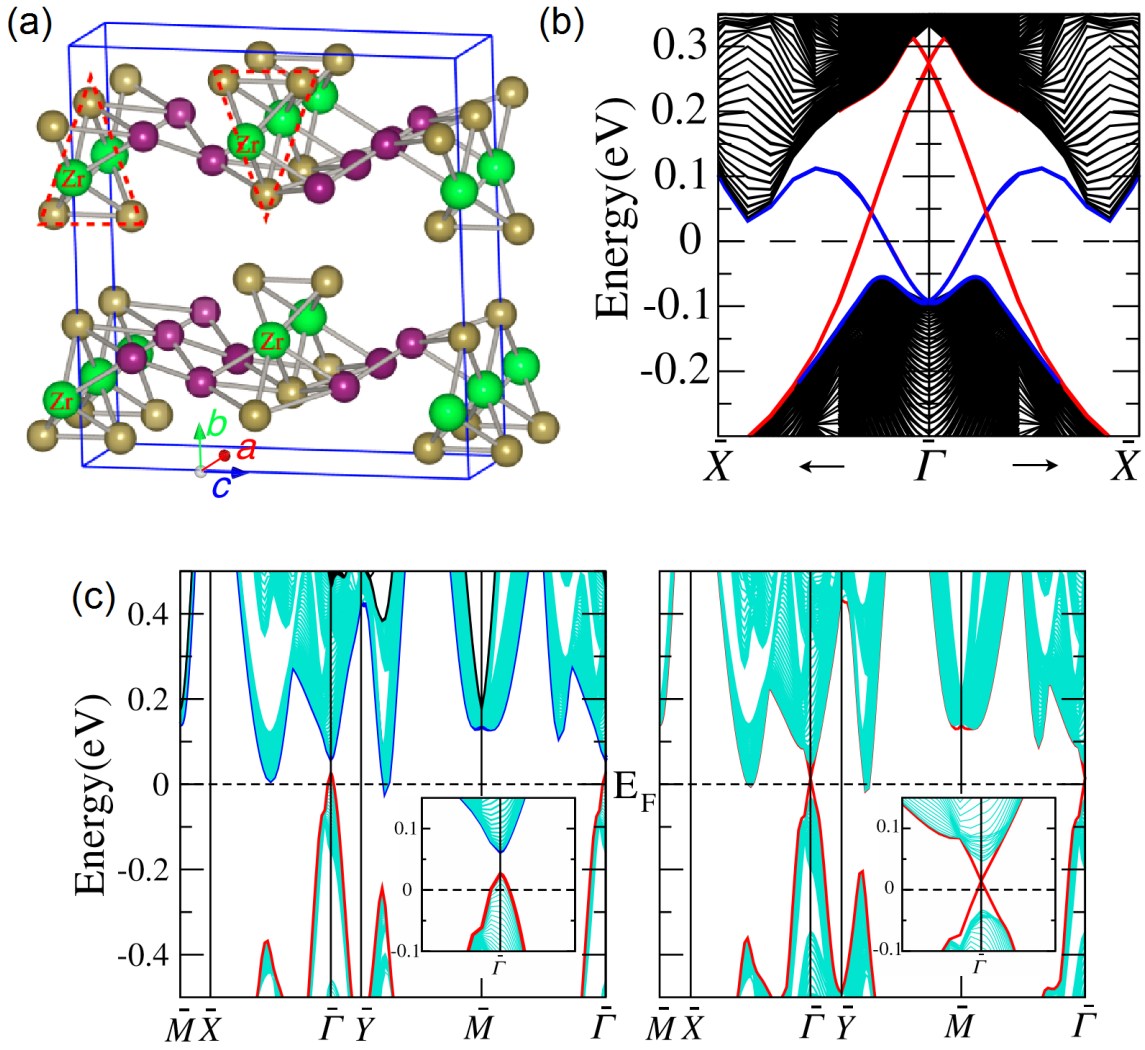

Figure 5.1: Band structure calculation of $ZrTe_5$. (a) The crystal structure of $ZrTe_5$. (b) Edge states within the bulk gap of monolayer $ZrTe_5$. The red and blue are the edge states terminated with the $ZrTe_3$ chain and Te zig-zag chain, respectively. (c) Band structure of $ZrTe_5$ in weak (left) and strong (right) TI phases, respectively. Adapted from Ref. [83].

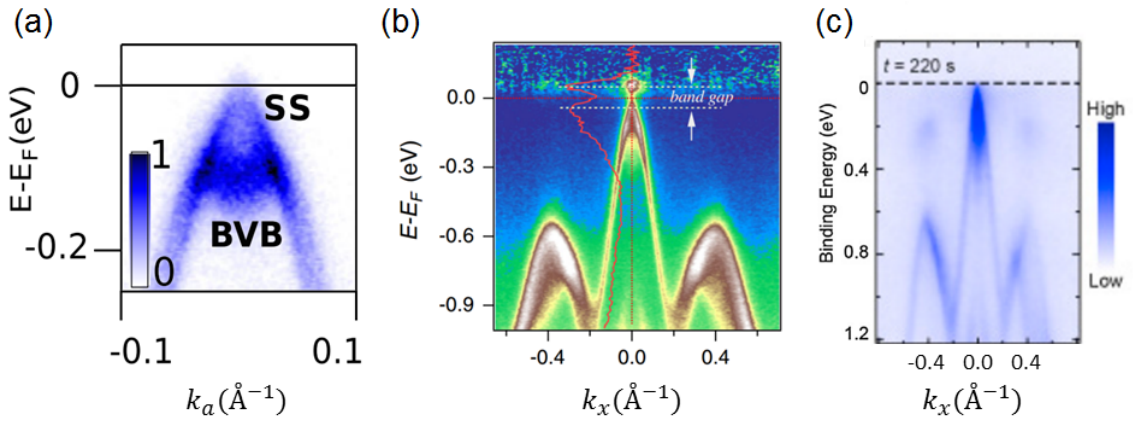

Figure 5.2: ARPES results on $ZrTe_5$ in literatures. ARPES results from different groups lead to conflicting interpretations ranging from (a) a strong TI, (b) a weak TI, and (c) a Dirac semimetal. Adapted from Refs. [93–95].

at step-edges [93, 96] can be observed. One ARPES [94] study also reported the presence of strong TI surface states, while a Dirac semimetal phase, which could be the boundary between strong and weak TI or between normal insulator and TI, was identified in other experiments [90, 95]. These contradicting observations may be related to the sensitive dependence of the topological phase of $ZrTe_5$ on the interlayer distance. Indeed, an indication of weak to strong TI transition induced by temperature has recently been reported in Ref. [92].

As for IR spectroscopy studies, recent reflectance measurements have suggested that bulk $ZrTe_5$ is a 3D massless Dirac semimetal [88, 97, 98]. Specfically, the zero field optical conductivity obtained by Kramers-Kronig (KK) transformation using a wide range of reflectance data gave a linear-in-energy dependence expected from a 3D Dirac band [97]. In a more recent magneto-reflectance measurement [98], the observed LL transitions can be described by a massless Dirac fermion model. However, the accuracy of the transition energies extracted from the reflectance measurements may be questioned since a true KK transformation cannot be implemented within the limited spectral range of magneto-IR reflectance measurements [88, 98]. Therefore, magneto-IR transmission measurements are needed to quantitatively describe the exact topological nature of $ZrTe_5$ since the real part

of the optical conductivity is directly proportional to the absorption amplitudes.

In this chapter, we will present the IR transmission magneto-spectroscopy study of mechanically exfoliated $ZrTe_5$ thin crystals near the intrinsic limit. Because of the low carrier density, we are able to observe a series of interband LL transitions that exhibit the characteristic dispersion of 2D massive Dirac fermions - a signature of the 2D Dirac semimetal electronic structure. We employ high-field magneto-spectroscopy with circularly polarized IR light to resolve a four-fold splitting of low-lying LL transitions, which is attributed to the combined effect of finite mass, large g-factor, and electron-hole asymmetry.

5.2 Experiment and results

5.2.1 Experiment

Single-crystal $ZrTe_5$ samples were synthesized by both the Te-assisted chemical vapor transport (CVT) method [99] and the molten Te flux growth [90]. The CVT growth started with polycrystalline $ZrTe_5$, which was prepared by reacting appropriate ratio of Zr and Te in an evacuated quartz tube at 450 °C for one week. Next, 2 g of polycrystalline $ZrTe_5$ along with transport agent (100 mg Te) were sealed in a quartz tube and placed horizontally in a tube furnace. The sample (source) was placed at the center of the furnace and heated up to 530 °C at a rate of 60 °C/hour. The growth zone (sink), which is 12 cm away from the center, was measured to be at a temperature of 450 °C.

In the flux growth, elemental Zr and Te were mixed in the molar ratio 1:400 and sealed under vacuum in a quartz tube. The mixture was heated at a rate of 50 °C/hour to 900 °C, held at this temperature for 72 hours, and then slowly cooled at a rate of 3 °C/hour to 445 °C, followed by re-melting the small crystals between 445 and 505 °C (by rapid heating at 60 °C/hour and slow cooling at 2 °C/hour for four times). Finally, the crystals were separated from the flux by centrifuging at 445 °C. To remove excess Te on the sample surface, we first seal the $ZrTe_5$ crystals back in an evacuated quartz tube, and then place it in a tube furnace that can create a temperature gradient. The hot and cold zone temperature

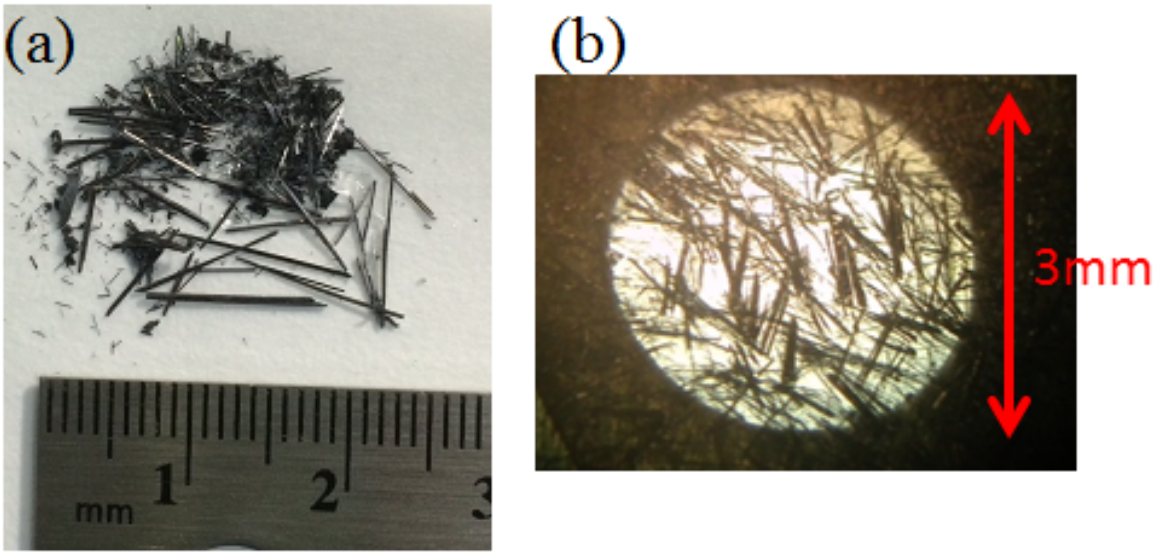

Figure 5.3: Optical images of $ZrTe_5$. (a) Flux-grown samples, (b) $ZrTe_5$/tape composite after exfoliation.

of the furnace is 400 °C and 350 °C, respectively. The crystals are placed in the hot zone for 24 hours, while the excess Te is transported to the cold zone. The optical image of as-grown crystal is shown in Fig. 5.3(a).

Room-temperature X-ray diffraction measurements were performed on both types of samples. Similar lattice constants were obtained, with $a = 3.985$ Å, $b = 14.526$ Å, and $c = 13.716$ Å for CVT-grown samples and $a = 3.988$ Å, $b = 14.505$ Å, and $c = 13.707$ Å for flux-grown samples. These values are consistent with that reported in the literature [90, 93].

Since $ZrTe_5$ has a layered structure with weakly van der Waals coupled layers along the b-axis (Fig. 5.1(a)), one can produce thin $ZrTe_5$ flakes with an average thickness of about 1 μm by repeatedly exfoliating the material with an IR-transparent Scotch tape. The resulting $ZrTe_5$/tape composite (Fig. 5.3(b)) enables IR transmission/absorption measurements. This method has been proven successful in the previous studies of graphite [100, 101] and TI materials such as Bi_2Te_3 [102].

Both broad-band and QCL based circular polarization resolved magneto-IR measurements were performed as described in Chapter 3 on the $ZrTe_5$/tape composites. All mea-

surements were performed in the Faraday configuration with the b-axis of the sample parallel to the magnetic field. In the discussion below, we only present results on the CVT-grown samples since the results in the flux-grown samples are similar [103].

5.2.2 Results and discussion

In Fig. 5.4(a), we plot the zero-field extinction spectrum, $1 - T/T_{\text{tape}}$, of $ZrTe_5$/tape composite measured at 25 K. Here, the sample spectrum (T) is referenced to the transmission through a bare tape (T_{tape}). At low photon energies, the extinction coefficient, and consequently, the absorption (A) first increases with energy (E) and then becomes spectrally flat at $E > 75$ meV. It is important to note that our sample is still transparent in the flat region, as evidenced by the additional absorptions of LL transtions observed in the same energy range (to be shown later). Therefore, the flat response can not be explained by complete reflection. In addition, this behavior clearly deviates from the expected linear dependence, $A \propto E$, for 3D Dirac semimetals [104], and differs our thin flake samples from the thick, opaque samples studied in Refs. [97, 98], where a 3D massless Dirac semimetal electronic structure was concluded for $ZrTe_5$. Moreover, our data are similar to that observed in graphene [105, 106], the best known material system hosting 2D Dirac fermions, for the entire experimental spectral range. Due to its 2D nature, $A = const.$ in mono-, bi-, and multi-layer graphene at high photon energies [107–110]. This 2D Dirac fermion speculation is supported by recent transport studies on $ZrTe_5$ thin flakes [87–89, 111].

To elucidate the electronic structure of $ZrTe_5$ thin flakes, we carry out systematic low-temperature IR transmission measurements in magnetic fields up to $B = 16$ T. Figure. 5.4(b) shows a normalized transmission spectrum taken at $B = 2$ T featuring a characteristic, graphene-like series of absorption minima. Indeed, the transition energies, which can be readily and accurately determined from the central energy of the absorption line, can be assigned to a series of interband LL transitions from $L_{-n(-n-1)}$ to $L_{n+1(n)}$ with the integer n (or $-n$) being the LL index. The LL spectrum of 2D Dirac fermions such as that

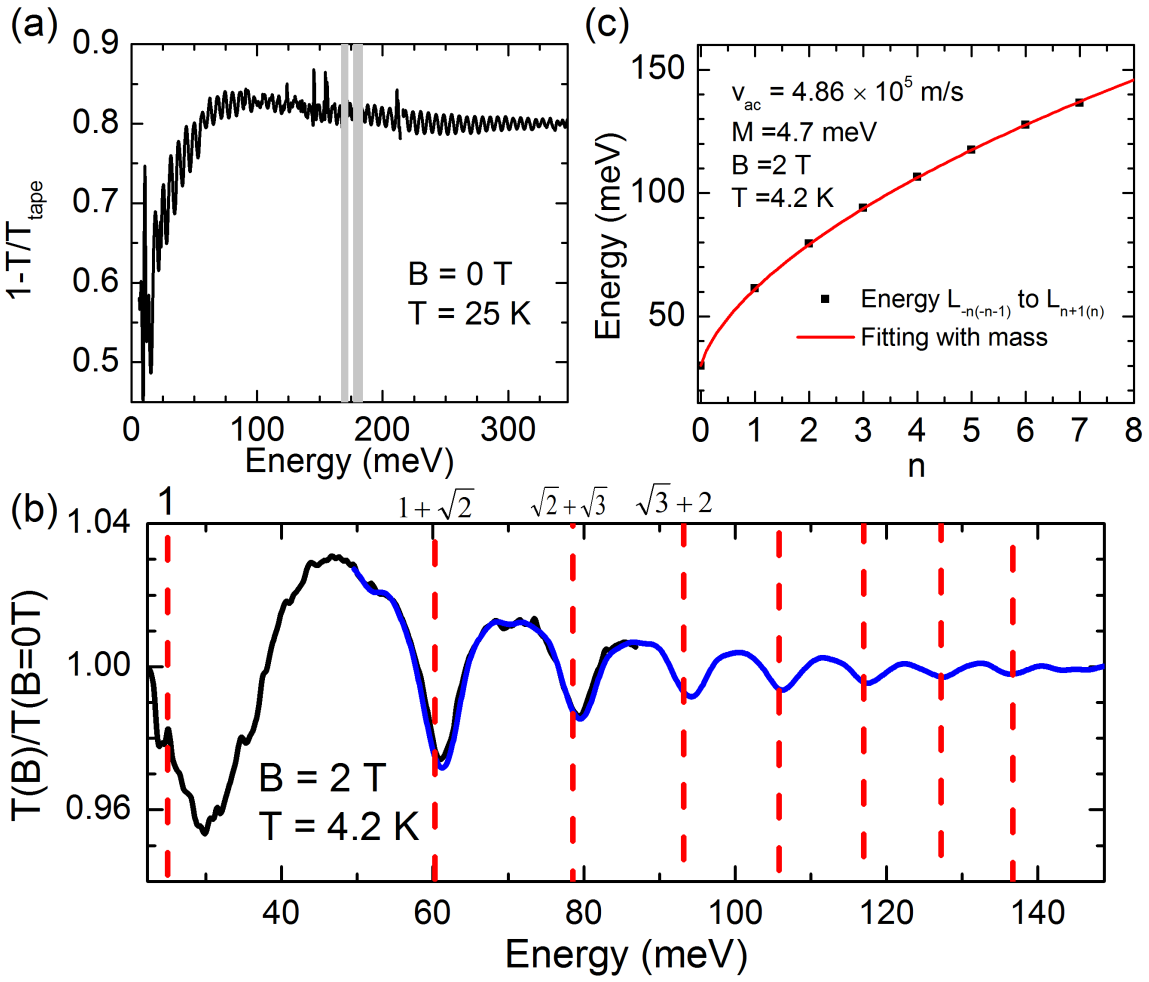

Figure 5.4: 2D massive Dirac fermions in $ZrTe_5$. (a) Extinction spectrum, $1 - T/T_{\text{tape}}$, of $ZrTe_5$/tape composite measured at $B = 0$ T and $T = 25$ K. The fast oscillations originate from Fabry-Pérot interference. The gray stripes cover opaque regions due to tape absorption. (b) Normalized transmission spectrum, $T(B)/T(B = 0)$, measured at $B = 2$ T and $T = 4.2$ K. The black and blue curves correspond to the far-IR and the mid-IR spectrum, respectively. The red dash lines mark the expected energies of $L_{-n(-n-1)} \rightarrow L_{n+1(n)}$ transitions for massless Dirac fermions. (c) Extracted LL transition energy from (c) as a function of LL index n. The red line shows the best fit to the data using Eq. (5.1).

in graphene can be described as

$$E_n = \alpha\sqrt{2e\hbar v_F^2 nB + M^2}, \tag{5.1}$$

where E_n is the energy of the nth LL, v_F is the Fermi velocity, M is the Dirac mass, and $\alpha = \pm 1$ stands for the CBs and VBs, respectively. For massless Dirac fermions, $E_n \propto \sqrt{n}$, leading to the characteristic $E_{-n\rightarrow n+1} \propto \sqrt{n} + \sqrt{n+1}$ dependence of optically allowed interband LL transitions $L_{-n} \rightarrow L_{n+1}$ [112, 113]. For massive Dirac fermions ($M \neq 0$), however, E_n deviates from a perfect $\sqrt{n}$ dependence [114]. The deviation becomes more pronounced for low-lying LL transitions when n is small. Such a massive Dirac fermion scenario can precisely describe our data at low magnetic fields. The vertical dash lines in Fig. 5.4(b) indicate transition energies following a model $\sqrt{n} + \sqrt{n+1}$ dependence, with the parameter v_F determined by the highest energy transition ($n = 7$). The measured energies of LL transitions exhibit a clear blueshift, particularly for low-lying transitions, suggesting the massive Dirac fermion interpretation. A more quantitative analysis is shown in Fig. 5.4(c), where the extracted transition energies are plotted as a function of n and fitted with Eq. (5.1). The best fit to the data gives $M = 4.7$ meV (corresponding to a 9.4 meV energy gap) and $v_F = 4.86 \times 10^5$ m/s. The latter is the average Fermi velocity in the *ac* plane of $ZrTe_5$ and its value is consistent with recent transport [115], ARPES [92] and IR [98] measurements.

The observation of a small Dirac mass of $M = 4.7$ meV is not a surprise. In theory, the Dirac point in semimetals is an accidental degeneracy when the VBs and CBs touch [116–119]. Without symmetry protection, level repulsion will automatically opens a gap at the Dirac point, equivalent to generating a Dirac mass. In addition, the lowest energy transition observed is $L_{0(-1)} \rightarrow L_{1(0)}$, which implies that our sample is in the quantum limit. This transition is visible at the magnetic field as low as 0.5 T, corresponding to a Fermi energy $\leq$ 16 meV. Therefore, our samples are close to the intrinsic limit, suited

for magneto-IR spectroscopy studies. Also, we note that the Lorentzian lineshape of LL transitions (Fig. 5.4(c)) provides another indication in favor of a 2D Dirac fermion picture, as the k_z dispersion in a 3D system would lead to an asymmetric lineshape with abrupt cutoff on the low-energy side [21].

Figure 5.5(a) illustrates the magnetic field dependence of the LL transitions and their splitting in high magnetic fields, particularly for the three lowest interband transitions: $L_{0(-1)} \rightarrow L_{1(0)}$, $L_{-1(-2)} \rightarrow L_{2(1)}$, and $L_{-2(-3)} \rightarrow L_{3(2)}$. The splitting of the $L_{0(-1)} \rightarrow L_{1(0)}$ transition was previously observed in magneto-IR reflectance measurements [98], but the proposed interpretation suffers from the requirement of two sets of g-factors. To explore the origins of the splitting, we performed magneto-IR circular polarization resolved measurements using mid-IR QCLs. Magneto-spectroscopy with circularly polarized light has been successfully employed in the past to reveal details of specific LL transitions in graphite [120], and more recently in graphene [121] and in a typical 3D TI Bi_2Se_3 [122]. Here, we focus on the $L_{-1(-2)} \rightarrow L_{2(1)}$ transition, which overlaps well the spectral range of our QCLs. The circular polarization resolved spectra are taken by fixing the light polarization and sweeping the magnetic field in positive or negative directions, which is equivalent to the use of σ^+ and σ^- polarized light.

Figure 5.6 shows the normalized transmission through $ZrTe_5$/tape composite as a function of magnetic field with the QCL energy fixed at different photon energies. With unpolarized IR light, a four-fold splitting of the $L_{-1(-2)} \rightarrow L_{2(1)}$ transition clearly reproduces that measured at $B = const.$ (Fig. 5.5). In a circularly polarized configuration, only two of the four split transitions are active in σ^+ or σ^- polarized light. This observation indicates the lifting of the degeneracy between the $L_{-1} \rightarrow L_2$ ($\Delta n = 1$, σ^+ active) and $L_{-2} \rightarrow L_1$ ($\Delta n = -1$, σ^- active) transitions, which can be attributed to an asymmetry between the electron and hole bands.

Next, we show that the remaining two-fold splitting of the $L_{-1} \rightarrow L_2$ (or $L_{-2} \rightarrow L_1$) transition reflects the lifting of the spin degeneracy, due to a combined effect of large g-

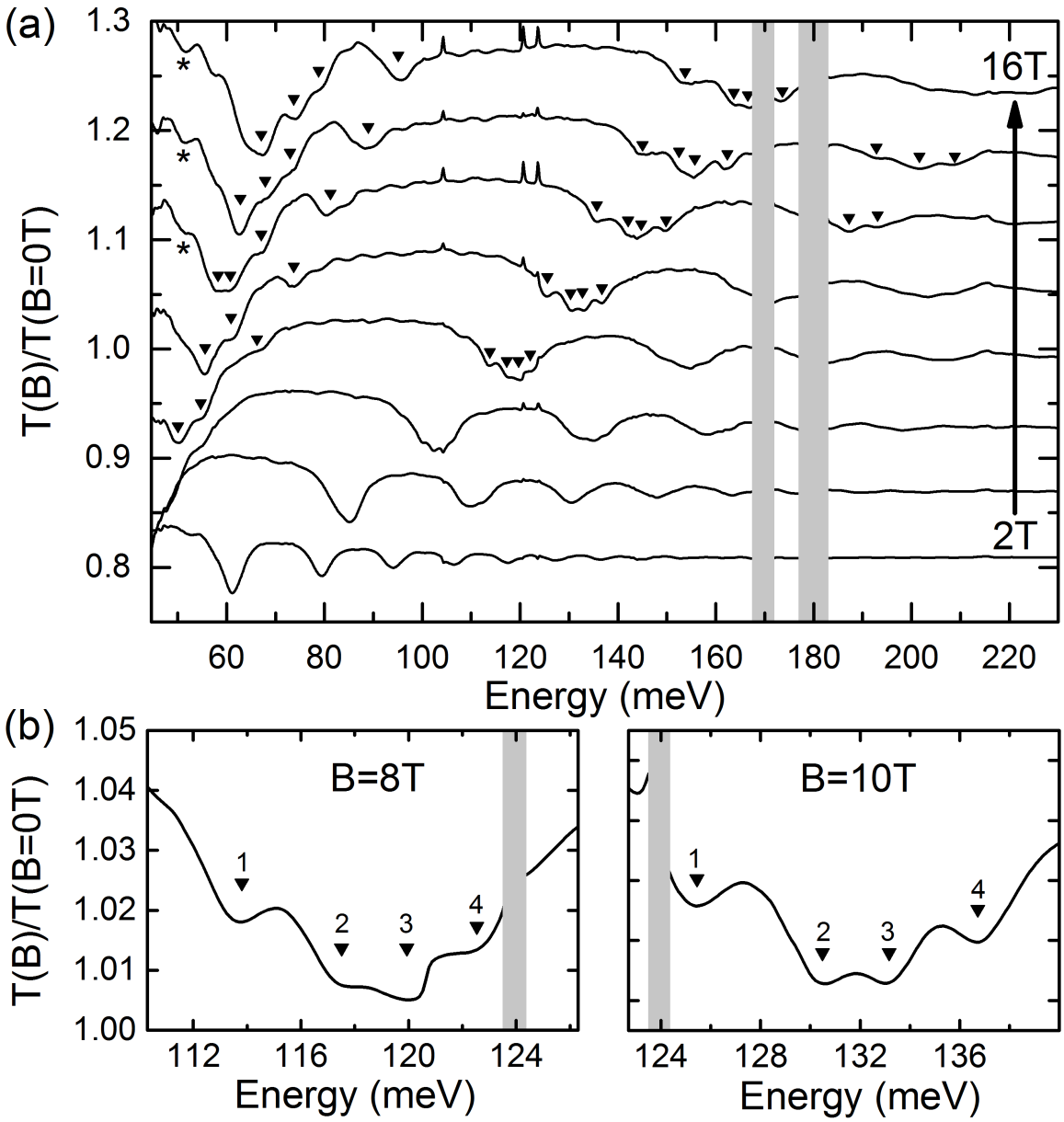

Figure 5.5: LL splittings at high magnetic fields. (a) Normalized transmission spectra, $T(B)/T(B = 0\text{T})$, of $ZrTe_5$/tape composite measured at selected magnetic fields. The down triangles (▼) label the splitting of low-lying LL transitions, while the star symbols ($\star$) point to B-independent spectral features originating from the normalization process. (b) Zoom-in view of the four-fold splitting of the $L_{-1(-2)} \rightarrow L_{2(1)}$ transition taken at $B = 8$ T and 10 T. In all panels, the spectra are offset vertically for clarity and the gray stripes cover opaque regions due to tape absorption.

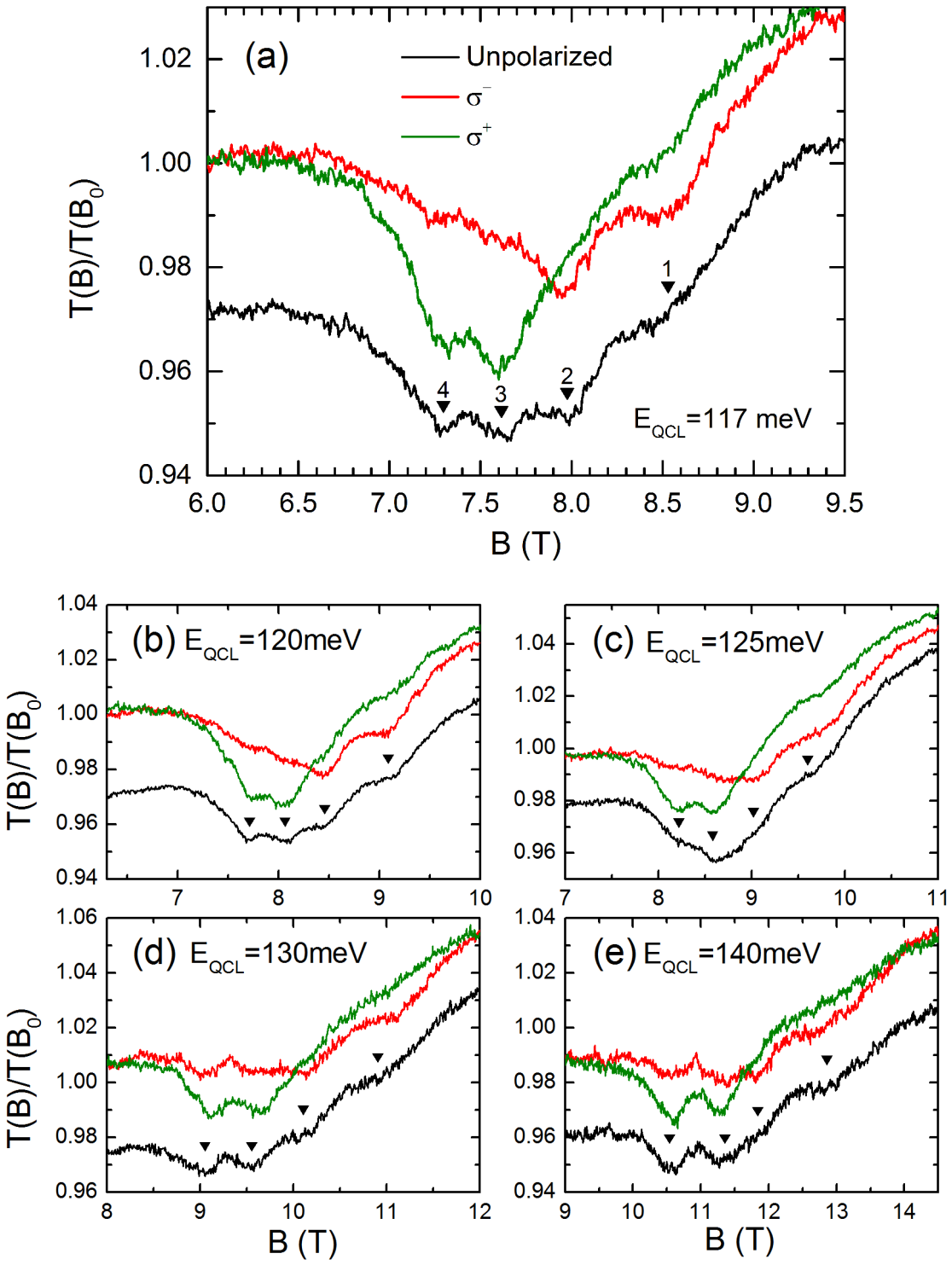

Figure 5.6: Circular polarization resolved transmission measurements. (a) Normalized transmission, $T(B)\ /T(B_0\ =\ 6$ T), as a function of magnetic field using unpolarized (black) and circularly polarized (red and green) IR light of 117 meV. Similar results are observed with incident light energy of (b) 120, (c) 125, (d) 130, and (e) 140 meV. The reference magnetic field B_0 is 6, 7, 8, and 9 T for (b-e), respectively. The four-fold splitting of the $L_{-1(-2)} \rightarrow L_{2(1)}$ transition is labeled by down triangles (▼) on the unpolarized data which is offset vertically for clarity.

factor (Zeeman effect) and finite mass. We begin with an effective Hamiltonian postulated by Bernevig, Hughes, and Zhang [8]

$$H(\mathbf{k}) = \epsilon_0(\mathbf{k}) + \begin{pmatrix} L(\mathbf{k}) & Ak_+ & 0 & 0 \\ Ak_- & -L(\mathbf{k}) & 0 & 0 \\ 0 & 0 & L(\mathbf{k}) & -Ak_- \\ 0 & 0 & -Ak_+ & -L(\mathbf{k}) \end{pmatrix},$$

where $\epsilon_0(\mathbf{k}) = C - D(k_x^2 + k_y^2)$, $L(\mathbf{k}) = M - \mathscr{B}(k_x^2 + k_y^2)$, $k_\pm = k_x \pm ik_y$, and k^4 terms neglected [118]. The derivation of this Hamiltonian can be found in Appendix C. The actual electronic structure is then determined by a set of material parameters: (1) $A = \hbar v_F$, (2) band inversion parameter $\mathscr{B}$, (3) energy offset C (which is set to zero), (4) electron-hole asymmetry parameter D, and (5) Dirac mass M. In the presence of a magnetic field, one can add the Zeeman term [123, 124], $\frac{\mu_B B}{2}\begin{pmatrix} g & 0 \\ 0 & -g \end{pmatrix}$, where μ_B is the Bohr magneton, $g = \begin{pmatrix} g_e & 0 \\ 0 & g_h \end{pmatrix}$, and g_e (g_h) are the effective g-factors for CBs (VBs), and solve the eigenvalue problem for the LL spectrum of massive Dirac fermions in $ZrTe_5$ thin flakes

$$\begin{aligned} E_0^{\uparrow} &= M - (D + \mathscr{B})\frac{eB}{\hbar} + \frac{\mu_B g_e}{2}B, \quad E_0^{\downarrow} = -M - (D - \mathscr{B})\frac{eB}{\hbar} - \frac{\mu_B g_h}{2}B, \quad n = 0 \\ E_{n,\alpha}^{s} &= -(2Dn + s\mathscr{B})\frac{eB}{\hbar} + s\frac{\mu_B \bar{Z}}{2}B \\ &\quad + \alpha\sqrt{2A^2 n\frac{eB}{\hbar} + \left[M - (2\mathscr{B}n + sD)\frac{eB}{\hbar} + s\frac{\mu_B \delta Z}{2}B\right]^2}. \quad n \neq 0 \end{aligned} \tag{5.2}$$

Here, $s = \uparrow\downarrow = \pm 1$ stands for the spin-up and spin-down LLs, $\bar{Z} = \frac{g_e + g_h}{2}$ is the average g-factor, and $\delta Z = \frac{g_e - g_h}{2}$. In the low-field limit, Eq. (5.2) reduces to Eq. (5.1). It should be emphasized that the Zeeman effect alone cannot lift the spin degeneracy of LL transitions even when considering electron-hole asymmetry, $D \neq 0$ and $\delta Z \neq 0$. This can be seen in

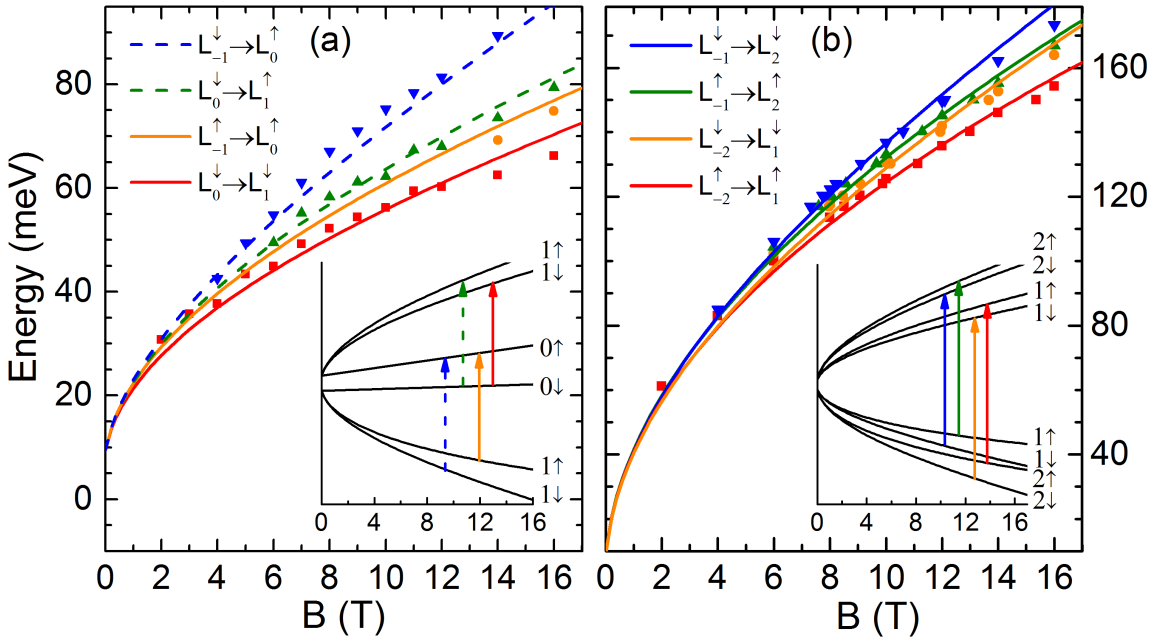

Figure 5.7: Magnetic field dependence of the four-fold splitting of low-lying LL transitions. The extracted energies (symbols) from both the broad-band and QCL-based measurements are fit with Eq. (5.2) (lines) for the (a) $L_{0(-1)} \rightarrow L_{1(0)}$ and (b) $L_{-1(-2)} \rightarrow L_{2(1)}$ transitions. The corresponding transitions are illustrated in the insets with the same color code. The solid and dash lines denote the spin-conserved strong transitions and the spin-flipped weak transitions, respectively.

Eq. (5.2), where a finite mass, $M \neq 0$ and/or $\mathscr{B} \neq 0$, is required to distinguish the $[\cdots]^2$ term for $s = \pm 1$. Therefore, the observed four-fold splitting of low-lying LL transitions provides another evidence of finite mass for the Dirac fermions in $ZrTe_5$ thin flakes.

Figure 5.7(b) shows the four-fold splitting of the $L_{-1(-2)} \rightarrow L_{2(1)}$ transition as a function of magnetic field and the color-coded lines are best fits to the data using Eq. (5.2). The associated fitting parameters are $v_F = 4.65 \times 10^5$ m/s, $\mathscr{B} = 341$ meV nm^2, $D = -126$ meV nm^2, $M = 4.71$ meV, $g_e = 24.3$, and $g_h = 7.5$. Here, M is consistent with that obtained from Fig. 5.4(c) while v_F is $\sim$4% smaller, and $D < 0$ implies a steeper CB than the VB. Interestingly, we notice that a smaller v_F is also needed to better describe the high-field data in Ref. [123].

To further validate our model, we checked if the above parameters allow to describe other split transitions, and found a very good agreement for the $L_{0(-1)} \rightarrow L_{1(0)}$ transition

(Fig. 5.7(a)). Due to the strong spin-orbit coupling in $ZrTe_5$, spin-flipped LL transitions ($L_0^{\downarrow} \rightarrow L_1^{\uparrow}$ and $L_{-1}^{\downarrow} \rightarrow L_0^{\uparrow}$) are allowed and assigned to the two relatively weak high-energy modes of the $L_{0(-1)} \rightarrow L_{1(0)}$ splitting. The four-fold splitting of the $L_{-1(-2)} \rightarrow L_{2(1)}$ transition, on the other hand, is related to the four strong spin-conserved modes, as the associated spin-flipped modes are expected to be very weak.

Lastly, our model predicts that additional splitting of the $L_{0(-1)} \rightarrow L_{1(0)}$ transition into $L_0^{\uparrow} \rightarrow L_1^{\uparrow}$ ($L_{-1}^{\downarrow} \rightarrow L_0^{\downarrow}$) may occur at lower energies due to the presence of a small amount of electron (hole) doping. Quantitative study of this mode, however, is hindered by a field-independent spectral feature at $\sim$52 meV (labeled by star symbol in Fig. 5.5(a)) and thus not pursued in this work.

5.3 Conclusion

In conclusion, we have performed IR transmission measurements on exfoliated $ZrTe_5$ near the intrinsic limit. The electronic structure of $ZrTe_5$ thin crystals is found to be 2D-like and support a Dirac semimetal interpretation but with a small relativistic mass (or gap). High-field magneto-spectroscopy measurements reveal a four-fold splitting of low-lying LL transitions and circular polarization resolved measurements show that two-fold comes from breaking the electron-hole symmetry while the other two-fold is caused by lifting the spin degeneracy. The magnetic field dependence of the splitting can be fully described using the BHZ effective Hamiltonian model.

CHAPTER 6
CLOSING REMARKS AND OUTLOOK

TIs have emerged as a new class of quantum matters in which the bulk is fully gapped but the surface/edge holds robust gapless states against disorders and external disturbance under the protection of symmetries. In this thesis, we use magneto-IR spectroscopy to study the electronic band strucutres of two TI candidates: InAs/GaSb DQWs and thin-flake $ZrTe_5$.

In InAs/GaSb DQWs, our combined theoretical and experimental study has demonstrated that the emergence of multiple absorption modes in the intrinsic limit can be attributed to the quantum phase transition from the normal to the inverted band structure. Such quantum phase transition can also be interpreted as a topological phase transition from normal insulator to TI, which has not been appreciated until recent developments of topological band theory. We further show that the quantum phase transition can be controlled by three effects: magnetic field, quantum confinement and strain, which vastly expand the parameter space for manipulating the transition.

Among the above three effects, the magnetic-field driven transition requires the system in an inverted state at zero field, since the electron and hole energies can only be tuned in one way with magnetic field. The quantum confinement effect and strain effect, however, can tune the relative positions of energy levels in both CBs and VBs, enabling a two-way manipulation between the normal and the inverted state. In addition, it is known that the band gap in semiconductors also depends on temperature [125], which could be another external parameter to control the topological phase in this system.

In $ZrTe_5$, the energy independent optical response in the zero field mid-IR transmission suggests a quasi-2D band structure, which is echoed by the symmetric lineshape in the observed LL transitions at low magnetic fields. The LL transitions also exhibit a characteristic

square root dependence on both magnetic field and LL index, signifying the presence of Dirac fermions in the system but with a small relativistic mass. At high magnetic fields, the low lying LL transitions exhibit a four-fold splitting, whose circular polarization dependence reveals symmetry breaking between the CB and VB and between different spin states. We show that all our observations can be quantitatively explained within the BHZ model. It should be noted that the BHZ model requires an energy gap to lift the spin degeneracy, thus lending another evidence for the massive Dirac fermions. The energy gap can naturally arise when the CB and VB anti-cross each other. Therefore, we believe that our thin flake $ZrTe_5$ is a Dirac semimetal, residing at the boundary between a normal insulator and a TI or between a weak TI and a strong TI.

To further elucidate the topological nature of the band structure, it is important to conduct a more thorough study in different crystal planes. An undergoing experiment along this line is to apply an in-plane magnetic field so that the out-of-plane information can be reflected in the cyclotron motions. Moreover, since $ZrTe_5$ is a Dirac semimetal, it is also interesting to study the topological phase transition on the interlayer distance, where temperature or external pressure may be an effective control as that in InAs/GaSb DQWs.

As a final remark, $ZrTe_5$ may accomodate much more profound physics than just its band topology. Recent studies have reported in $ZrTe_5$ the observation for the long sought chiral magnetic effects in high energy physics [90]. In addition, it has been proposed that by breaking the time reversal or inversion symmetry, the Dirac bands may be split into two non-degenerate modes in analogue to the Weyl modes in Dirac equations, which opens up the study of Weyl fermions in solid state system [85]. With further understanding in its topological phase, $ZrTe_5$ is promising in providing a fertile playground in discovering novel quantum particles in condensed matters.

Appendices

APPENDIX A

QUASI-DEGENERATE PERTURBATION THEORY

For a Hamiltonian H, assuming we have a set of orthogonal approximate eigenfunctions $\{\phi_n\}$, the exact eigenfunction can be approximated by

$$\Phi \approx \sum_n C_n \phi_n, \tag{A.1}$$

where C_n is the expansion coefficient of the basis ϕ_n. If the set $\{\phi_n\}$ is complete, this relation is exact. Using the orthogonal relations, one can find that the eigenvalue problem $H\Phi = E\Phi$ can be written as

$$\sum_n [H_{mn} - E\delta_{mn}]C_n = 0. \tag{A.2}$$

This is equivalent to calculating the determinant of the matrix H_{mn}, where $H_{mn} = \int \phi_m^* H \phi_n$.

We can divide Eq. (A.1) into two parts:

$$\Phi = \sum_{n\in A} C_n \phi_n + \sum_{n\in B} C_n \phi_n, \tag{A.3}$$

where set A includes the eigenstates of interests and set B is composed of the other states. Since we are only interested in finding the eigenenergies for the states in set A, we only need to find a matrix that only connects the coefficients in set A.

From Eq. (A.2), we can calculate any coefficient C_m through

$$C_m = \sum_{n\in A} h'_{mn} C_n + \sum_{n\in B} h'_{mn} C_n, \tag{A.4}$$

where $h'_{mn} = \frac{H'_{mn}}{E - H_{mm}}$ and $H'_{mn} = H_{mn} - H_{mn}\delta_{mn}$. The coefficient for the basis function

in set B can be removed by repeatedly using Eq. (A.4)

$$\begin{aligned} C_m &= \sum_{n\in A} h'_{mn}C_n + \sum_{n\in B} h'_{mn}[\sum_{\alpha\in A} h'_{n\alpha}C_\alpha + \sum_{\alpha\in B} h'_{n\alpha}C_\alpha] \\ &= \sum_{n\in A} h'_{mn}C_n + \sum_{\alpha\in A}\sum_{n\in B} h'_{mn}h'_{n\alpha}C_\alpha + \big[\sum_{\beta\in A}\sum_{n\alpha\in B} + \sum_{n,\alpha,\beta\in B}\big] h'_{mn}h'_{n\alpha}h'_{\alpha\beta}C_\beta. \end{aligned} \tag{A.5}$$

Since this substitution can go on infinitely, we can truncate the last term if $h'_{mn} \ll 1$ for $m, n \in B$. Now,

$$\begin{aligned} C_m &= \sum_{n\in A}[h'_{mn} + \sum_{\alpha\in B} h'_{m\alpha}h'_{\alpha} + \sum_{\alpha\in B}\sum_{\beta\in B} h'_{m\alpha}h'_{\alpha\beta}h'_{\beta n}]C_n \\ &= \frac{1}{E - H_{mm}}\sum_{n\in A}[H'_{mn} + \sum_{\alpha\in B}\frac{H'_{m\alpha}H'_{\alpha n}}{(E - H_{\alpha\alpha})} + \sum_{\alpha\in B}\sum_{\beta\in B}\frac{H'_{m\alpha}H'_{\alpha\beta}H'_{\beta n}}{(E - H_{\alpha\alpha})(E - H_{\beta\beta})}]C_n, \end{aligned}$$

$$\text{so that} \quad (E - H_{mm})C_m = \sum_{n\in A}[U_{mn} - H_{mn}\delta_{mn}]C_n,$$

$$\text{where} \quad U_{mn} = H_{mn} + \sum_{\alpha\in B}\frac{H'_{m\alpha}H'_{\alpha n}}{(E - H_{\alpha\alpha})} + \sum_{\alpha\in B}\sum_{\beta\in B}\frac{H'_{m\alpha}H'_{\alpha\beta}H'_{\beta n}}{(E - H_{\alpha\alpha})(E - H_{\beta\beta})}.$$

For $m \in A$

$$\sum_{n\in A}[U_{mn} - E\delta_{mn}]C_n = 0. \tag{A.6}$$

The renormalized Hamiltonian matrix U_{mn} only involves the states in set A while maintaining the influence from the other states in the summation. Solving Eq. (A.6) gives the eigenvalues for the interested states. Note that, in principle, the eigenenergies need to be solved self-consistently. However, one can use the eigenvalue before including the effects from other states as an approximation to U_{mn}, if it is known.

APPENDIX B

SOLVING COUPLED DIFFERENTIAL EQUATIONS USING PLANE WAVE EXPANSION

There are many methods to solve a set of coupled differential equations. The plane wave expansion method has its unique advantage because it converges fast even with a small set of basis expansions, therefore the computation load is much smaller compared to other methods. In addition, the plane wave expansion is a widely used technique in solid state band structure calculations and can be easily adpated to other problem requiring solving coupled differential equations.

In the envelope function theory, the envelope function of the ith spinnor component can be expanded with a series of plane waves [126]

$$f_i(z) = \frac{1}{\sqrt{L}} \sum_{m=-N}^{N} c_{im} e^{ik_m z} = \sum_m c_{im} \left|\phi_m\right\rangle, \quad i = 1, 2, \cdots, 8, \tag{B.1}$$

where L is the total width of the QW structure, and $k_m = m\frac{2\pi}{L}$ is the wave vector of a basis with m being an integer. The basis are truncated at $m = \pm N$.

With this expansion, the coupled differential equations $H\psi = E\psi$ can be rewritten as

$$H_{ij} f_j = E f_i \rightarrow H_{ij} c_{jm} \left|\phi_m\right\rangle = E c_{im} \left|\phi_m\right\rangle. \tag{B.2}$$

Here, Einstein summation is used to simplify the notation. Using the orthogonal relations between the basis, we can arrive at the following equation

$$\left\langle\phi_n\right| H_{ij} \left|\phi_m\right\rangle c_{jm} = E c_{in}. \tag{B.3}$$

Note that now each element of the Hamitonian matrix is expanded to a $2N+1$ by $2N+1$

matrix

$$H_{ij} = \begin{pmatrix} H_{ij}^{0} & H_{ij}^{-1} & H_{ij}^{-2} & \cdots & H_{ij}^{-2N} \\ H_{ij}^{1} & H_{ij}^{0} & H_{ij}^{-1} & \cdots & H_{ij}^{-2N+1} \\ \vdots & \vdots & \vdots & \vdots & \vdots \\ H_{ij}^{N-n} & \cdots & H_{ij}^{n-m} & \cdots & H_{ij}^{-N+n} \\ \vdots & \vdots & \vdots & \vdots & \vdots \\ H_{ij}^{2N+1} & \cdots & \cdots & \cdots & H_{ij}^{0} \end{pmatrix},$$

where $H_{ij}^{n-m} = \langle \phi_n | \, H_{ij} \, | \phi_m \rangle$ is the $(n-m)$th Fourier component of the H_{ij} operator.

One needs to pay special attention to the order of the operator with respect to the relevant parameters. Here, we symmetrize each Hamiltonian to ensure the Hermicity of the matrix as follows

$$H_{ij} = A + B\hat{k_z} + C\hat{k_z}^2 = A + \frac{(B\hat{k_z} + \hat{k_z}B)}{2} + \hat{k_z}C\hat{k_z}. \tag{B.4}$$

Therefore, the Fourier component of the Hamiltonian is

$$\langle \phi_n | \, H_{ij} \, | \phi_m \rangle = \langle \phi_n | \, A \, | \phi_m \rangle + \frac{k_m + k_n}{2} \langle \phi_n | \, B \, | \phi_m \rangle + k_m k_n \langle \phi_n | \, C \, | \phi_m \rangle . \tag{B.5}$$

If $m \neq n$,

$$\langle \phi_n | \, A \, | \phi_m \rangle = \sum_j \int_{z_j}^{z_{j+1}} A^j [\Theta(z - z_j) - \Theta(z - z_{j+1})] e^{ik_{m-n}z} \frac{dz}{L} \tag{B.6}$$

$$= \sum_j \frac{iA^j}{k_{m-n}L} [e^{ik_{m-n}z_j} - e^{ik_{m-n}z_{j+1}}]. \tag{B.7}$$

If $m = n$,

$$\langle \phi_n | \, A \, | \phi_m \rangle = \sum_j \int_{z_j}^{z_{j+1}} A^j [\Theta(z - z_j) - \Theta(z - z_{j+1})] \frac{1}{L} dz = \sum_j \frac{A^j}{L} [z_{j+1} - z_j]. \tag{B.8}$$

Here, A^j denotes the parameter for the constituent material in the jth QW which starts at position z_j.

With the above transformation, one can easily see that the Hamiltonian H now no longer involves momentum operators and is an $8(2N+1)$ by $8(2N+1)$ algebraic matrix whose eigenvalues can be solved using MATLAB or other commercial softwares.

APPENDIX C

MODEL HAMILTONIAN FOR $ZrTe_5$

Here, we briefly show the derivation of the effective Hamiltonian and its LLs for $ZrTe_5$ [97]. We start with the following basis:

$$|+,\uparrow\rangle, |+,\downarrow\rangle, |-,\uparrow\rangle, |-,\downarrow\rangle, \tag{C.1}$$

where $\pm$ labels the orbitals (or Kramer pairs) and $\uparrow,\downarrow$ denotes the spin. In $ZrTe_5$, there are four symmetries: mirror reflection about xz plane (m_{xz}) and yz plane (m_{yz}), inversion ($\mathscr{I}$), and time reversal symmetry ($\mathscr{T}$). The eigenvalue of the symmetry operators on these four states are listed in Table C.1.

In the orbital part, the symmetry operation can bring each basis function into a linear combination of all basis functions. For example, under the m_{xz} operation, the basis $|+\rangle$ is unchanged because its eigenvalue of this operation is 1, while the state $|-\rangle$ obtains a minus sign. Therefore, $(|+\rangle, |-\rangle)$ is transformed into $(|+\rangle, -|-\rangle)$, which can be described by operating τ_z onto the original bases, where τ is the Pauli matrix operating on the orbital states. Following the same logics, one can construct all the symmetry operators on the orbital wavefunction.

As for the spin, the operation m_{xz} is equivalent to rotating the spin around y-axis 180 degree and then followed by an inversion operation. Since inversion operation does not change spin (because spin is a pseudo vector like angular momentum), the symmetry operator for m_{xz} for the spin states is $-i\sigma^y$, where σ is also the Pauli matrix but operating on the spin states. Recall that the rotation operator for spin half is [5]

$$\exp(\frac{-i\sigma\cdot\hat{n}\theta}{2}) = \cos\frac{\theta}{2} - i\sigma\cdot\hat{n}\sin\frac{\theta}{2}, \tag{C.2}$$

Table C.1: Eigenvalue of the symmetry operators on the four basis states.

	m_{xz}	m_{yz}	$\mathscr{I}$
$\|+,\uparrow\rangle$	-1	1	1
$\|+,\downarrow\rangle$	-1	1	1
$\|-,\uparrow\rangle$	1	1	-1
$\|-,\downarrow\rangle$	1	1	-1

where $\hat{n}$ is the rotation axis and θ is the rotation angle.

Therefore, the symmetry operators for Eq. (C.1) can be obtained by multiplying the spin and orbital contributions

$$m_{xz} : -i\sigma^y\tau^z, \quad m_{yz} : -i\sigma^x, \quad \mathscr{I} : \tau^z, \quad \mathscr{T} : \mathscr{K}\, i\sigma^y. \tag{C.3}$$

One can easily verify that the conjugate of each operators is the inverse operator.

The Hamiltonian H must also satisfy the above symmetries, leading to

$$\begin{aligned} H(k_x, k_y, k_z) &= \sigma^y\tau^z \cdot H(k_x, -k_y, k_z) \cdot \sigma^y\tau^z = \sigma^x \cdot H(-k_x, k_y, k_z) \cdot \sigma^x \\ &= \tau^z \cdot H(-k_x, -k_y, -k_z) \cdot \tau^z = \sigma^y \cdot [H(k_x, -k_y, k_z)]^* \cdot \sigma^y. \end{aligned} \tag{C.4}$$

Since the Hamiltonian is a 4 by 4 matrix, it must be a linear combinations of the followings

$$\sigma^i\tau^j, \quad , i, j = x, y, z, 0,$$

where $\sigma^0 = \tau^0 = I_2$ and I_2 is a 2 by 2 unit matrix. Then, we can expand $H(k_x, k_y, k_z)$ in the polynomials of k whose combination with the matrix $\sigma^i\tau^j$ is restricted by the symmetry Eq. (C.4). Therefore, we can arrived at

$$\begin{aligned} H(\mathbf{k}) = (M - \mathscr{B}' v_F^2 k^2)\tau^z I_2 + \hbar(v_{F,x} k_x \tau^x \sigma^z - v_{F,y} k_y \tau^y I_2) \\ - D' v_F^2 k^2 I_4 + (\bar{Z}' I_2 + \delta Z' \tau^z)\sigma^z, \end{aligned} \tag{C.5}$$

where M is the Dirac mass, $\mathscr{B}'$ is the band inversion parameter, D' is the electron-hole asymmetry parameter, v_F is the Fermi velocity, $v_F^2k^2 = v_{F,x}^2k_x^2 + v_{F,y}^2k_y^2$, $k_z = 0$, and

$$\tau^z I_2 = \begin{pmatrix} I_2 & 0 \\ 0 & -I_2 \end{pmatrix}, \tau^x\sigma^z = \begin{pmatrix} 0 & \sigma^z \\ \sigma^z & 0 \end{pmatrix}, \tau^y I_2 = \begin{pmatrix} 0 & -iI_2 \\ iI_2 & 0 \end{pmatrix},$$
$$I_4 = \begin{pmatrix} I_2 & 0 \\ 0 & I_2 \end{pmatrix}, I_2\sigma^z = \begin{pmatrix} \sigma^z & 0 \\ 0 & \sigma^z \end{pmatrix}, \tau^z\sigma^z = \begin{pmatrix} \sigma^z & 0 \\ 0 & -\sigma^z \end{pmatrix}.$$

In addition, the Zeeman effect is considered with $\bar{Z}' = \mu_B B\bar{g}/2$ and $\delta Z' = \mu_B B\delta g/2$, where $\bar{g} = \frac{g_+ + g_-}{2}$, $\delta g = \frac{g_+ - g_-}{2}$, μ_B is the Bohr magneton, g_+ and g_- denote the g-factors for the $+$ and $-$ orbitals, respectively. Now the Hamiltonian reads

$$H = \begin{pmatrix} H_0 & H_{01} \\ H_{10} & H_1 \end{pmatrix},$$

where

$$H_0 = \begin{pmatrix} (M - \mathscr{B}'v_F^2k^2) - D'v_F^2k^2 + \bar{Z}' + \delta Z' & 0 \\ 0 & (M - \mathscr{B}'v_F^2k^2) - D'v_F^2k^2 - \bar{Z}' - \delta Z' \end{pmatrix},$$

$$H_1 = \begin{pmatrix} -(M - \mathscr{B}'v_F^2k^2) - D'v_F^2k^2 + \bar{Z}' - \delta Z' & 0 \\ 0 & -(M - \mathscr{B}'v_F^2k^2) - D'v_F^2k^2 - \bar{Z}' + \delta Z' \end{pmatrix},$$

and

$$H_{01} = H_{10}^\dagger = \begin{pmatrix} \hbar v_{F,x}k_x + i\hbar v_{F,y}k_y & 0 \\ 0 & -\hbar v_{F,x}k_x + i\hbar v_{F,y}k_y \end{pmatrix}.$$

To obtain the LL energy, we employ the Landau-gauge vector potential $\mathbf{A} = (-By, 0, 0)$ and define $\Delta = \sqrt{|2\hbar v_{F,x}v_{F,y}eB|}$ and $\hat{b} = \frac{(v_{F,x}\hat{P}_x - iv_{F,y}\hat{P}_y)}{\Delta}$ (where $\hat{P}_x$ and $\hat{P}_y$ are momentum operators). Then, $[\hat{b}, \hat{b}^\dagger] = 1$ and $v_F^2k^2 = (\hat{b}^\dagger\hat{b} + \frac{1}{2})\Delta^2 = (n + \frac{1}{2})\Delta^2$. The Hamiltonian

in a magnetic field becomes

$$H_0 = \begin{pmatrix} M - (\mathscr{B}' + D')(n - \frac{1}{2})\Delta^2 + \bar{Z}' + \delta Z' & 0 \\ 0 & M - (\mathscr{B}' + D')(n + \frac{1}{2})\Delta^2 - \bar{Z}' - \delta Z' \end{pmatrix},$$

$$H_1 = \begin{pmatrix} -M + (\mathscr{B}' - D')(n + \frac{1}{2})\Delta^2 + \bar{Z}' - \delta Z' & 0 \\ 0 & -M + (\mathscr{B}' - D')(n - \frac{1}{2})\Delta^2 - \bar{Z}' + \delta Z' \end{pmatrix},$$

and

$$H_{01} = H_{10}^{\dagger} = \begin{pmatrix} \Delta\sqrt{n} & 0 \\ 0 & -\Delta\sqrt{n} \end{pmatrix}.$$

The corresponding LL energies are

$$E_0^{\uparrow} = M - \frac{\mathscr{B}' + D'}{2}\Delta^2 + \bar{Z}' + \delta Z', \tag{C.6}$$

$$E_0^{\downarrow} = -M + \frac{\mathscr{B}' - D'}{2}\Delta^2 - \bar{Z}' + \delta Z', \tag{C.7}$$

and for $n \neq 0$,

$$E_{n,\pm}^{s} = (-\frac{s\mathscr{B}'}{2} - nD')\Delta^2 + s\bar{Z}' \pm \sqrt{\Delta^2 n + \left[M - (n\mathscr{B}' + \frac{sD'}{2})\Delta^2 + s\delta Z'\right]^2}, \tag{C.8}$$

where $s = \uparrow\downarrow = \pm 1$ stands for the spin-up and spin-down LLs. These solutions are essentially the same as Eq. (5.2). The above equations work for both 2D and 3D massive Dirac fermions (for the latter, when taking the $k_z = 0$ limit).

REFERENCES

[1] K. von Klitzing, "The quantized Hall effect", Rev. Mod. Phys. **58**, 519 (1986).

[2] M. Z. Hasan and C. L. Kane, "Colloquim: topological insulators", Rev. Mod. Phys. **82**, 3045 (2010).

[3] M. E. Cage, R. F. Dziuba, and B. F. Field, "A test of the quantum Hall effect as a resistance standard", IEEE Trans. Instrum. Meas. **34**, 301 (1985).

[4] A. Gray, *Modern differential geometry of curves and surfaces with Mathematica* (CRC Press, Boca Raton, 1999).

[5] J. J. Sakurai, *Modern quantum mechanics*, edited by S. F. Tuan (Addison-Wesley Pub. Co., Reading, Massachusetts, 1994).

[6] D. J. Thouless, M. Kohmoto, M. P. Nightingale, and M. den Nijs, "Quantized Hall conductance in a two-dimensional periodic potential", Phys. Rev. Lett. **49**, 405 (1982).

[7] C. L. Kane and E. J. Mele, "Quantum spin Hall effect in graphene", Phys. Rev. Lett. **95**, 226801 (2005).

[8] B. A. Bernevig, T. L. Hughes, and S.-C. Zhang, "Quantum spin Hall effect and topological phase transition in HgTe quantum wells", Science **314**, 1757 (2006).

[9] M. König, S. Wiedmann, C. Brüne, A. Roth, H. Buhmann, L. W. Molenkamp, X.-L. Qi, and S.-C. Zhang, "Quantum spin Hall insulator state in HgTe quantum wells", Science **318**, 766 (2007).

[10] A. Roth, C. Brüne, H. Buhmann, L. W. Molenkamp, J. Maciejko, X.-L. Qi, and S.-C. Zhang, "Nonlocal transport in the quantum spin Hall state", Science **325**, 294 (2009).

[11] C. Liu, T. L. Hughes, X.-L. Qi, K. Wang, and S.-C. Zhang, "Quantum spin Hall effect in inverted type-II semiconductors", Phys. Rev. Lett. **100**, 236601 (2008).

[12] L. Fu, C. L. Kane, and E. J. Mele, "Topological insulators in three dimensions", Phys. Rev. Lett. **98**, 106803 (2007).

[13] X.-L. Qi and S.-C. Zhang, "Topological insulators and superconductors", Rev. Mod. Phys. **83**, 1057 (2011).

[14] Y. Xia, D. Qian, D. Hsieh, L. Wray, A. Pal, H. Lin, A. Bansil, D. Grauer, Y. S. Hor, R. J. Cava, and M. Z. Hasan, "Observation of a large-gap topological-insulator class with a single Dirac cone on the surface", Nat. Phys. **5**, 398 (2009).

[15] Y. Ando, "Topological insulator materials", J. Phys. Soc. Jpn. **82**, 102001 (2013).

[16] A. Nishide, A. A. Taskin, Y. Takeichi, T. Okuda, A. Kakizaki, T. Hirahara, K. Nakatsuji, F. Komori, Y. Ando, and I. Matsuda, "Direct mapping of the spin-filtered surface bands of a three-dimensional quantum spin Hall insulator", Phys. Rev. B **81**, 041309 (2010).

[17] Z. Ren, A. A. Taskin, S. Sasaki, K. Segawa, and Y. Ando, "Fermi level tuning and a large activation gap achieved in the topological insulator Bi_2Te_2Se by Sn doping", Phys. Rev. B **85**, 155301 (2012).

[18] Z. Ren, A. A. Taskin, S. Sasaki, K. Segawa, and Y. Ando, "Optimizing $Bi_{2-x}Sb_x$ $Te_{3-y}Se_y$ solid solutions to approach the intrinsic topological insulator regime", Phys. Rev. B **84**, 165311 (2011).

[19] M. Brahlek, N. Koirala, M. Salehi, N. Bansal, and S. Oh, "Emergence of decoupled surface transport channels in bulk insulating Bi_2Se_3 thin films", Phys. Rev. Lett. **113**, 026801 (2014).

[20] S. Syed, J. B. Heroux, Y. J. Wang, M. J. Manfra, R. J. Molnar, and H. L. Stormer, "Nonparabolicity of the conduction band of wurtzite GaN", Appl. Phys. Lett. **83**, 4553 (2003).

[21] M. Orlita, C. Faugeras, A.-L. Barra, G. Martinez, M. Potemski, D. M. Basko, M. S. Zholudev, F. Teppe, W. Knap, V. I. Gavrilenko, N. N. Mikhailov, S. A. Dvoretskii, P. Neugebauer, C. Berger, and W. A. de Heer, "Infrared magneto-spectroscopy of two-dimensional and three-dimensional massless fermions: a comparison", J. Appl. Phys. **117**, 112803 (2015).

[22] E. Kane, "Energy band structure in p-type germanium and silicon", J. Phys. Chem. Solids **1**, 82 (1956).

[23] M. Cardona and F. H. Pollak, "Energy-band structure of germanium and silicon: the $\mathbf{k} \cdot \mathbf{p}$ method", Phys. Rev. **142**, 530 (1966).

[24] L. C. Lew Yan Voon and M. Willatzen, *The $\boldsymbol{k} \cdot \boldsymbol{p}$ method: electronic properties of semiconductors* (Springer-Verlag, Berlin, Heidelberg, 2009).

[25] P.-O. Löwdin, "A note on the quantum mechanical perturbation theory", J. Chem. Phys. **19**, 1396 (1951).

[26] R. Winkler, *Spin-orbit coupling effects in two-dimensional electron and hole systems* (Springer-Verlag, Berlin, Heidelberg, 2003).

[27] J. Li, W. Yang, and K. Chang, "Spin states in InAs/AlSb/GaSb semiconductor quantum wells", Phys. Rev. B **80**, 035303 (2009).

[28] M. Gmitra and J. Fabian, "First-principles studies of orbital and spin-orbit properties of GaAs, GaSb, InAs, and InSb zinc-blende and wurtzite semiconductors", Phys. Rev. B **94**, 165202 (2016).

[29] G. D. Sanders, Y. Sun, F. V. Kyrychenko, C. J. Stanton, G. A. Khodaparast, M. A. Zudov, J. Kono, Y. H. Matsuda, N. Miura, and H. Munekata, "Electronic states and cyclotron resonance in n-type InMnAs", Phys. Rev. B **68**, 165205 (2003).

[30] J. M. Luttinger, "Quantum theory of cyclotron resonance in semiconductors: general theory", Phys. Rev. **102**, 1030 (1956).

[31] C.-X. Liu, X.-L. Qi, H. Zhang, X. Dai, Z. Fang, and S.-C. Zhang, "Model Hamiltonian for topological insulators", Phys. Rev. B **82**, 045122 (2010).

[32] E. G. Novik, A. Pfeuffer-Jeschke, T. Jungwirth, V. Latussek, C. R. Becker, G. Landwehr, H. Buhmann, and L. W. Molenkamp, "Band structure of semimagnetic $Hg_{1-y}Mn_yTe$ quantum wells", Phys. Rev. B **72**, 035321 (2005).

[33] S.-Q. Shen, *Topological insulators: Dirac equation in condensed matters* (Springer, Berlin, 2012).

[34] D. N. Basov, R. D. Averitt, D. van der Marel, M. Dressel, and K. Haule, "Electrodynamics of correlated electron materials", Rev. Mod. Phys. **83**, 471 (2011).

[35] K. Masutani, *Introduction to experimental infrared spectroscopy*, edited by M. Tasumi and A. Sakamoto (Wiley, Chichester, 2015).

[36] P. R. Griffiths and J. A. de Haseth, *Fourier transform infrared spectrometry* (John Wiley & Sons, Inc., Hoboken, 2007).

[37] A. Rogalski, "Infrared detectors: status and trends", Prog. Quantum Electron. **27**, 59 (2003).

[38] P. L. Richards, "Bolometers for infrared and millimeter waves", J. Appl. Phys. **76**, 1 (1994).

[39] J. Faist, F. Capasso, D. L. Sivco, C. Sirtori, A. L. Hutchinson, and A. Y. Cho, "Quantum cascade laser", Science **264**, 553 (1994).

[40] C. Gmachl, F. Capasso, D. L. Sivco, and A. Y. Cho, "Recent progress in quantum cascade lasers and applications", Rep. Prog. Phys. **64**, 1533 (2001).

[41] J. Faist, F. Capasso, C. Sirtori, D. L. Sivco, A. L. Hutchinson, and A. Y. Cho, "Vertical transition quantum cascade laser with Bragg confined excited state", Appl. Phys. Lett. **66**, 538 (1995).

[42] J. M. Beckers, "Achromatic linear retarders", Appl. Opt. **10**, 973 (1971).

[43] R. M. A. Azzam, "Phase shifts that accompany total internal reflection at a dielectric-dielectric interface", J. Opt. Soc. Am. A **21**, 1559 (2004).

[44] X. Xi, R. Smith, T. Stanislavchuk, A. Sirenko, S. Gilbert, J. Tu, and G. Carr, "A broadband silicon quarter-wave retarder for far-infrared spectroscopic circular dichroism", Infrared Phys. Technol. **67**, 436 (2014).

[45] H. Kroemer, "Heterostructure devices: A device physicist looks at interfaces", Surf. Sci. **132**, 543 (1983).

[46] J. Kono, B. D. McCombe, J.-P. Cheng, I. Lo, W. C. Mitchel, and C. E. Stutz, "Cyclotron-resonance oscillations in a two-dimensional electron-hole system", Phys. Rev. B **50**, 12242 (1994).

[47] J. Kono, B. D. McCombe, J.-P. Cheng, I. Lo, W. C. Mitchel, and C. E. Stutz, "Far-infrared magneto-optical study of two-dimensional electrons and holes in InAs/ $Al_xGa_{1-x}Sb$ quantum wells", Phys. Rev. B **55**, 1617 (1997).

[48] L.-C. Tung, P. A. Folkes, G. Gumbs, W. Xu, and Y.-J. Wang, "Magneto-infrared modes in InAs-AlSb-GaSb coupled quantum wells", Phys. Rev. B **82**, 115305 (2010).

[49] G. M. Sundaram, R. J. Warburton, R. J. Nicholas, G. M. Summers, N. J. Mason, and P. J. Walker, "Cyclotron resonance in InAs/GaSb heterostructures", Semicond. Sci. Technol. **7**, 985 (1992).

[50] M. J. Yang, C. H. Yang, B. R. Bennett, and B. V. Shanabrook, "Evidence of a hybridization gap in semimetallic InAs/GaSb systems", Phys. Rev. Lett. **78**, 4613 (1997).

[51] T. P. Marlow, L. J. Cooper, D. D. Arnone, N. K. Patel, D. M. Whittaker, E. H. Linfield, D. A. Ritchie, and M. Pepper, "Ground state of a two-dimensional coupled electron-hole gas in InAs/GaSb narrow gap heterostructures", Phys. Rev. Lett. **82**, 2362 (1999).

[52] C. Petchsingh, R. J. Nicholas, K. Takashina, N. J. Mason, and J. Zeman, "Mass enhancement and electron-hole coupling in InAs/GaSb bilayers studied by cyclotron resonance", Physica E **12**, 289 (2002).

[53] C. Petchsingh, R. J. Nicholas, K. Takashina, N. J. Mason, and J. Zeman, "Effects of electron-hole hybridization on cyclotron resonance in InAs/GaSb heterostructures", Phys. Rev. B **70**, 155306 (2004).

[54] F. Qu, A. J. A. Beukman, S. Nadj-Perge, M. Wimmer, B.-M. Nguyen, W. Yi, J. Thorp, M. Sokolich, A. A. Kiselev, M. J. Manfra, C. M. Marcus, and L. P. Kouwenhoven, "Electric and magnetic tuning between the trivial and topological phases in InAs/GaSb double quantum wells", Phys. Rev. Lett. **115**, 036803 (2015).

[55] I. Knez, R.-R. Du, and G. Sullivan, "Evidence for helical edge modes in inverted InAs/GaSb quantum wells", Phys. Rev. Lett. **107**, 136603 (2011).

[56] L. Du, I. Knez, G. Sullivan, and R.-R. Du, "Robust helical edge transport in gated InAs/GaSb bilayers", Phys. Rev. Lett. **114**, 096802 (2015).

[57] S. Mueller, A. N. Pal, M. Karalic, T. Tschirky, C. Charpentier, W. Wegscheider, K. Ensslin, and T. Ihn, "Nonlocal transport via edge states in InAs/GaSb coupled quantum wells", Phys. Rev. B **92**, 081303 (2015).

[58] T. Li, P. Wang, H. Fu, L. Du, K. A. Schreiber, X. Mu, X. Liu, G. Sullivan, G. A. Csáthy, X. Lin, and R.-R. Du, "Observation of a helical Luttinger liquid in InAs/GaSb quantum spin Hall edges", Phys. Rev. Lett. **115**, 136804 (2015).

[59] L. Du, W. Lou, C. Kai, G. Sullivan, and R.-R. Du, "Gate-tuned spontaneous exciton insulator in double-quantum wells", arxiv:1508.04509.

[60] X. Shi, W. Yu, Z. Jiang, B. A. Bernevig, W. Pan, S. D. Hawkins, and J. F. Klem, "Giant supercurrent states in a superconductor-InAs/GaSb-superconductor junction", J. Appl. Phys. **118**, 133905 (2015).

[61] L. Du, T. Li, W. Lou, X. Wu, X. Liu, Z. Han, C. Zhang, G. Sullivan, A. Lkhlassi, C. Kai, and R.-R. Du, "Strain-engineering of InAs/GaInSb topological insulator towards majorana platform", arxiv:1608.06588.

[62] A. Rogalski and P. Martyniuk, "InAs/GaInSb superlattices as a promising material system for third generation infrared detectors", Infrared Phys. Technol. **48**, 39 (2006).

[63] L. M. Murray, D. T. Norton, J. T. Olesberg, T. F. Boggess, and J. P. Prineas, "Comparison of tunnel junctions for cascaded InAs/GaSb superlattice light emitting diodes", J. Vac. Sci. Technol. B **30**, 021203 (2012).

[64] J.-S. Liu, Y. Zhu, P. S. Goley, and M. K. Hudait, "Heterointerface engineering of broken-gap InAs/GaSb multilayer structures", ACS Appl. Mater. Interfaces **7**, PMID: 25568961, 2512 (2015).

[65] E. R. Youngdale, J. R. Meyer, C. A. Hoffman, F. J. Bartoli, C. H. Grein, P. M. Young, H. Ehrenreich, R. H. Miles, and D. H. Chow, "Auger lifetime enhancement in InAs-$Ga_{1-x}In_xSb$ superlattices", Appl. Phys. Lett. **64**, 3160 (1994).

[66] Y. Jiang, S. Thapa, G. D. Sanders, C. J. Stanton, Q. Zhang, J. Kono, W. K. Lou, K. Chang, S. D. Hawkins, J. F. Klem, W. Pan, D. Smirnov, and Z. Jiang, "Probing the semiconductor to semimetal transition in InAs/GaSb double quantum wells by magneto-infrared spectroscopy", Phys. Rev. B **95**, 045116 (2017).

[67] M. G. Burt, "The justification for applying the effective-mass approximation to microstructures", J. Phys. Condens. Matter **4**, 6651 (1992).

[68] G. L. Bir and G. E. Pikus, *Symmetry and strain-induced effects in semiconductors* (Wiley, New York, 1975).

[69] R. M. Wood, D. Saha, L. A. McCarthy, J. T. Tokarski, G. D. Sanders, P. L. Kuhns, S. A. McGill, A. P. Reyes, J. L. Reno, C. J. Stanton, and C. R. Bowers, "Effects of strain and quantum confinement in optically pumped nuclear magnetic resonance in GaAs: interpretation guided by spin-dependent band structure calculations", Phys. Rev. B **90**, 155317 (2014).

[70] S. L. Chuang, *Physics of optoelectronic devices* (Wiley, New York, 1995).

[71] S. Datta, *Quantum transport: atom to transistor* (Cambridge University Press, New York, 2005).

[72] A. Zakharova, S. T. Yen, and K. A. Chao, "Landau level structures and semimetal-semiconductor transition in strained InAs/GaSb quantum wells", Phys. Rev. B **69**, 115319 (2004).

[73] K. Nilsson, A. Zakharova, I. Lapushkin, S. T. Yen, and K. A. Chao, "Cyclotron masses and g-factors of hybridized electron-hole states in InAs/GaSb quantum wells", Phys. Rev. B **74**, 075308 (2006).

[74] C. R. Pidgeon and R. N. Brown, "Interband magneto-absorption and Faraday rotation in InSb", Phys. Rev. **146**, 575 (1966).

[75] I. Lapushkin, A. Zakharova, S. T. Yen, and K. A. Chao, "Self-consistent investigation of the semimetal-semiconductor transition in InAs/GaSb quantum wells under external electric fields", J. Phys. Condens. Matter **16**, 4677 (2004).

[76] J. Li, K. Chang, G. Q. Hai, and K. S. Chan, "Anomalous Rashba spin-orbit interaction in InAs/GaSb quantum wells", Appl. Phys. Lett. **92**, 152107 (2008).

[77] L.-H. Hu, C.-X. Liu, D.-H. Xu, F.-C. Zhang, and Y. Zhou, "Electric control of inverted gap and hybridization gap in type-II InAs/GaSb quantum wells", Phys. Rev. B **94**, 045317 (2016).

[78] T. Kasturiarachchi, D. Saha, X. Pan, G. D. Sanders, M. Edirisooriya, T. D. Mishima, R. E. Doezema, C. J. Stanton, and M. B. Santos, "Interband magneto-spectroscopy in InSb square and parabolic quantum wells", J. Appl. Phys. **117**, 213914 (2015).

[79] L. L. Chang, N. Kawai, G. A. SaiHalasz, R. Ludeke, and L. Esaki, "Observation of semiconductor-semimetal transition in InAs-GaSb superlattices", Appl. Phys. Lett. **35**, 939 (1979).

[80] I. Vurgaftman, J. R. Meyer, and L. R. Ram-Mohan, "Band parameters for III-V compound semiconductors and their alloys", J. Appl. Phys. **89**, 5815 (2001).

[81] I. V. Lerner and Y. E. Lozovik, "Electron-hole rearrangements in two-dimensional semimetals in high magnetic fields", J. Phys. C **12**, L501 (1979).

[82] D. J. Barnes, R. J. Nicholas, R. J. Warburton, N. J. Mason, P. J. Walker, and N. Miura, "Observation of magnetic-field-induced semimetal-semiconductor transitions in crossed-gap superlattices by cyclotron resonance", Phys. Rev. B **49**, 10474 (1994).

[83] H. Weng, X. Dai, and Z. Fang, "Transition-metal pentatelluride $ZrTe_5$ and $HfTe_5$: a paradigm for large-gap quantum spin Hall insulators", Phys. Rev. X **4**, 011002 (2014).

[84] R. T. Littleton IV, T. M. Tritt, C. R. Feger, J. Kolis, M. L. Wilson, M. Marone, J. Payne, D. Verebeli, and F. Levy, "Effect of Ti substitution on the thermoelectric properties of the pentatelluride materials $M_{1-x}Ti_xTe_5$ (M=Hf,Zr)", Appl. Phys. Lett. **72**, 2056 (1998).

[85] O. Vafek and A. Vishwanath, "Dirac fermions in solids: from high-Tc cuprates and graphene to topological insulators and Weyl semimetals", Annu. Rev. Condens. Matter Phys. **5**, 83 (2014).

[86] Z. Fan, Q. F. Liang, Y. B. Chen, S.-H. Yao, and J. Zhou, "Transition between strong and weak topological insulator in $ZrTe_5$ and $HfTe_5$", Sci. Rep. **7**, 45567 (2017).

[87] W. Yu, Y. Jiang, J. Yang, Z. L. Dun, H. D. Zhou, Z. Jiang, P. Lu, and W. Pan, "Quantum oscillations at integer and fractional Landau level indices in $ZrTe_5$", Sci. Rep. **6**, 12576 (2016).

[88] X. Yuan, C. Zhang, Y. Liu, A. Narayan, C. Song, S. D. Shen, X. Sui, J. Xu, H. Yu, Z. An, J. Zhao, S. Sanvito, H. Yan, and F. Xiu, "Observation of quasi-two-dimensional Dirac fermions in $ZrTe_5$", NPG Asia Mater. **8**, e325 (2016).

[89] Y. Liu, X. Yuan, C. Zhang, Z. Jin, A. Narayan, C. Luo, Z. Chen, L. Yang, J. Zou, X. Wu, S. Sanvito, Z. Xia, L. Li, Z. Wang, and F. Xiu, "Zeeman splitting and dynamical mass generation in Dirac semimetal $ZrTe_5$", Nat. Comm. **7**, 12516 (2016).

[90] Q. Li, D. E. Kharzeev, C. Zhang, Y. Huang, I. Pletikosić, A. V. Fedorov, R. D. Zhong, J. A. Schneeloch, G. D. Gu, and T. Valla, "Chiral magnetic effect in $ZrTe_5$", Nat. Phys. **12**, 550 (2016).

[91] L. Moreschini, J. C. Johannsen, H. Berger, J. Denlinger, C. Jozwiak, E. Rotenberg, K. S. Kim, A. Bostwick, and M. Grioni, "Nature and topology of the low-energy states in $ZrTe_5$", Phys. Rev. B **94**, 081101 (2016).

[92] Y. Zhang, C. Wang, L. Yu, G. Liu, A. Liang, J. Huang, S. Nie, Y. Zhang, B. Shen, J. Liu, H. Weng, L. Zhao, G. Chen, X. Jia, C. Hu, Y. Ding, S. He, L. Zhao, F. Zhang, S. Zhang, F. Yang, Z. Wang, Q. Peng, X. Dai, Z. Fang, Z. Xu, C. Chen, and X. J. Zhou, "Electronic evidence of temperature-induced Lifshitz transition and topological nature in $ZrTe_5$", arXiv:1602.03576.

[93] R. Wu, J.-Z. Ma, S.-M. Nie, L.-X. Zhao, X. Huang, J.-X. Yin, B.-B. Fu, P. Richard, G.-F. Chen, Z. Fang, X. Dai, H.-M. Weng, T. Qian, H. Ding, and S. H. Pan, "Evidence for topological edge states in a large energy gap near the step edges on the surface of $ZrTe_5$", Phys. Rev. X **6**, 021017 (2016).

[94] G. Manzoni, L. Gragnaniello, G. Autès, T. Kuhn, A. Sterzi, F. Cilento, M. Zacchigna, V. Enenkel, I. Vobornik, L. Barba, F. Bisti, P. Bugnon, A. Magrez, V. N. Strocov, H. Berger, O. V. Yazyev, M. Fonin, F. Parmigiani, and A. Crepaldi, "Evidence for a strong topological insulator phase in $ZrTe_5$", Phys. Rev. Lett. **117**, 237601 (2016).

[95] L. Shen, M. Wang, S. Sun, J. Jiang, X. Xu, T. Zhang, Q. Zhang, Y. Lv, S. Yao, Y. Chen, M. Lu, Y. Chen, C. Felser, B. Yan, Z. Liu, L. Yang, and Y. L. Chen, "Spectroscopic evidence for the gapless electronic structure in bulk $ZrTe_5$", J. Electron Spectros. Relat. Phenom., in press (2016).

[96] X.-B. Li, W.-K. Huang, Y.-Y. Lv, K.-W. Zhang, C.-L. Yang, B.-B. Zhang, Y. B. Chen, S.-H. Yao, J. Zhou, M.-H. Lu, L. Sheng, S.-C. Li, J.-F. Jia, Q.-K. Xue, Y.-F. Chen, and D.-Y. Xing, "Experimental observation of topological edge states at the surface step edge of the topological insulator $ZrTe_5$", Phys. Rev. Lett. **116**, 176803 (2016).

[97] R. Y. Chen, S. J. Zhang, J. A. Schneeloch, C. Zhang, Q. Li, G. D. Gu, and N. L. Wang, "Optical spectroscopy study of the three-dimensional Dirac semimetal $ZrTe_5$", Phys. Rev. B **92**, 075107 (2015).

[98] R. Y. Chen, Z. G. Chen, X.-Y. Song, J. A. Schneeloch, G. D. Gu, F. Wang, and N. L. Wang, "Magnetoinfrared spectroscopy of Landau levels and Zeeman splitting of three-dimensional massless Dirac fermions in $ZrTe_5$", Phys. Rev. Lett. **115**, 176404 (2015).

[99] M. Binnewies, R. Glaum, M. Schmidt, and P. Schmidt, *Chemical vapor transport reactions* (Walter de Gruyter, Berlin, 2012).

[100] M. Orlita, C. Faugeras, G. Martinez, D. K. Maude, M. L. Sadowski, and M. Potemski, "Dirac fermions at the H point of graphite: magnetotransmission studies", Phys. Rev. Lett. **100**, 136403 (2008).

[101] K.-C. Chuang, A. M. R. Baker, and R. J. Nicholas, "Magnetoabsorption study of Landau levels in graphite", Phys. Rev. B **80**, 161410 (2009).

[102] L.-C. Tung, W. Yu, P. Cadden-Zimansky, I. Miotkowski, Y. P. Chen, D. Smirnov, and Z. Jiang, "Magnetoinfrared spectroscopic study of thin Bi_2Te_3 single crystals", Phys. Rev. B **93**, 085140 (2016).

[103] Y. Jiang, Z. Dun, H. Zhou, Z. Lu, K.-W. Chen, S. Moon, T. Besara, T. Siegrist, R. Baumbach, D. Smirnov, and Z. Jiang, "Landau level spectroscopy of massive Dirac fermions in single-crystalline $ZrTe_5$ thin flakes", arXiv:1703.08193.

[104] T. Timusk, J. P. Carbotte, C. C. Homes, D. N. Basov, and S. G. Sharapov, "Three-dimensional Dirac fermions in quasicrystals as seen via optical conductivity", Phys. Rev. B **87**, 235121 (2013).

[105] K. F. Mak, M. Y. Sfeir, Y. Wu, C. H. Lui, J. A. Misewich, and T. F. Heinz, "Measurement of the optical conductivity of graphene", Phys. Rev. Lett. **101**, 196405 (2008).

[106] Z. Li, E. Henriksen, Z. Jiang, Z. Hao, M. Martin, P. Kim, H. Stormer, and D. Basov, "Dirac charge dynamics in graphene by infrared spectroscopy", Nat. Phys. **4**, 532 (2008).

[107] N. M. R. Peres, F. Guinea, and A. H. Castro Neto, "Electronic properties of disordered two-dimensional carbon", Phys. Rev. B **73**, 125411 (2006).

[108] D. S. L. Abergel and V. I. Fal'ko, "Optical and magneto-optical far-infrared properties of bilayer graphene", Phys. Rev. B **75**, 155430 (2007).

[109] S. Ryu, C. Mudry, A. Furusaki, and A. W. W. Ludwig, "Landauer conductance and twisted boundary conditions for Dirac fermions in two space dimensions", Phys. Rev. B **75**, 205344 (2007).

[110] M. Koshino and T. Ando, "Magneto-optical properties of multilayer graphene", Phys. Rev. B **77**, 115313 (2008).

[111] J. Niu, J. Wang, Z. He, C. Zhang, X. Li, T. Cai, X. Ma, S. Jia, D. Yu, and X. Wu, "Electrical transport in nanothick $ZrTe_5$ sheets: from three to two dimensions", Phys. Rev. B **95**, 035420 (2017).

[112] M. L. Sadowski, G. Martinez, M. Potemski, C. Berger, and W. A. de Heer, "Landau level spectroscopy of ultrathin graphite layers", Phys. Rev. Lett. **97**, 266405 (2006).

[113] Z. Jiang, E. A. Henriksen, L. C. Tung, Y.-J. Wang, M. E. Schwartz, M. Y. Han, P. Kim, and H. L. Stormer, "Infrared spectroscopy of Landau levels of graphene", Phys. Rev. Lett. **98**, 197403 (2007).

[114] Z. G. Chen, Z. W. Shi, W. Yang, X. B. Lu, Y. Lai, H. G. Yan, F. Wang, G. Y. Zhang, and Z. Q. Li, "Observation of an intrinsic bandgap and Landau level", Nat. Comm. **5**, 4461 (2014).

[115] G. Zheng, J. Lu, X. Zhu, W. Ning, Y. Han, H. Zhang, J. Zhang, C. Xi, J. Yang, H. Du, K. Yang, Y. Zhang, and M. Tian, "Transport evidence for the three-dimensional Dirac semimetal phase in $ZrTe_5$", Phys. Rev. B **93**, 115414 (2016).

[116] J. L. Mañes, "Existence of bulk chiral fermions and crystal symmetry", Phys. Rev. B **85**, 155118 (2012).

[117] S. M. Young, S. Zaheer, J. C. Y. Teo, C. L. Kane, E. J. Mele, and A. M. Rappe, "Dirac semimetal in three dimensions", Phys. Rev. Lett. **108**, 140405 (2012).

[118] Z. Wang, Y. Sun, X.-Q. Chen, C. Franchini, G. Xu, H. Weng, X. Dai, and Z. Fang, "Dirac semimetal and topological phase transitions in A_3Bi ($A = Na$, k, rb)", Phys. Rev. B **85**, 195320 (2012).

[119] Z. Wang, H. Weng, Q. Wu, X. Dai, and Z. Fang, "Three-dimensional Dirac semimetal and quantum transport in Cd_3As_2", Phys. Rev. B **88**, 125427 (2013).

[120] W. W. Toy, M. S. Dresselhaus, and G. Dresselhaus, "Minority carriers in graphite and the H-point magnetoreflection spectra", Phys. Rev. B **15**, 4077 (1977).

[121] I. Crassee, J. Levallois, D. van der Marel, A. L. Walter, T. Seyller, and A. B. Kuzmenko, "Multicomponent magneto-optical conductivity of multilayer graphene on SiC", Phys. Rev. B **84**, 035103 (2011).

[122] M. Orlita, B. A. Piot, G. Martinez, N. K. S. Kumar, C. Faugeras, M. Potemski, C. Michel, E. M. Hankiewicz, T. Brauner, S. Schreyeck, S. Grauer, K. Brunner, C. Gould, C. Brüne, and L. W. Molenkamp, "Magneto-optics of massive Dirac fermions in bulk Bi_2Se_3", Phys. Rev. Lett. **114**, 186401 (2015).

[123] B. Büttner, C. Liu, G. Tkachov, E. Novik, C. Brüne, H. Buhmann, E. Hankiewicz, P. Recher, B. Trauzettel, S. Zhang, and L. Molenkamp, "Single valley Dirac fermions in zero-gap HgTe quantum wells", Nat. Phys. **7**, 418 (2011).

[124] J. Ludwig, Y. B. Vasilyev, N. N. Mikhailov, J. M. Poumirol, Z. Jiang, O. Vafek, and D. Smirnov, "Cyclotron resonance of single-valley Dirac fermions in nearly gapless HgTe quantum wells", Phys. Rev. B **89**, 241406 (2014).

[125] F. Teppe, M. Marcinkiewicz, S. S. Krishtopenko, S. Ruffenach, C. Consejo, A. M. Kadykov, W. Desrat, D. But, W. Knap, J. Ludwig, S. Moon, D. Smirnov, M. Orlita, Z. Jiang, S. V. Morozov, V. Gavrilenko, N. N. Mikhailov, and S. A. Dvoretskii, "Temperature-driven massless Kane fermions in HgCdTe crystals", Nat. Comm. **7**, 12576 (2016).

[126] T. Mei, "Fourier transform-based $\mathbf{k} \cdot \mathbf{p}$ method of semiconductor superlattice electronic structure", J. Appl. Phys. **102**, 053708 (2007).

VITA

Yuxuan Jiang was born in 1986 in Shantou, China. He received his bachelor's degree in physics from Peking University in 2010. Since 2011, he joined Professor Zhigang Jiang's lab in Georgia Tech. From 2014 to 2016, he was a visiting student in the National High Magnetic Field Laboratory in Tallahasse, Florida, under the supervision of Doctor Dmitry Smirnov. His research interest is in the magneto-infrared spectroscopy of emerging topological materials.